Institute of Thermal Engineering

TU Graz

Burian Paul Josef, BSc

Numerical simulation of the radiative heat transfer in industrial furnaces using the lattice Boltzmann method

Master's Thesis

to achieve the university degree of

Diplom-Ingenieur / Master of Science

Master's degree programme: Mechanical Engineering

submitted to

Graz University of Technology

Supervisor

Dipl.-Ing. Dr.techn. Prieler, René, BSc

Institute of Thermal Engineering
Head: Univ.-Prof. Dipl-Ing. Dr.techn. Hochenauer, Christoph

Graz, May 2018

Affidavit

I declare that I have authored this thesis independently, that I have not used other than the declared sources/resources, and that I have explicitly indicated all material which has been quoted either literally or by content from the sources used. The text document uploaded to TUGRAZonline is identical to the present master's thesis.

Eidesstattliche Erklärung

Ich erkläre an Eides statt, dass ich die vorliegende Arbeit selbstständig verfasst, andere als die angegebenen Quellen/Hilfsmittel nicht benutzt, und die den benutzten Quellen wörtlich und inhaltlich entnommenen Stellen als solche kenntlich gemacht habe. Das in TUGRAZonline hochgeladene Textdokument ist mit der vorliegenden Masterarbeit identisch.

Date / Datum	Signature / Unterschrift

Abstract

The prediction of the radiative heat transfer in furnaces remains a time-consuming component towards the development of new furnace designs. The goal of this thesis was to research the basis for a new simulation technique based on the lattice Boltzmann method to model both time and cost efficiently the radiative heat transfer in industrial furnaces. Existing approaches to solve the radiative transport equation as well as the heat transport equation based on the lattice Boltzmann method were analysed. A two-dimensional lattice Boltzmann based model was developed and validated against established radiative heat transfer models such as the spherical harmonics method (P1) or the discrete ordinates method (DOM). Subsequently, the lattice Boltzmann model for the heat transfer equation was coupled with the radiative transfer equation to take into account radiation in participating media. The validated model was further adapted to simulate the radiative heat transfer in a walking hearth type reheating furnace in order to examine the heat fluxes transferred to the furnace load consisting of 64 steel billets. The results showed good comparison to existing radiation modelling methods. Furthermore, points for improvement for future development of the method especially concerning the simulation runtime and accuracy of results are shown.
The fundamentals of calculating radiative heat transfer in industrial furnaces using the lattice Boltzmann method were evaluated, allowing the possibility of future application in the development of industrial furnaces.

Kurzfassung

Bei Hochtemperaturprozessen und insbesondere in Industrieöfen wird ein Großteil der Wärmeleistung durch Wärmestrahlung übertragen. Eine möglichst genaue Vorhersage der übertragenen Wärmeleistung ist daher unerlässlich für einen effizienten Betrieb beziehungsweise die Entwicklung neuer Ofendesigns.
Im Rahmen dieser Masterarbeit wurde ein Simulationsmodell auf Basis der Lattice Boltzmann Methode entwickelt, mit welchem es möglich ist den Strahlungswärmetransport in einem vereinfachten zweidimensionalen Industrieofenmodell zu berechnen. Im ersten Schritt wurde die Anwendbarkeit der Lattice Boltzmann Methode für den erläuterten Anwendungsfall untersucht. Neben analytischen Lösungen, wurden etablierte, in kommerziellen Softwarepaketen enthaltene Strahlungsmodelle zur Validierung herangezogen. Als Referenzlösung diente beispielsweise das „discrete ordinates model" (DOM) und das „spherical harmonics model" (P1). Des Weiteren wurde das Modell mit der Energiegleichung gekoppelt um den Strahlungswärmetransport in beteiligten, insbesondere in absorbierenden, Medien zu berechnen. Mithilfe des validierten Modells konnte der Strahlungswärmetransport in einem Hubbalkenofen ermittelt werden. Die Ergebnisse zeigten gute Übereinstimmung mit jenen der mittels „computational fluid dynamics" (CFD) berechneten Referenzlösungen.
Die Grundsätze des Strahlungswärmetransportes in Industrieöfen mittels der Lattice Boltzmann Methode wurden erarbeitet sowie Möglichkeiten zur weitergehenden Anwendung aufgezeigt.

Contents

List of Figures

List of Tables

Nomenclature

^{eq}	equilibrium
c	speed of light
c_i	lattice velocity in discrete direction i
c_P	specific heat capacity
f_i	radiative particle distribution function in lattice direction i
G	volumetric absorption
g_i	temperature particle distribution function in lattice direction i
I	radiative intensity
I_i	radiative intensity in the discrete direction i
k	thermal conductivity
N	Stark number
N_x	number of cell nodes in x-direction
N_y	number of cell nodes in y-direction
p	scattering phase function
q	heat flux
$\mathbf{r}$, $\vec{r}$	spatial direction vector
S	source term
s	geometric distance (in the direction $\hat{s}$)
t	time
T	temperature
T_{ref}	reference temperature
$\widetilde{T}$	dimensionless temperature
U	lattice velocity
W	scaling factor
w_i	lattice weight in discrete direction i
w_j	DOM weight factor in discrete direction i

Greek symbols:

α	thermal diffusivity
β	extinction coefficient
Γ	collision operator
$\delta_{\alpha\beta}$	Kronecker symbol
ε	emissivity of surface
ϵ	Levi-Civita symbol
ζ	dimensionless time
Θ	polar angle / zenith
κ_a	absorption coefficient
λ	wavelength
μ	direction cosine of azimuthal direction
ρ	density
σ_S	scattering coefficient
τ	relaxation time
τ_η	optical thickness
Φ	scattering phase function
χ	dimensionless radiative intensity
Ψ	azimuthal angle
Ω	solid angle
Ω_i	collision operation in lattice direction i
ω	scattering albedo

Acronyms

ADE advection-diffusion equation

BGK Bhatnagar-Gross-Krook

C-E Chapman-Enskog
CDE convection-diffusion equation
CFD computational fluid dynamics

DOM discrete ordinates method

ETLBE energy transport lattice Boltzmann equation

LBE lattice Boltzmann equation
LBM lattice Boltzmann method

MD molecular dynamics
MS multi speed

NSE Navier-Stokes equations

PDE partial differential equation
PDF particle distribution function

RTE radiative transport equation
RTLBE radiative transport lattice Boltzmann equation

SRT single-relaxation-time

TDF temperature distribution functions

UDF user-defined function

1. Introduction

The goal of this thesis was to identify the potential of the lattice Boltzmann method (LBM) to predict the radiative heat transfer in industrial furnaces. The importance for the accurate prediction of the radiative heat transfer is motivated by the urge to reduce CO_2 emissions, thus requiring efficient furnaces designs [1]. Furthermore, an accurate knowledge of the energy fluxes allows an economical usage and consumption of expensive natural gas resources. According to Prieler et al. [2] numerical models offer the possibility to analyse and optimise the heating processes and workflow conditions. Introductory current methods in use for furnace simulations are briefly described. Following the general introduction of the fundamentals of the radiative heat transfer, radiative modelling methods are summarized in Ch. 2. The third chapter (Ch. 3) gives an overview over the exploited LBMs for both solving the radiative transport equation (RTE), as well as the energy or heat transport equation. Subsequently, in Ch. 4 the results of the LBM simulation are given and the validation process is outlined. After successful validation of the elaborated model Ch. 5 is devoted to a walking hearth furnace, which was simulated in three consecutive steps. Apart from the gaseous phase also the heat transport inside the billets was calculated using the LBM.

1.1. Fundamentals of radiative heat transfer

The following chapter is intended to give a brief overview of the necessary background information on thermal radiation. It is based on Modest [3] as well as Howell et al. [4].

Heat can be generally transported by [3]:

- conduction
- convection
- radiation

In contrast to conduction and convection, which both require the presence of a medium for the energy transfer, thermal radiation is transferred by electromagnetic waves or photons, thereby does not require a medium for its transfer. Another major difference between the above-mentioned is the heat transfer range. Conduction and convection allow an energy balance on an 'infinitesimal volume' (conservation of energy) leading to the formulation of a partial differential equation. Thermal radiation is a long-range phenomenon. *This leads to an integral equation in up to seven independent variables (the frequency of radiation, three space coordinates, two coordinates describing the direction of travel of photons, and time)* [3].
There are two possible approaches to describe thermal radiative energy (electromagnetic wave theory or quantum mechanics), however neither one is able to describe all observed radiative phenomena. Figure 1.1 illustrates the dependency of the above-mentioned different variables, for different forms of radiation, with respect to characteristics such as frequency, wavenumber and wavelength.
Regarding the intervening medium the radiation travels through one needs to differentiate between participating and non-participating media. A medium affecting the quantity of radiation is denoted 'participating' [4].
Radiation is a three-dimensional phenomenon, thus the most crucial parameters will be briefly described (in accordance with Fig. 1.2). The energy flux emitted from the point P into the environment, displayed as a unit hemisphere, may vary in different directions. The surface area of the hemisphere is denoted as 'total solid angle' with a value of 2π. The solid angle Ω itself describes the angle from which an area dA_j gets irradiated by the source in point P.

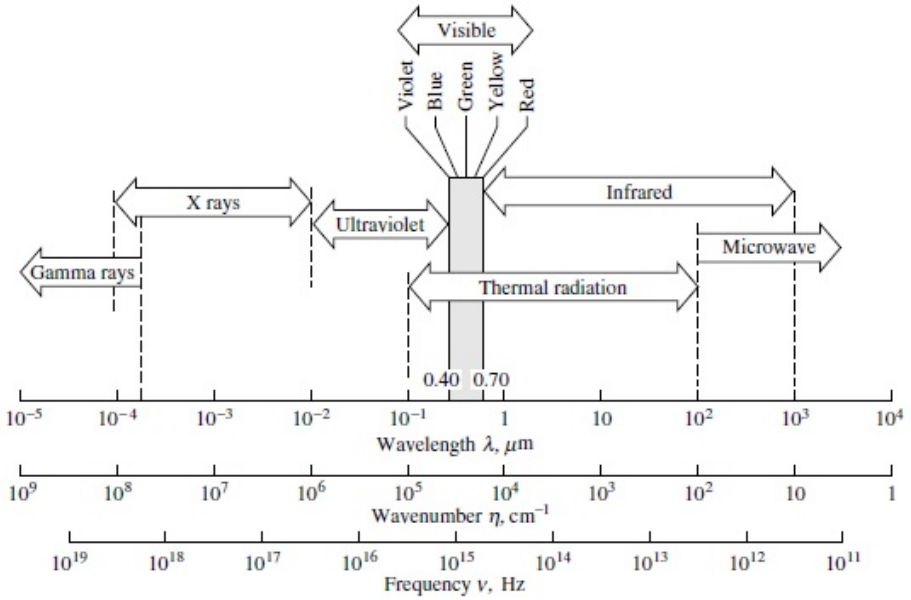

Figure 1.1.: *Electromagnetic wave spectrum (for radiation travelling through vacuum, n=1)* [3]

The mathematical context is given by Eq. 1.1,

$$d\Omega = \frac{dA_{jp}}{S^2} = \frac{\cos\Theta_j dA_j}{S^2} \tag{1.1}$$

in which S denotes the distance between the irradiated surface dA_j and the point P. The projection of the irradiated surface dA_j on the hemisphere is given by the surface element dA_{jp}, which is related via the polar angle (or zenith) Θ_j. The polar angle Θ_j is determined by the angle between the surface normals of the surface elements dA_j and dA_{jp}. The irradiated surface is spanned by the polar angle and the azimuthal angle, the latter is measured between the projection of the unit vector $\hat{s}$ of the direction vector S and an arbitrary axis on the base surface dA. Consequently the solid angle can be expressed as a function of the polar angle and the azimuthal angle, describing an infinitesimal surface element on the unit hemisphere as given by Eq. 1.2.

$$d\Omega = \sin\Theta d\Theta d\Psi \tag{1.2}$$

In summary the three descriptive angle definitions are listed below:

- solid angle Ω: *The solid angle is similar to a planar angle by definition, but is given in three dimensional space. [...] The solid angle is the ratio of base area to the square of the chord length.* [4]
- azimuthal angle Ψ: measured between an arbitrary axis (usually measured from the x-axis) on the surface and the projection of $\hat{s}$ onto the surface
- polar angle or zenith Θ: *measured from the surface normal to* $\hat{n}$ [3]

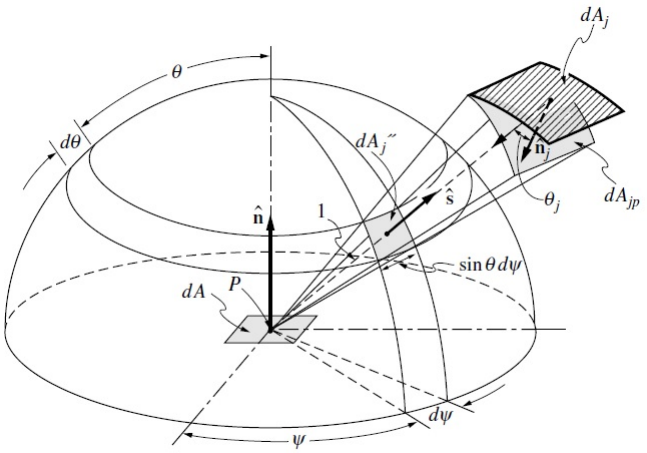

Figure 1.2.: *Emission direction and solid angles as related to a unit hemisphere* [3]

One of the most important parameters for the radiative heat transfer is the radiative intensity, in its spectral Eq. 1.3 or total (integral over all wavelengths) Eq. 1.4 form: [3]

$$I_\lambda = \frac{\text{radiative energy flow}}{\text{time} \cdot \text{area normal to ray} \cdot \text{solid angle} \cdot \text{wavelength}} \tag{1.3}$$

$$I = \frac{\text{radiative energy flow}}{\text{time} \cdot \text{area normal to ray} \cdot \text{solid angle}} \tag{1.4}$$

Specifically, the spectral intensity refers to radiation in an interval $d\lambda$ around a single wavelength, while the total intensity refers to combined radiation including all wavelengths. [4]

1.2. Radiation characteristics

In order to describe the energy loss in radiation the terms scattering, described by the scattering coefficient σ_S, and absorption, described by the absorption coefficient κ_a, are introduced. Scattering of radiation can occur due to following mechanisms as illustrated in Fig. 1.3:

- diffraction: altering of the photon path without collision
- reflection: change in direction the photon travels
- refraction: penetration of the photon into the particle

Absorption describes the penetration of an electromagnetic wave into a particle. The extinction coefficient β expresses the decrease in radiation due to absorption

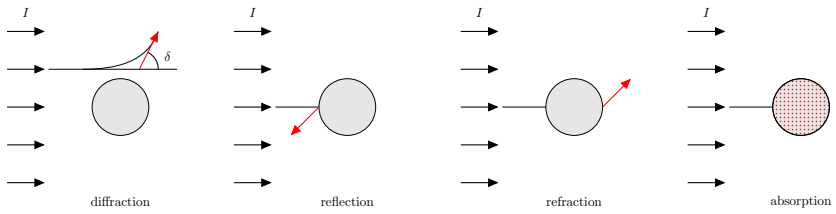

Figure 1.3.: Interaction of electromagnetic wave with a particle [3]

and scattering losses. It is a physical property and therefore dependent on the wavelength λ as well as other local properties.

$$\beta = \kappa_a + \sigma_S$$

The scattering phase function describes the probability of a ray from one direction being scattered into another by an angle θ. The relative importance of scattering is given by the single scattering albedo as following, whereas $\omega = 0$ relates to zero scattering and $\omega = 1$ pure scattering (no absorption).

$$\omega = \frac{\sigma_S}{\kappa_a + \sigma_S} = \frac{\sigma_S}{\beta}$$

Two major difficulties make the study of radiation transfer in absorbing, emitting, and scattering media quite challenging. The first difficulty is the spatial variation in radiative properties throughout the medium; absorption, emission,

and scattering can occur at all locations within the medium at different strengths depending on the concentration of gases and local temperature variations. A complete solution for energy exchange requires knowing the radiation intensity, temperature, and physical properties throughout the medium. The mathematics describing the radiative field is inherently complex. A second difficulty is that spectral effects are often much more pronounced in gases, translucent solids, and translucent liquids than for solid surfaces, and a detailed spectrally dependent analysis may be required. Most of the simplifications introduced for solving radiation problems in gases and other translucent materials are aimed at decreasing one or both of these complexities. [4]

1.3. The radiative transport equation

The RTE in general form can be written as [3]:

$$\frac{dI}{ds} = \kappa I_b - \kappa I - \sigma_S I + \frac{\sigma_S}{4\pi} \int_{4\pi} I(\hat{s_j}) \Phi(\hat{s_j}, \hat{s}) d\Omega_j \tag{1.5}$$

The term on the left-hand-side describes in general the change of radiative intensity I in space s. Whereas the right-hand-side describes the cause for those changes, induced due to emission, scattering and absorption of radiation. The term I_b denotes the blackbody intensity which links, according to Planck's law, the temperature influence on the emission spectrum and energy of a body [4]. The last term describes the increase of radiative intensity from other directions, indicated by the index j [3]. In this context the scattering phase function Φ is given, which describes the probability of a ray being scattered from one direction in another.

2. Solution methods for the radiative transfer equation

This section gives a brief overview of existing and well established solution methods for the radiative transfer equation. It has been deliberately summarized, as the main focus of this thesis rests upon the implementation of the LBM presented in the upcoming Ch. 3. There are various different methods to solve the RTE, most of which are given in Fig. 2.1.

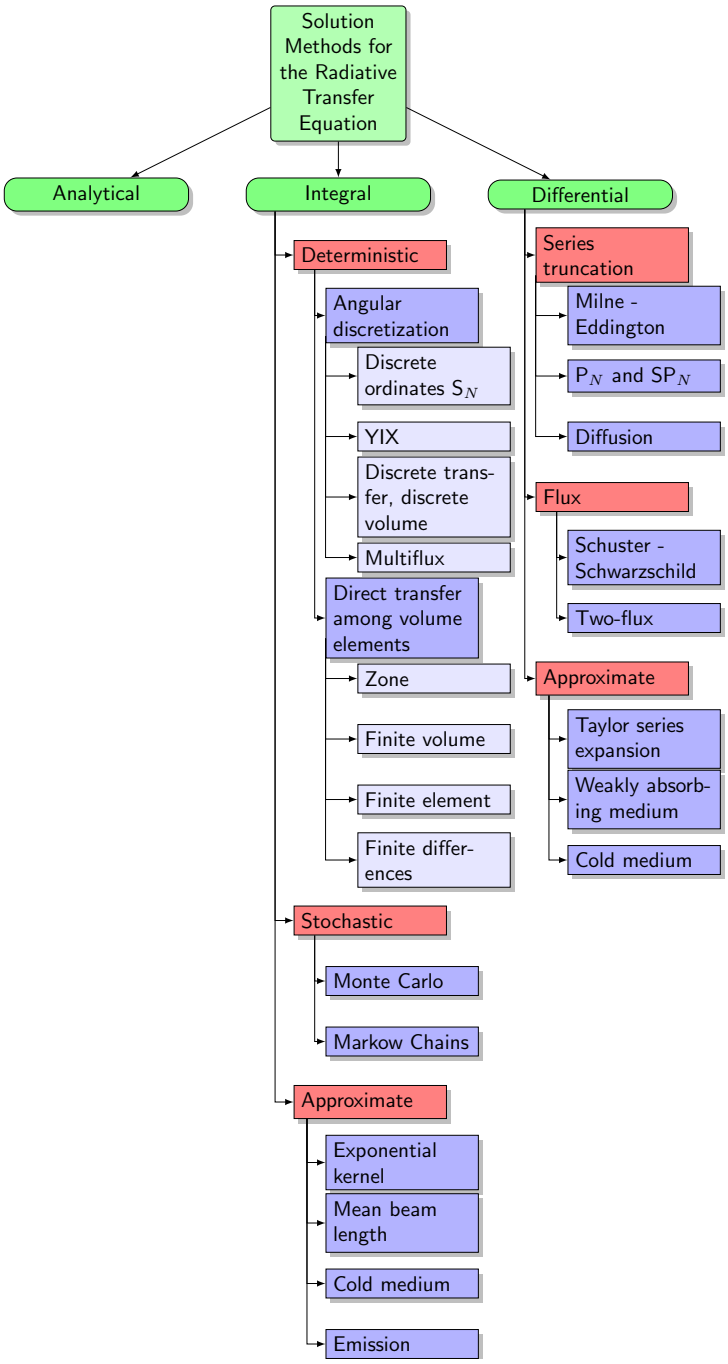

Figure 2.1.: Solution methods for the radiative transfer equation [4]

Of those solution methods presented in Fig. 2.1 only a few are suited for the simulation of the radiative heat transfer in furnaces. This restriction is due to the various assumptions that have to be made in order to use these methods. Figure 2.2 gives an abstracted overview of the established methods in solving the RTE in furnace simulations in which the LBM has been marked as a possible future solution method.

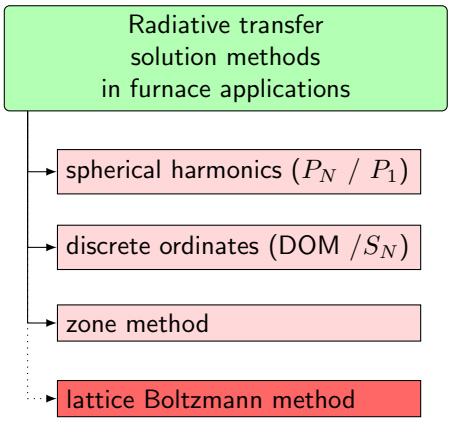

Figure 2.2.: Overview of different radiative solution methods used in furnace simulation

2.1. Method of spherical harmonics

Basis for the P_N approximation forms the radiative intensity field $I(\mathbf{r}, \hat{\mathbf{s}})$, which represents the location of the radiative intensity I at the position $\mathbf{r}$ as a function of a scalar expressed through a generalized Fourier series.

$$I(\mathbf{r}, \hat{\mathbf{s}}) = \sum_{l=0}^{\infty} \sum_{m=-l}^{l} I_l^m(\mathbf{r})\, \Upsilon_l^m(\hat{\mathbf{s}}) \tag{2.1}$$

The sub- and superscripts l and m denote the positional dependency of the coefficient, the spherical harmonics are given by the term $\Upsilon_l^m(\hat{\mathbf{s}})$, which can be expanded to,

$$\Upsilon_l^m(\Theta, \Psi) = \begin{cases} \cos(m\Psi)\, P_l^m(\cos\Theta), & \text{for} \quad m \geq 0 \\ \sin(|m|\Psi)\, P_l^m(\cos\Theta), & \text{for} \quad m < 0 \end{cases} \tag{2.2}$$

in which the associated Legrende polynomials P_l^m were introduced.

$$P_l^m(\mu) = (-1)^m \frac{(1-\mu^2)^{\frac{|m|}{2}}}{2^l l!} \frac{d^{l+|m|}}{d\mu^{l+|m|}} \left(\mu^2 - 1\right)^l \tag{2.3}$$

Substitution of the radiative intensity given by Eq. 2.1 in the RTE yields,

$$\hat{\mathbf{s}} \cdot \nabla_\tau I + I = (1-\omega) I_b + \frac{\omega}{4\pi} \int_{4\pi} I(\hat{\mathbf{s}}) \Phi(\hat{\mathbf{s}} \cdot \hat{\mathbf{s}}') \, d\Omega' \tag{2.4}$$

This leads to an infinite number of partial differential equation (PDE) which is simplified by the truncation of the series in Eq. 2.1. The highest level of the coefficient l is eponymous for the method. The most common form of the P_N method is the lowest order approximation, namely the P1 approximation.
An excerpt of examples of the usage of the P1 method is subsequently given. For instance Kuang et al. [5] applied the P1 method in solving the radiative heat transfer in a coal fired furnace in regards to lowering NO_x emissions. Zhang et al. [6] applied the P1 method to study the heat transfer in a regenerative slab reheating furnace.

2.2. Discrete ordinates method

Similar to the previously presented P_N method, the discrete ordinates method (DOM) or S_N approximation transforms the RTE into a set of PDEs [3]. The RTE is solved for n different directions as follows,

$$\hat{\mathbf{s}}_i \cdot \nabla I(\mathbf{r}, \hat{\mathbf{s}}_i) = \kappa(\mathbf{r}) I_b(\mathbf{r}) - \beta(\mathbf{r}) I(\mathbf{r}, \hat{\mathbf{s}}_i) + \frac{\sigma_s(\mathbf{r})}{4\pi} \underbrace{\sum_{j=1}^{n} w_j I(\mathbf{r}, \hat{\mathbf{s}}_j) \Phi(\mathbf{r}, \hat{\mathbf{s}}_j, \hat{\mathbf{s}}_i)}_{*} \tag{2.5}$$

The directional integrals (marked by an asterisk) over the hemisphere have been replaced by numerical quadrature in Eq. 2.5. Using the DOM requires discretisation of the entire solid angle (4π) along a finite number of directions. Weight factors (w_j) correspond to the solid angle increments. The discretisation

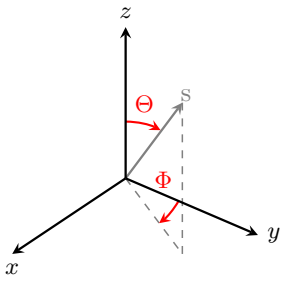

Figure 2.3.: Angular coordinate system [9]

is done using angular quadrature, thus conservation of energy cannot be ensured [7] [8]. Angular discretisation has a major influence on the gained results, as the angular space of 4π is discretized into $N_\Theta \times N_\Phi$ solid angles. *The angles* Θ *and* Φ *are the polar and azimuthal angles respectively, and are measured with respect to the global Cartesian system* (x, y, z) *[...]. The* Θ *and* Φ *extents of the control angle,* $\Delta\Theta$ *and* $\Delta\Phi$*, are constant. In two-dimensional calculations, only four octants are solved due to symmetry, making a total of* $4N_\Theta N_\Phi$ *directions in all. In three-dimensional calculations, a total of* $8N_\Theta N_\Phi$ *directions are solved.* [9] Increasing discretisation leads to an increase of accuracy, however, at a high computational cost.
A vast majority of publications upon the issue of radiative heat transfer modelling in industrial furnaces is currently based on the DOM. Morgado et al. [10] analysed a walking beam furnace using the DOM. Prieler et al. [2] investigated the heating characteristics of steel billets using the DOM in a walking hearth furnace. Furthermore Landfahrer et al. [11], [12], Han et al. [13] as well as Tang et al. [14] investigated reheating furnaces using the DOM.

2.3. Zone method

In this method the enclosure is subdivided into a finite number of isothermal volume and surface area zones. An energy balance is then performed for the radiative exchange between any two zones, employing pre-calculated 'exchange areas.' This process leads to a set of simultaneous equations for the unknown temperatures or heat fluxes. [3]
The zoning procedure is illustrated in Fig. 2.4 for an arbitrary enclosure, at

which the enclosure was subdivided into n isothermal zones of temperature T_n and emissivity ε_n. At the heart of the zone method lie the generic exchange

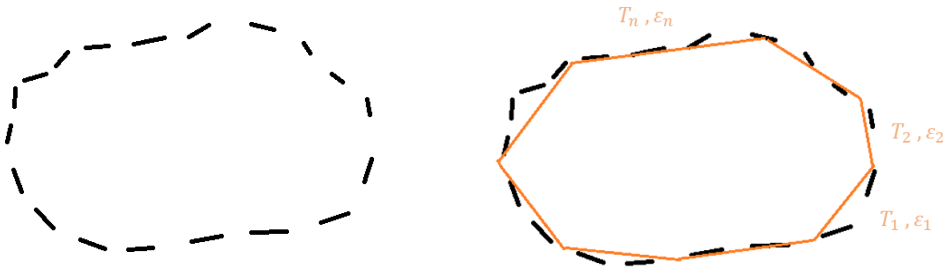

Figure 2.4.: Zonal method: arbitrary surface enclosure (left), subdivided by isothermal surfaces (right)

factors, which can be distinguished in three subcategories, namely the energy exchange between:

- two volume elements,
- a volume element and a surface element, and
- two surface elements.

The exchange factor forms the correlation between the emitted radiation of a surface or volume element and the amount of absorbed or scattered radiation on the second surface or volume element [15]. Due to the complex derivation of the zone method, which is also known as zonal method in literature, the derivation of selfsame is at this point forgone, thus referring to [3], [4], [15] for further information.
First advances using the zone method could be achieved by Li [16]. Wu et al. [17] used the zone method to simulate the heat transfer in a roller-hearth furnace. Recent work has been done by Ebrahimi et al. [18] who compared the solution of radiative heat transfer in a furnace with the P1-approximation, in particular the effect of the flame position on the furnace performance.

3. Radiative heat transfer - lattice Boltzmann method

The LBM has been developed in the last couple of decades as a versatile tool for conventional computational fluid dynamics (CFD) applications, however, the usage for thermal or radiative heat transfer simulation is still at an early stage of development. As the computing of radiative information is the most time consuming component [19], due to the physically fast progression of radiation, there is a need for minimizing the computing time. Existing methods such as previously described in chapter 2 already have the potential to solve the radiative transfer equation, however it is expected that by applying the LBM the computational costs can be drastically improved [19].
The expected advantage of using the LBM over existing methods such as the DOM or P1 model, is justified by the fundamental simple parallelisation principle of the method, and thus anticipating a reduced computational effort. Subsequently, a brief overview regarding existing publications on the subject is given.

3.1. Introduction to the lattice Boltzmann method

The Boltzmann transport equation origins from the Austrian physicist Ludwig Eduard Boltzmann (1844-1906) and his research on kinetic theory (a mesoscopic theory). The description of the theory is motivated by the different levels of approach often encountered in context with fluids. In general three possible descriptive levels are applicable, namely the microscopic, mesoscopic and macroscopic descriptions, which are illustrated in Fig. 3.1. Using a microscopic

approach molecular descriptions (e.g molecular dynamics (MD)) are of interest, whereas the macroscopic approach is set up on a continuum level with respective quantities (e.g. CFD), such as density or velocity. The mesoscopic approach constitutes an intermediate level in between the microscopic and macroscopic scale. The quantity of interest are distributions or representative collections of molecules. A well known example for the macroscopic level would be the Navier-Stokes equations (NSE) used in fluid dynamics. On the microscopic level the Newton's dynamics are accordingly used [20].

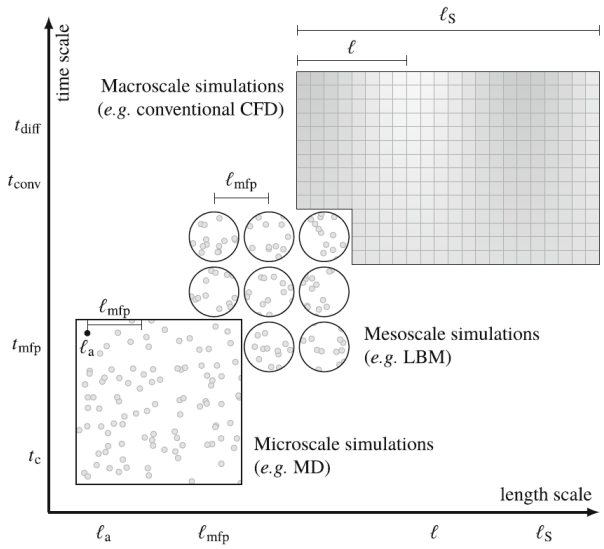

Figure 3.1.: *The hierarchy of length and time scales in typical fluid dynamics problems. Depending on the level of details required, different simulation techniques are suitable* [20]

The LBM itself provides a similar approach independently from the problem under consideration. One considers a basic quantity (e.g. velocity) which is represented by a particle distribution function (PDF) $f(x, c, t)$. The PDF considers a statistical description of the system of molecules in space x, travelling with the velocity c in time t. If an external force F acts on the molecules a change in the PDFs position and velocity is expected. The number of molecules prior to the collision is the same as after, if no collisions between the molecules

occur, as stated in Eq. 3.1.

$$\underbrace{f\left(x+cdt, c+Fft, t+dt\right)dxdc}_{post-collision} - \underbrace{f\left(x,c,t\right)drdx}_{pre-collision} = 0 \tag{3.1}$$

Though if collisions occur between the molecules, the collision term Γ is introduced, which describes the rate of change between the initial and final state of the PDFs.

$$f\left(x+cdt, c+Fdt, t+dt\right)dxdc - f\left(x,c,t\right)drdx = \Gamma(f)dxdcdt \tag{3.2}$$

Dividing Eq. 3.2 by $dxdcdt$ and writing the limit $(dt \to 0)$ for the PDF leads to,

$$\frac{df}{dt} = \Gamma(f) \tag{3.3}$$

The change of the PDF can be expanded as follows,

$$df = \frac{\partial f}{\partial r}dr + \frac{\partial f}{\partial c}dc + \frac{\partial f}{\partial t}dt \tag{3.4}$$

Division of Eq. 3.4 by dt yields,

$$\frac{df}{dt} = \frac{\partial f}{\partial x}\underbrace{\frac{dx}{dt}}_{c} + \frac{\partial f}{\partial c}\underbrace{\frac{dc}{dt}}_{a=\frac{F}{m}} + \frac{\partial f}{\partial t} = \Gamma(f) \tag{3.5}$$

The Boltzmann equation is written according to [21] as following,

$$\frac{\partial f}{\partial t} + c\frac{\partial f}{\partial x} + \frac{F}{m}\frac{\partial f}{\partial c} = \Gamma\left(f\right) \tag{3.6}$$

in which the first term on the left-hand-side denotes the temporal change of the quantity f under consideration, whilst the second term represents the spatial change of the quantity associated with the velocity c. The third term on the left-hand-side represents the specific body forces F/m. Thus Eq. 3.6 can be seen as an advection equation. The term on the right-hand-side Γ is a source term representing the redistribution of the PDF caused by collisions, hence, declared as the collision operator. Discretisation of the Boltzmann equation in velocity space, physical space, and time, renders the lattice Boltzmann equation as follows,

$$f_i\left(x + c_i\Delta t, t+\Delta t\right) = f_i\left(x,t\right) + \Omega_i\left(x,t\right) \tag{3.7}$$

in which the index i denotes the different lattice directions. The transport of the PDF along the lattice directions is organised through the so-called lattice arrangements, in which each discrete PDF gets assigned to a specific direction vector as illustrated in Fig. 3.2. Details on the lattice arrangements are given in Sec. 3.7. The differences in modelling physical quantities with the above

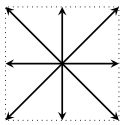

Figure 3.2.: Exemplary lattice arrangement used for the transport of particle distribution functions

described equation lie in the formulation of the collision term Ω_i, as well as the appending of necessary source terms if needed. The working principle of the LBM is characterised by a collision and streaming step of the quantity under consideration (see Fig. 3.3).

Figure 3.3.: Schematics of the pre- and post-collision PDFs

By observing a representative distribution of the quantity of interest in the lattices nodes, and applying the above described steps for information exchange a versatile algorithm can be developed. Pertaining to the information exchange steps, the streaming step describes the broadcast in a specific direction, whilst the collision step is a mechanism that prevents a particle from infinite following a ray path. [22]
The collision operator Γ respectively Ω_i can be modelled in various ways, thus, only the most commonly used Bhatnagar-Gross-Krook (BGK) collision operator is introduced. *The main difficulty in handling the full Boltzmann equation arises from the complicated nature of the collision terms* [23]. Each collision term handles two parts, the first representing the removed and absorbed particle, the second representing collision caused emission of particles. The emission

term is replaced in the BGK model *by a term representing a Maxwellian distribution of the emitted particles* [23], thus allowing conservation of the required quantities.

$$\Omega_i = \frac{(f_i^{eq} - f_i)}{\tau_i} \tag{3.8}$$

As evident in Eq. 3.8 the model is a single-relaxation-time (SRT) model and thus the relaxation constant τ_i can be related to the problem under consideration, using the Chapman-Enskog (C-E) analysis. The C-E analysis is in general terms used to determine a connection between the lattice Boltzmann equation (LBE) and the macroscopic equation. *The Chapman–Enskog expansion is a vehicle to derive macroscopic equations from stream and collide equations. This is a crucial step of the LBM development, since it is not guarantied or even clear whether the computations in mesoscale generate suitable solutions of macroscopic target equations or not [sic!].* [24]
Due to the complex nature of the C-E the reader is referred to the appendix A for the RTE and appendix B for the energy equation for details.

3.1.1. Literature overview of modelling the radiative transfer equation using the lattice Boltzmann method

The quantity of interest for solving the RTE is the radiation intensity, more precisely the intensity or PDF of selfsame in lattice nodes. Currently two different approaches towards the modelling of radiative transport with the LBM exist, namely the *phenomenological approach* and the *direct discretisation approach*. The former proposes kinetic equations heuristically and has been previously used in lighting simulations by Geist et al. [25]. The information is transported in time and space using a Markovian update, at which, following a 'Markov chain', the probability of a PDF being deflected in any direction is uninfluenced by prior events [4]. The latter derives kinetic equations by analogy to classical discretisation of the Boltzmann equation, as previously described in section 3.1, and is amongst others widely used in thermal heat radiation transfer.
First advances in radiation heat transfer modelling using the LBM were made by Mishra et al. [26]–[31]. Major advances followed upon the publication of Ma et al. [32] who successfully derived a macroscopic conservation of radiation

energy and momentum on basis of radiation hydrodynamics (Note: radiation hydrodynamics describe the effects of radiation on the dynamics of fluids. [33]). Up until this moment the computed results for the RTE were tied to the meso-scale. The derivation of macroscopic equations is rather difficult to achieve and to review using analytical solutions for proper error analysis [24]. The majority of existing publications at the moment is restricted to one- or two-dimensional examples involving various assumptions concerning scattering and angular discretisation [29], [34]–[36]. The first publication on three-dimensional radiative LBM application was written by Mink et al. [24], regarding the light simulation in participating media using a derivation strongly linked to the P1 method. Another practical approach was presented by McCulloch and Bindra [22], [37] who successfully showed the application of a RTE based LBM in multi-physics problems.
The sections 3.2 and 3.3 are intended to highlight two methods considering radiative transfer in participating media. The method by McCulloch and Bindra [37], hereinafter denoted as 'Method 1', was selected as it provides an up-to-date profound basis for further coupling in multi-physics problems. The method by Asinari et al. [19], subsequently denoted as 'Method 2', was chosen as a reference solution. Both methods were developed in view of the rather inconvenient, in terms of computational expenses, existing modelling methods for high temperature processes.

3.2. Method 1

The first method described is based upon a derivation of the LBE developed by [32], without explicitly providing of a conservation of the macroscopic quantities. However [37] provided a simple and economical approach to couple the RTE with the energy equation to observe the temperature influence on the radiation intensity. The radiative transfer equation for non-equilibrium monoenergetic radiative transfer can be written as [37]:

$$\frac{\partial I\left(\mathbf{r},\mathbf{\Omega},t\right)}{\partial t}+\mathbf{\Omega}\nabla I\left(\mathbf{r},\mathbf{\Omega},t\right)=\kappa_a\left[\frac{1}{4\pi}\sigma T\left(\mathbf{r},t\right)^4-I\left(\mathbf{r},\mathbf{\Omega},t\right)\right]+\sigma_S\left[\frac{1}{4\pi}\int_{4\pi}I\left(\mathbf{r},\mathbf{\Omega},t\right)d\mathbf{\Omega}-I\left(\mathbf{r},\mathbf{\Omega},t\right)\right]+S\left(\mathbf{r},\mathbf{\Omega},t\right) \quad (3.9)$$

The terms on the left-hand-side describe the changes in the radiative field due to temporal and spatial effects. Whereas the terms on the right-hand-side associated with κ_a represent the radiative source and sink due to absorption, and those associated with σ_S represent the same due to scattering. The remaining term S describes all additional sources.
According to [22] the inter-particle collision rate is negligible, therefore the collision operator for radiative transport is linear and may be described by absorption and scattering integrals. The above described Eq. 3.9 was subsequently derived to a LBM formulation.

3.2.0.1. From the Boltzmann equation of photon transfer to the radiative transfer lattice Boltzmann equation

The foundation amongst many publications concerning the modelling of radiative transfer using the LBM is an article written by Ma et al. [32], details are given in appendix A. Through derivation of the macroscopic conservation equations of radiation energy and radiation momentum from the radiation hydrodynamics and eulerian equations Ma et al. developed a LBM for radiative transfer (Eq. 3.10) in a uniform refractive index medium without scattering. Selfsame is a two step model based on the macroscopic conservation equations and a C-E expansion method.

$$I_{\nu,\Omega}\left(\mathbf{r}+c\mathbf{\Omega}\Delta t, t+\Delta t\right) - I_{\nu,\Omega}\left(\mathbf{r},t\right) = -\frac{1}{\tau}\left[I_{\nu,\Omega}\left(\mathbf{r},t\right) - I^{eq}_{\nu,\Omega}\left(\mathbf{r},t\right)\right] + S_{\nu,\Omega}\left(\mathbf{r},t\right)\Delta t + w_{\Omega} I_{\nu,\Omega}\left(\mathbf{r},t\right)\Delta t \quad (3.10)$$

3.2.1. One-dimensional cartesian radiative transfer lattice Boltzmann equation

The following sections describe the method developed by McCulloch and Bindra [37][22].

Assuming a steady state situation the one-dimensional form Eq. 3.9 can be formulated as following:

$$\mu \frac{dI(x,\mu)}{dx} = \kappa_a \left[\frac{1}{2} \sigma T(x)^4 - I(x,\mu) \right] + \sigma_S \left[\int_{-1}^{1} I(x,\mu) d\mu - I(x,\mu) \right] + S(x,\mu) \quad (3.11)$$

The factor μ describes the directional cosine of the azimuthal direction. Note that the factor $\frac{1}{2}$ (in two-dimensional applications $\frac{1}{4\pi}$) is an arbitrary constant [3]. Introducing non-dimensional variables is the first step in order to receive the desired LBE.

$$r_x = \frac{\beta x}{\tau_W} \quad \tau_W = \beta W \quad \widetilde{T} = \frac{T}{T_{ref}} \quad \chi = \frac{I}{\sigma T_{ref}^4} \quad S^* = \frac{S}{\sigma T_{ref}^4} \quad (3.12)$$

r_x represents the non-dimensional optical thickness in direction x (Note: the definition of selfsame can vary on the chosen scaling W), Ψ is the dimensionless radiative heat flux.
The scattering albedo is defined as $\omega = \frac{\sigma_S}{\kappa_a + \sigma_S}$. By definition $\kappa_a = \beta - \sigma_S$, with β being the extinction coefficient. [3]
Hence the RTE can be written as:

$$\mu \frac{d\chi}{dr_x} = \tau_W \left[(1-\omega) \frac{\widetilde{T}^4}{2} - \chi + \frac{\omega}{2} \int_{-1}^{1} \chi d\mu + \frac{1}{\beta} S^* \right] \quad (3.13)$$

The equivalent LBE in the discrete direction i, neglecting volumetric energy sources, and thus, implying radiative equilibrium is:

$$f_i(r_x + c_{i,r_x} \Delta t, t + \Delta t) = f_i(r_x, t) + \Delta t \beta W \left(w_i (1-\omega) \widetilde{T}^4 - f_i(r_x, t) + \omega w_i \sum_j f_j(r_x, t) \right) \quad (3.14)$$

The non-dimensional radiative intensity χ has been replaced by the PDF f_i representing the radiative intensity in the discrete direction i. The lattice arrangements weights are represented by w_i as described in the section 3.7. The scattering integral has to be approximated by numerical quadrature.
As the developed LBE formally lacks of an equilibrium term, it is difficult to apply a C-E analysis to ensure macroscopic conservation of the quantities of interest.

3.2.2. Two-dimensional cartesian radiative transfer lattice Boltzmann equation

The two-dimensional LBE of the RTE is rather similar to Eq. 3.14 in which $\vec{r}$ represents the non-dimensional optical thickness in the x- and y-direction.

$$f_i\left(\vec{r}+\vec{c}_i\Delta t, t+\Delta t\right) = f_i\left(\vec{r},t\right) + \Delta t\beta W\left(w_i\left(1-\omega\right)\widetilde{T}^4 - f_i\left(\vec{r},t\right) + \omega w_i\sum_j f_j\left(\vec{r},t\right)\right) \quad (3.15)$$

The computational collision and streaming step can now be derived from Eq. 3.15 as following:

$$f_i^*\left(\vec{r},t\right) = f_i\left(\vec{r},t\right) + \Delta t\beta W\left(w_i\left(1-\omega\right)\widetilde{T}^4 - f_i\left(\vec{r},t\right) + \omega w_i\sum_j f_j\left(\vec{r},t\right)\right) \quad (3.16)$$

$$f_i\left(\vec{r}+\vec{c}_i\Delta t, t+\Delta t\right) = f_i^*\left(\vec{r},t\right) \quad (3.17)$$

3.3. Method 2

This section describes the method developed by Asinari et al. [19]. The second method uses a different approach to resolve the RTE in their LBE formulation and thus conserves the macroscopic quantities of interest by nature. Based on this work Mishra et al. [31] recently published a one-way coupling approach to solve the conduction-radiation heat transfer using the LBM.

The derivation for the LBE starts once again from the RTE as given by [3], where $\beta = \kappa_a + \sigma_S$.

$$\frac{dI}{ds} = \hat{s}\cdot\nabla I = -\beta I + \kappa_a I_b + \frac{\sigma_S}{4\pi}\int_{4\pi} Ip\left(\Omega,\Omega'\right)d\Omega' \quad (3.18)$$

Under the assumption of isotropic scattering ($p\left(\Omega,\Omega'\right)=1$) and the application of a radiative equilibrium condition Eq. 3.18 can be written as given in Eq. 3.19.

The radiative equilibrium condition implies that incoming and outgoing energy are in balance [38], whereas radiation is the primary mechanism of energy transfer [4], which implies that the volumetric emission $4\pi I_b$ equals the volumetric absorption G. In doing so the radiative heat flux and its divergence are zeroised, thus the following relation $\nabla \cdot \vec{q_R} = \kappa_a(4\pi I_b - G) \stackrel{!}{=} 0$ allows further calculation [34].

$$\frac{dI}{ds} = \hat{s} \cdot \nabla I = \beta \left(\frac{G}{4\pi} - I \right) \tag{3.19}$$

and respectively for the discrete directions i:

$$\frac{dI_i}{ds} = \hat{s} \cdot \nabla I_i = \beta \left(\frac{G}{4\pi} - I_i \right) \tag{3.20}$$

The transient form of the RTE can be written in analogy to [3]:

$$\frac{1}{c}\frac{\partial I_i}{\partial t} + \hat{s} \cdot \nabla I_i = \beta \left(\frac{G}{4\pi} - I_i \right) \tag{3.21}$$

As radiation is a three-dimensional phenomenon, but the solution sought for is in the two-dimensional space, isotropy has to be assumed. *Further since we are constrained to be in the solution plane and have to cover all directions now confined to the solution plane, at any point, for the radiation contained in the* 4π *spherical space, we assume isotropy in the polar direction* Θ $(0 \leq \Theta \leq \pi)$ *[...] and thus we consider angular dependence of intensity only in the azimuthal direction* Ψ $(0 \leq \Psi \leq 2\pi)$. [19]. Figure 3.4 gives the geometrical context for the statement above. Weights have to be applied in each discrete direction i for the streaming PDF, in order to enforce the isotropy conditions. The corresponding weights are computed using Eq. 3.51 as described in section 3.7.
Assuming that the generic component of the lattice equals the fictitious speed of light ($\vec{c_i} = c$) the RTE can be written as:

$$\frac{\partial I_i}{\partial s} + \vec{c_i} \cdot \nabla I_i = \frac{D_i I_i}{Dt} = c_i \beta \left(\frac{G}{4\pi} - I_i \right) \tag{3.22}$$

Integrating the above equation leads to the following equation,

$$I_i\left(\vec{r} + \vec{c_i}\Delta t, t + \Delta t\right) = I_i\left(\vec{r}, t\right) + \Delta t c_i \beta \left(\frac{G}{4\pi} - I_i \right) \tag{3.23}$$

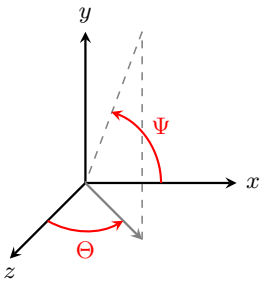

Figure 3.4.: Coordinate system used based on [19]

Next the relaxation time τ_i is introduced. As the PDF between the lattice nodes is transferred through collision and streaming steps, the relaxation time describes the duration until the equilibrium state after the collisions step is reached. It can be seen as a scale in terms of strength of the diffusion process.

$$\tau_i = \frac{1}{c_i \beta} \tag{3.24}$$

The key difference here is that τ_i is a straightforward function of the transport coefficient β, which is already defined in the original physical problem given by Eq. 3.19, and hence there is no need to introduce any asymptotic expansion technique (e.g. Chapman-Enskog). Moreover, even though different τ_i are used for different azimuthal directions, this formulation is still substantially based on a single-relaxation-time approach, because the differences among τ_i are due to differences among the magnitudes of the lattice velocities c_i, which are purely geometrical parameters prescribed by the considered lattice. Summarizing, the relaxation times τ_i depend on combinations of the physical parameter β and lattice-dependent geometrical parameters c_i , according to Eq. 3.24. [19]
f_i represents the particle distribution function and it is the carrier for radiative energy, whereas $\frac{G}{4\pi} = I^{eq}$ is the equilibrium particle distribution function. Thus Eq. 3.23 can be written as:

$$f_i\left(\vec{r} + \vec{c}_i \Delta t, t + \Delta t\right) = f_i\left(\vec{r}, t\right) + \frac{\Delta t}{\tau_i}\left[f_i^{eq}\left(\vec{r}, t\right) - f_i\left(\vec{r}, t\right)\right] \tag{3.25}$$

In order to compute the equilibrium particle distribution function the before mentioned weights are needed, whereat in Eq. 3.26 i represents the lattice link

and M is the total number of discrete directions.

$$f_i^{eq} = \sum_{i=1}^{M} f_i w_i \tag{3.26}$$

Collision step:

$$f_i^* \left(\vec{r}_n, t\right) = f_i \left(\vec{r}_n, t\right) + \frac{\Delta t}{\tau_i} \left[f_i^{eq} \left(\vec{r}_n, t\right) - f_i \left(\vec{r}_n, t\right)\right] \tag{3.27}$$

Streaming step:

$$f_i \left(\vec{r}_n + \vec{c}_i \Delta t, t + \Delta t\right) = f_i^* \left(\vec{r}_n, t\right) \tag{3.28}$$

3.4. Solving the energy equation using the lattice Boltzmann method

The energy equation is modelled using the LBM on basis of an advection-diffusion equation (ADE) or convection-diffusion equation (CDE) as given by [20]:

$$\frac{\partial T}{\partial t} + \nabla \left(Tu\right) = \alpha \nabla^2 T + q \tag{3.29}$$

The first term on the left-hand-side of Eq. 3.29 describes the temporal change of temperature, the second term describes the spatial change due to convection. The first term on the right-hand-side describes the spatial change due to conduction and the last term includes source terms. The parameter α in the conduction term describes the thermal diffusivity of the medium and is related via the thermal conductivity k, the specific heat capacity c_P and the materials density ρ as follows,

$$\alpha = \frac{k}{\rho \cdot c_P} = const. \tag{3.30}$$

The corresponding 'standard' LBM algorithm for a discrete direction i is given by Eq. 3.31.

$$g_i \left(\mathbf{r} + \mathbf{c}_i \Delta t, t + \Delta t\right) - g_i \left(\mathbf{r}, t\right) = \Omega_i \left(\mathbf{r}, t\right) + Q_i \left(\mathbf{r}, t\right) \tag{3.31}$$

The simplest collision model is given by the BGK operator as following (cf. appendix B):

$$\Omega_i(\mathbf{r},t) = -\frac{1}{\tau_g}\left(g_i(\mathbf{r},t) - g_i^{eq}(\mathbf{r},t)\right) \tag{3.32}$$

An approach for the relaxation-time-term (see Eq. 3.33 for a two-dimensional problem) has been proposed in [27], including physical properties of the medium through the thermal diffusivity given by α.

$$\tau_g = \frac{3\alpha}{U^2} + \frac{\Delta t}{2} \tag{3.33}$$

The propagation (or lattice) speed U is defined as $U = \frac{\Delta x}{\Delta t}$, whereat Δx denotes the distance between the nodes and Δt represents the time step. The equilibrium distribution function g_i^{eq} is given according to [20] following a linear approach.

$$g_i^{eq} = w_i^m \widetilde{T} \tag{3.34}$$

The non-dimensional temperature itself is computed as the sum of discrete temperature distribution functions (TDF) as illustrated in Fig. 3.5.

$$\widetilde{T} = \sum_i g_i \tag{3.35}$$

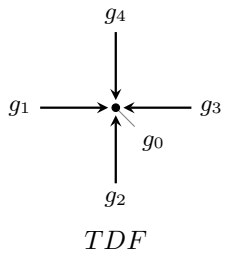

Figure 3.5.: Composition of the temperature distribution function for the D2Q5 lattice arrangement

3.5. Coupling of the energy and radiative transfer lattice Boltzmann equations

The presented methods are different in modelling the radiative source term in the energy equation. The Stark number N, which is also known in literature as conduction-radiation-parameter, forms an important parameter in the coupling of the energy equation and RTE [4].

$$N = \frac{\beta k}{4\sigma T_{ref}^3} \tag{3.36}$$

The conduction-radiation-parameter relates the extinction coefficient β and the thermal conductivity k with the Boltzmann constant σ and the reference temperature T_{ref}. *The N does not directly give the relative values of conduction to emission because the ratio of these values depends on both temperature difference and temperature level.* [4]
For high values of N, conduction is the dominating heat transfer mechanism, whereas for small values of N, radiation dominates. [39]

3.5.0.1. Method 1

The set of non-dimensional variables used for the energy equation is given below, for the temperature $\widetilde{T}$, intensity χ and space $\vec{r}$.

$$r_x = \frac{\beta x}{\tau_W} \quad r_y = \frac{\beta y}{\tau_W} \quad \tau_W = \beta W \quad \widetilde{T} = \frac{T}{T_{ref}} \quad \chi = \frac{I}{\sigma T_{ref}^4} \tag{3.37}$$

The source term in Eq. 3.31 was derived from the dimensionless energy equation 3.29 as following,

$$\rho C_p \frac{\partial T(r,t)}{\partial t} + \rho C_p u \nabla T = \nabla (k \nabla T) + \underbrace{\kappa_a \left[\int_{4\pi} I(r,\Omega,t)\, d\Omega - \sigma T(r,t)^4 \right]}_{*} \tag{3.38}$$

in which the radiative source term is given for a non-scattering medium, thus, only the absorptive terms (marked by an asterisk) of the RTE given by Eq. 3.9

are left. Regarding a steady state medium in the two-dimensional space Eq. 3.38 is reduced to:

$$k\left(\frac{d^2T}{dx^2}+\frac{d^2T}{dy^2}\right)=\kappa_a\left(\sigma T^4-\int_{\Omega=4\pi} I\left(x,y,\Omega\right)d\Omega\right) \tag{3.39}$$

Thus, the energy equation can be written as:

$$\frac{d^2\Theta}{dr_x^2}+\frac{d^2\Theta}{dr_y^2}=\frac{\kappa\sigma T_{ref}^3}{k}W^2\left(\Theta^4-\int\chi d\Omega\right) \tag{3.40}$$

In case of a non-scattering medium and by setting $W=\kappa^{-1}$ the right-hand-side is simplified to:

$$\frac{d^2\Theta}{dr_x^2}+\frac{d^2\Theta}{dr_y^2}=\frac{1}{4N}\left(\Theta^4-\int_{4\pi}\chi d\Omega\right) \tag{3.41}$$

The right-hand-side of Eq. 3.41 represents the source term in the later LBM formulation of Eq. 3.29. The one-dimensional lattice Boltzmann formulation of the energy equation has been derived by [37], however the two-dimensional derivation for a non-scattering is written in analogy as following:

$$\begin{aligned} g_i\left(\vec{r}+\vec{c}_i\Delta t,t+\Delta t\right)&=g_i\left(\vec{r},t\right)\\ &-\frac{1}{\tau}\left[g_i\left(\vec{r},t\right)-g_i^{eq}\left(\vec{r},t\right)\right]+w_i^m\left(\frac{1}{4N}\left(\widetilde{T}^4-\int_{4\pi}\chi d\Omega\right)\right)\Delta t \end{aligned} \tag{3.42}$$

The source term is given by the difference of the sum of non-dimensional discrete temperatures g_i represented through $\widetilde{T}$, and the spatial integral of the non-dimensional radiative intensity χ, which is calculated from the discrete radiative intensity f_i through numerical integration [22].

3.5.0.2. Method 2

Mishra et al. presented a transient model for solving the radiative-heat exchange in [31]. The set of non-dimensional variables used for the energy equation is given below, for the temperature $\widetilde{T}$, intensity χ, space $\vec{r}$ and time ζ.

$$r_x=x\beta\quad r_y=y\beta\qquad\widetilde{T}=\frac{T}{T_{ref}}\quad\chi=\frac{I}{\sigma T_{ref}^4}\quad\zeta=\alpha\beta^2t \tag{3.43}$$

In the absence of convection and heat generation, for a homogeneous medium, the energy equation is given by

$$\rho c_p \frac{\partial T}{\partial t} = k\nabla^2 T - \nabla \cdot \vec{q}_R \tag{3.44}$$

where $\nabla = (\partial/\partial x + \partial/\partial y)$ *and* $\vec{q}_R$ *is the radiative heat flux.* [31]
The divergence of the radiative heat flux in Eq. 3.44 is dependent on the incident radiation G and the blackbody intensity I_b as given by [4]:

$$\nabla \cdot \vec{q}_R = \kappa_a \left(4\pi I_b - G\right) = \kappa_a \left(4\pi \frac{\sigma T^4}{\pi} - G\right) \tag{3.45}$$

The non-dimensional form of the radiative source term is calculated from the non-dimensional temperatures $\widetilde{T}$ and the incident radiation, which is composed of the radiative intensities' PDFs and their corresponding weights as follows,

$$\nabla^* \cdot \chi = \kappa_a \left(4\widetilde{T} - \frac{\sum\limits_i f_i w_i}{\pi}\right) \tag{3.46}$$

This approach is so far similar to the P-1 radiation model. The non-dimensional form of the energy equation is given as follows,

$$\frac{d\widetilde{T}}{d\zeta} = \frac{d^2\widetilde{T}}{dr_x^2} + \frac{d^2\widetilde{T}}{dr_y^2} - \frac{1}{4N}\nabla^*\chi \tag{3.47}$$

The corresponding LBE can be written as:

$$\begin{aligned} g_i\left(\vec{r} + \vec{c}_i\Delta\xi, \xi + \Delta\xi\right) = g_i\left(\vec{r}, \xi\right) \\ - \frac{\Delta\xi}{\tau}\left[g_i\left(\vec{r}, \xi\right) - g_i^{eq}\left(\vec{r}, \xi\right)\right] - w_i\left(\frac{\Delta\xi}{4N}\right)\nabla \cdot \chi \end{aligned} \tag{3.48}$$

3.6. Hybrid approach

For the sake of completeness hybrid model approaches shall be mentioned as well. In hybrid models, such as given in [40], the discretisation of the radiative transfer directions is computed using the S_N quadrature scheme

(DOM approach), whereupon the rest of the calculation is done using a lattice Boltzmann scheme. Other forms include a conventional numeric approach for the computation of the radiative information, and coupling it in so called multi-physics problems. Exemplary for such a multi-physics coupling of the radiative information with conduction, calculated using a lattice Boltzmann scheme, is [29]. However, using the LBM to solve both the RTE and the energy equation is appealing because of a consistent approach, which shows high potential for parallelisation. Subsequently, Fig. 3.6 illustrates the solution procedure of a hybrid model according to [27].

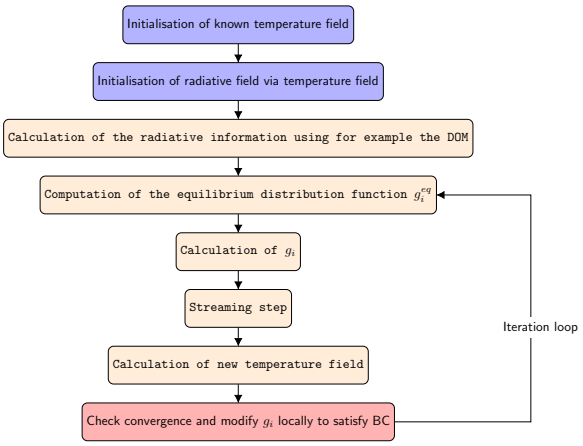

Figure 3.6.: Hybrid model solution procedure

3.7. Lattice arrangements and corresponding weighting factors

The mesh, referred to as lattice in the LBM, is of great importance to every numerical simulation. In dealing with the LBM the lattice arrangements commonly used are squares as well as hexagons in two-dimensional space and cube cells in three-dimensional space [41]. There is a common terminology in the naming of the lattice arrangements known as $DnQm$. The dimension of the problem (one-, two-, three-dimensional) is given by the factor n, whilst the

number of lattice directions is given by the factor m. [21] Subsequently the difference between different lattice arrangements depending on their purpose will be explained.

3.7.1. Commonly used lattice arrangements in fluid dynamics

Figure 3.7 illustrates the possibilities of two-dimensional lattice arrangements, however, the hexagonal D2Q7 lattice arrangement represents rather an exceptional case. An example for the usage of the D2Q7 lattice arrangement is the simulation of shallow water flows as given by Zhou [41]. The commonly used

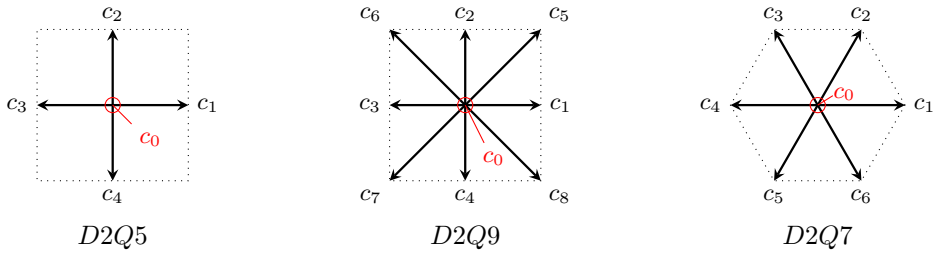

D2Q5 *D2Q9* *D2Q7*

Figure 3.7.: Square and hexagonal two-dimensional lattice arrangements: D2Q5 (left), D2Q9 (middle) and D2Q7 (right)

D2Q9 lattice arrangement has eight velocity vectors starting from the central node. The PDF is transported in each discrete direction with the corresponding velocity. *The weights for directions with identical speeds are equal for reason of symmetry.* [42]
The lattice velocities for the D2Q5 respectively the D2Q9 lattices are given in literature [21] as following:

$$c_0 = (0,0) \qquad c_{1,3} = (\pm 1, 0) \qquad c_{2,4} = (0, \pm 1) \qquad c_{5,6,7,8} = (\pm 1, \pm 1)$$

The corresponding weights for the D2Q5 lattice are:

$$w_i = \begin{cases} \frac{1}{3} & i = 0 \\ \frac{1}{6} & i = 1-4 \end{cases}$$

The corresponding weights for the D2Q9 lattice are:

$$w_i = \begin{cases} \frac{4}{9} & i = 0 \\ \frac{1}{9} & i = 1 - 4 \\ \frac{1}{36} & i = 5 - 8 \end{cases}$$

Depending on their application the lattice arrangements, respectively their velocity sets, have to obey certain requirements. These are generally based on the conservation of mass and momentum and rotational isotropy of the lattice.

3.7.2. Lattice arrangements for the purpose of radiation modelling

Lattice arrangements for radiative transfer simulations are slightly different than those used for fluid dynamics. The difference is based on the fact that there is no stationary node in radiation modelling, as this is physically impossible [22], due to the fast propagation of radiation (speed of light) compared to fluid dynamics. Figure 3.8 shows two representative lattice arrangements for the purpose of radiation modelling. On the left a single speed D2Q4 lattice arrangement is illustrated, whereas to the right a multi speed (MS) lattice arrangement is given. A MS describes in general a lattice arrangement with several different lattice velocities [42]. Apart from those lattice arrangements

D2Q4 *D2Q8*

Figure 3.8.: Two-dimensional lattice arrangements: D2Q4 and D2Q8

mentioned above, there are many others but substantially more complex models,

such as for example the D2Q16 model which is also a MS model. *In these models, the discrete velocities are coupled with the associated lattices, and so such models are also termed as space-filling models.* [43] Unfortunately the terminology is ambiguous, regarding for example the D2Q16 model as can be seen in Figure 3.9.

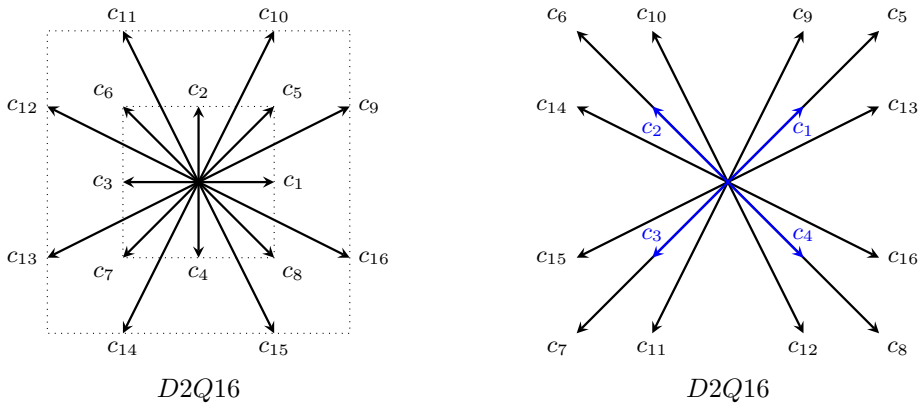

Figure 3.9.: Multi-speed lattice: left D2Q16 by [19], right D2Q16 by [44]

The D2Q16 lattice experimented on was based on the geometry in [19] (left in Fig. 3.9), due to the ideal evenly spaced angular resolution it provides. The following sections deal primarily with the previously illustrated D2Q8 lattice arrangement.

3.7.2.1. Lattice velocities

In order to define the lattice weights one needs to describe the lattice velocities first. These are given below for a D2Q8 lattice.

$$c_i = \begin{cases} c\left(\cos\left(\frac{(i-1)\pi}{2}\right), \sin\left(\frac{(i-1)\pi}{2}\right)\right) & i = 1-4 \\ \sqrt{2}c\left(\cos\left(\frac{(i-5)\pi}{2}+\frac{\pi}{4}\right), \sin\left(\frac{(i-5)\pi}{2}+\frac{\pi}{4}\right)\right) & i = 5-8 \end{cases}$$

The lattice velocities for a D2Q16 lattice are given below [37].

$$c_i = \begin{cases} c\left(\cos\left(\frac{(i-1)\pi}{2}\right), \sin\left(\frac{(i-1)\pi}{2}\right)\right) & i = 1-4 \\ \sqrt{2}c\left(\cos\left(\frac{(i-5)\pi}{2}+\frac{\pi}{4}\right), \sin\left(\frac{(i-5)\pi}{2}+\frac{\pi}{4}\right)\right) & i = 5-8 \\ \sqrt{5}c\left(\cos\left(\frac{(i-9)\pi}{4}+\frac{\pi}{8}\right), \sin\left(\frac{(i-9)\pi}{4}+\frac{\pi}{8}\right)\right) & i = 9-16 \end{cases}$$

3.7.2.2. Lattice weights

Unfortunately, there is no uniform method for the calculation of the lattice weights established in literature. Weighting factors can be interpreted as 'general conditions a velocity set has to obey' [20]. A common rule is that lattice weights are the same if the lattice velocities are the same for their respective direction reasoned by symmetry. In the following, three methods to determine the lattice weights are described:

- **McCulloch et al.** [37] [22]:
  McCulloch and Bindra derived the lattice weights from generalized lattice tensors, a common approach in the application of the LBM. *The weights for each cardinal and diagonal direction lead to isotropic generalized lattice tensors of rank 2 and 4 [...]. This is achieved by conservation of lattice angular moments up to the fourth order over scattering or any other radiation interaction. In case of anisotropic function $w(\mu)$, the odd moments vanish.* [37]
  According to Guo and Shu [43] an isotropic tensor of n-th rank describes a tensor which is invariant to rotations and reflections, thus any arbitrary orthogonal transformation. A theorem describing isotropic tensors up to the fourth rank is given by [42] and [43]:
  - *There are no isotropic tensors of rank 1 (vectors).*
  - *An isotropic tensor of rank 2 is proportional to the 2nd Kronecker delta tensor $\delta_{\alpha\beta}$.*
  - *An isotropic tensor of rank 3 is proportional to $\epsilon_{\alpha\beta\gamma}$*
  - *There are three different (linear independent) tensors of rank 4,*

$$\delta_{\alpha\beta}\delta_{\gamma\eta}, \delta_{\alpha\gamma}\delta_{\beta\eta}, \delta_{\alpha\eta}\delta_{\beta\gamma}$$

which can be combined to the most general form

$$T_{\alpha\beta\gamma\eta} = a\delta_{\alpha\beta}\delta_{\gamma\eta} + b\delta_{\alpha\gamma}\delta_{\beta\eta} + c\delta_{\alpha\eta}\delta_{\beta\gamma}$$

where a, b, c are arbitrary constants.

The odd moments, which are zeroised because of the symmetry condition, are given below. The cartesian components of the lattice velocities c_i are given by $c_{i\alpha}$, $c_{i\beta}$ and $c_{i\gamma}$.

$$\begin{aligned} \sum_i w_i c_{i\alpha} &= 0 \\ \sum_i w_i c_{i\alpha} c_{i\beta} c_{i\gamma} &= 0 \end{aligned} \tag{3.49}$$

The even moments are given subsequently.

$$\begin{aligned} \sum_i w_i &= 1 \\ \sum_i w_i c_{i\alpha} c_{i\beta} &= \delta_{\alpha\beta} \\ \sum_i w_i c_{i\alpha} c_{i\beta} c_{i\gamma} c_{i\eta} &= \delta_{\alpha\beta}\delta_{\gamma\eta} + \delta_{\alpha\gamma}\delta_{\beta\eta} + \delta_{\alpha\eta}\delta_{\beta\gamma} \end{aligned} \tag{3.50}$$

The Kronecker Symbol or Kronecker Delta function is given by [45]

$$\delta_{\alpha\beta} = \begin{cases} 0 & \alpha \neq \beta \\ 1 & \alpha = \beta \end{cases}$$

An evaluation performed by McCulloch and Bindra of the above stated system of equations 3.49 and 3.50 led to the following weighting factors:

$$w_i = \begin{cases} 0.20 & i = 1 - 4 \\ 0.05 & i = 5 - 8 \end{cases}$$

- **Asinari et al.** [19]:
  According to [19] the weight corresponding to the discrete direction i is computed by Eq. 3.51. The angular regions of influence of the PDFs is in general not the same (see Fig. 3.10). Although in the case of the D2Q8 lattice arrangement the angular space (2π) is discretised in eight equally spaced divisions resulting in the same $\Delta\delta_i$ for all.

$$w_i = \left(\frac{1}{4\pi}\right) \int_0^{\pi} \sin\gamma d\gamma \int_{\delta_i - \frac{\Delta\delta_i}{2}}^{\delta_i + \frac{\Delta\delta_i}{2}} d\delta = \frac{\Delta\delta_i}{2\pi} \tag{3.51}$$

Figure 3.10.: Regions of influence (marked grey) for the D2Q8 lattice based on [19] and corresponding energy shells (marked red)

Based upon the interpretation of the left-aligned figure 3.10, where the region of influence for the nodes 5-8 is slightly bigger than that of the remaining nodes (1-4), the nodes 5-8 therefore have a bigger value. Analysis of the area ratios renders the following values for the lattice weights:

$$w_i = \begin{cases} 0.10355 & i = 1-4 \\ 0.14645 & i = 5-8 \end{cases}$$

Regarding the above stated weights in connection with the different energy shells the nodes are located in (see Fig. 3.10 right), the diagonal weighting factors (5-8) can be derived through division by the factor of $\sqrt{2}$, to the same weighting factor as those from nodes one to four, thus,

showing once again the strong geometrical linkage between the weighting factors and the lattice arrangement.
The correlation between the lattice speed and the streaming step is given as $U = \frac{\Delta x}{\Delta t}$ in which is assumed that $\Delta x = \Delta y$. The magnitude of the lattice velocity set can be expressed as $c_i = \varepsilon_i U$, where according to [19] ε_i is a constant depending on the energy shell of the considered velocity. For the D2Q8 under consideration lattice arrangement $\varepsilon_{1-4} = 1$ and $\varepsilon_{5-8} = \sqrt{2}$. The relation between the lattice speed and the lattice velocity is given as follows,

$$c_{1,3} = (\pm 1, 0) \cdot U \ , \ c_{2,4} = (0, \pm 1) \cdot U \ , \ c_{5,6,7,8} = (\pm 1, \pm 1) \cdot U \tag{3.52}$$

- **Yi et al.** [40]:
  Although in [40] no explicit derivation of the D2Q8 lattice arrangement is given, a modified D2Q9 lattice arrangement was used for the modelling of the radiative source term in accordance to the application in CFD (cf. Sec. 3.7.1). Using the D2Q9 as a basis they split the weighting factor of node zero (central node) to equal parts onto the remaining nodes. This results in the following weighting factors:

$$w_i = \begin{cases} 0 & i = 0 \\ \frac{1}{9} + \frac{1}{18} = \frac{1}{6} & i = 1 - 4 \\ \frac{1}{36} + \frac{1}{18} = \frac{1}{12} & i = 5 - 8 \end{cases}$$

3.8. Boundary conditions

3.8.1. Radiative transfer lattice Boltzmann equation

The boundary conditions for the radiative transport lattice Boltzmann equation (RTLBE) are the same for both methods. *Boundary conditions for the radiation equation are calculated based on emissivities of the walls along with the known*

temperatures at the boundary [...] [37]. According to [30] the boundary intensity for a diffuse-gray surface is given by

$$I_{i,wall} = \frac{\varepsilon \sigma T_{wall}^4}{\pi} + \left(\frac{1 - \varepsilon_{wall}}{\pi} \right) q_{wall} \tag{3.53}$$

The first term on the right-hand-side denotes the black body intensity, the second term represents the heat flux at the wall caused by the incident radiation. In case of a black body ($\varepsilon = 1$) Eq. 3.53 is reduced to:

$$I_{i,wall} = \frac{\sigma T_{wall}^4}{\pi} \tag{3.54}$$

The non-dimensional form of Eq. 3.54 can be written as following:

$$\Psi_i = \Theta_{wall}^4 \tag{3.55}$$

In order to implement the boundary condition the below stated boundary conditions were used:

- Dirichlet: in case of a known radiative heat flux at surface
- Neumann: in order to implement zero flux or adiabatic conditions [21]

3.8.1.1. Dirichlet boundary condition

The Dirichlet boundary condition was implemented as a bounce-back boundary as illustrated in figure 3.11. *The working principle of bounce-back boundaries is that populations hitting a rigid wall during propagation are reflected back to where they originally came from.* [20] Thus for the coupled model the temperature values are imposed on the outgoing lattice PDF.

Figure 3.11.: Bounce back boundary condition

3.8.1.2. Neumann boundary condition

The implementation of the Neumann boundary condition assumes a vanishing diffusion flux between the node at the boundary and the node prior to the boundary. Therefore the value of the node prior to boundary was imposed on the boundary node, as illustrated in Fig 3.12. [20]

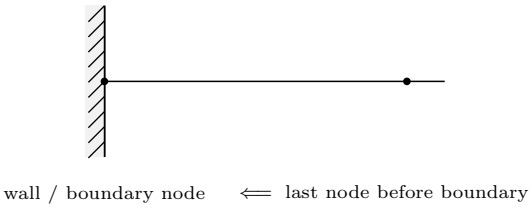

Figure 3.12.: Schematics of the Neumann boundary condition

3.8.1.3. Multi-speed lattice arrangement boundary conditions

The fact that lattice nodes are not restricted anymore to their nearest neighbours demands for an adapted boundary treatment. *Two approaches are currently used to treat multilayer lattices, namely, the external treatment, where layers of nodes are grouped to represent identical boundary conditions, or the internal treatment, where the outer layer of nodes represents the boundary condition and the inner layers belong to the fluid domain.* ***However, there are currently no insightful discussions into which treatment is suitable or more favorable for multispeed lattices.*** [46]
In this connection the affected lattice directions were imposed with the same value on the nodes next to the boundary as on the boundary in order to ensure numerical stability.

3.8.2. Heat transfer lattice Boltzmann equation

Similar to the above described boundary conditions for radiative heat transfer, Dirichlet and Neumann boundary conditions are used to solve the energy equation. The Neumann boundary condition is similar as described in Sec. 3.8.1.2, as for the Dirichlet boundary condition a new scheme is subsequently presented.

3.8.2.1. Dirichlet boundary condition

The implementation of Dirichlet boundaries in style of an Anti-Bounce-Back Scheme based on an approach by Mishra et al. [26] was examined and extended for multiple lattice arrangements (cf. appendix C). The meaning of anti-bounce-back is essentially that the outgoing PDF is represented by a given temperature (T_W) which is combined with the incoming PDF. Assuming the wall has zero velocity the boundary condition can be written as follows,

$$g_i\left(x_b, t+\Delta t\right) = -g_i^*\left(x_b, t\right) + 2 \cdot w_i T_W \tag{3.56}$$

in which g_i represents the outgoing PDF, whilst g_i^* represents the incoming PDF. In case of an anti-bounce-back rule the wall is located between the solid node (x_s) and the boundary node (x_w) as illustrated below. [20]

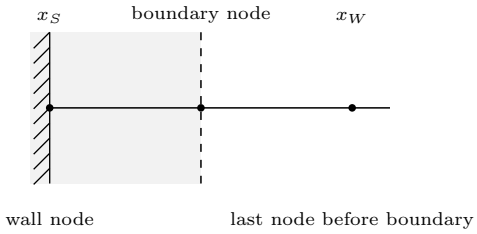

Figure 3.13.: Schematics of the Dirichlet anti-bounce-back boundary condition

3.8.2.2. Corner treatment

Due to the fact that corners in a rectangular geometry are influenced by the two adjacent walls they theoretically have two (sometimes different) boundary conditions. For example the south-east corner of a rectangular geometry

is affected by the south and east wall's temperature. In order to avoid unintentional overwriting of corner nodes, selfsame were set by default to the higher wall temperature, following the approach by [26]. Below in Fig. 3.14 the participating PDFs are illustrated.

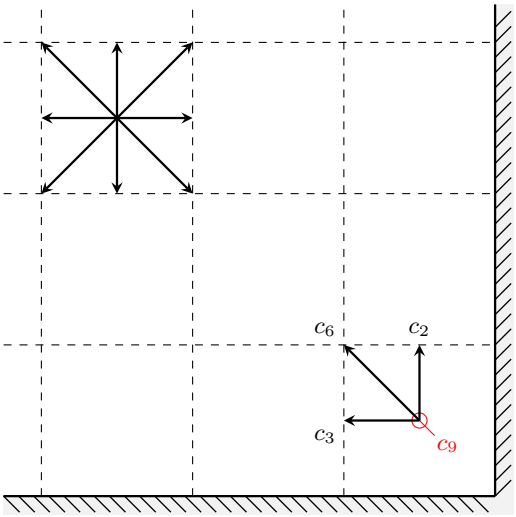

Figure 3.14.: Corner bounce back condition for a concave corner

4. Code validation - two-dimensional test case

The aim of this chapter was to test the LBM based simulation tool for the prediction of radiative heat transfer in industrial furnace applications. The energy equation was solved using the LBM in different media and the results were compared with a reference solution. Furthermore the previously presented 'Method 1' (see Ch. 3.2) was validated for solving the radiative heat transfer in both non-participating and participating media. A mesh study was performed for the radiative transfer in non-participating media with regards to different absorption coefficients and levels of discretisation. The terms 'temperature field' and 'radiative field' denote the temperature respectively the radiation intensity node values of a lattice as a whole.

4.1. Steady state energy equation

In order to calculate the temperature effect on the radiative heat transfer a LBM temperature model was implemented and validated. The energy equation was solved for a steady state heat exchange on a rectangular slab geometry (see Fig. 4.1). Two different cases were studied and validated using an analytical reference and ANSYS Fluent.
In the first case the north and south wall were set to two different temperatures, whilst the east and west wall were exposed to a zero flux condition.
In the second case studied the boundary conditions of the north, east and south wall were set to a value of $T_0 = 300$ K whilst the west wall was defined as source wall with a higher temperature T.
Both cases were subject to analysis with fictional physical property parameters as well as the physical properties of air, which were assumed to be constant.

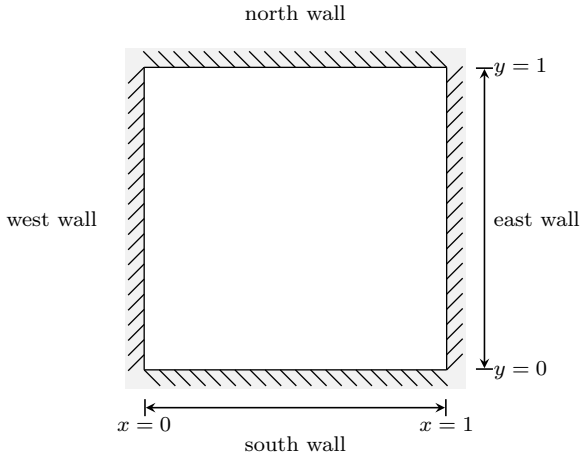

Figure 4.1.: Rectangular slab geometry

The imposed values are listed in the table (Tab. 4.1). An error analysis and validation was performed for both the D2Q5 and the D2Q9 lattice arrangement.

Table 4.1.: Physical properties for validation test case

physical property	fictitious medium	air
density ρ in (kg/m^3)	1	1.225
specific heat capacity Cp in $J/(kgK)$	1	1006.43
thermal conductivity k in $W/(mK)$	1	0.0242

4.1.1. Error analysis

The error of the LBM solution was investigated by Eq. 4.1, where the LBM results were compared to a reference solution.

$$\text{Error}_{LBM} = \frac{||\Psi_{LBM} - \Psi_{\text{reference solution}}||}{||\Psi_{\text{reference solution}}||} \tag{4.1}$$

Furthermore numerical methods are in general prone to the following errors: [48]

- round-off errors: are caused by the numerical precision of the computer used
- iteration errors: describe the difference between a converged solution and the corresponding solution after a large infinite number of iterations
- discretisation errors: describe the difference between the exact solution on a high-resolution mesh compared to the converged solution of a computational reasonable mesh
- model errors: are intrinsic caused by the modelling equations in comparison with reality

4.1.2. Energy transfer lattice Boltzmann equation

The energy equation (Eq. 3.42) presented in the previous chapter (Ch. 3) was validated without the radiative influence term. Thus, the LBE for the energy transport is written as:

$$g_i\left(\vec{r}+\vec{e}_i\Delta t, t+\Delta t\right) = g_i\left(\vec{r},t\right) - \frac{1}{\tau}\left[g_i\left(\vec{r},t\right) - g_i^{eq}\left(\vec{r},t\right)\right] \tag{4.2}$$

The relaxation time parameter τ which has a strong influence on the overall convergence and error was calculated using the approach by [27]. The resulting LBE is given subsequently by Eq. 4.3.

$$g_i\left(\vec{r}+\vec{e}_i\Delta t, t+\Delta t\right) = g_i\left(\vec{r},t\right) - \frac{1}{\tau}\left[g_i\left(\vec{r},t\right) - w_i^m \sum_i g_i\left(\vec{r},t\right)\right] \tag{4.3}$$

4.1.3. Analytical reference

An analytical reference solution was used for the validation of the first case, as for the second the influence of the north-south temperature gradient could not be considered in the one-dimensional analytical solution. The heat equation as given by [20] for a steady state problem ($\partial t = 0$) without source terms ($q = 0$) in a resting medium ($u = 0$) was simplified as following:

$$\cancel{\frac{\partial T}{\partial t}} + \cancel{\nabla\cdot(T\vec{u})} = \alpha\nabla^2 T + \cancel{q} \tag{4.4}$$

Thus, the temperature gradient in any direction (e.g. x-direction) is given as a linear function for constant material properties ($T \neq T(\alpha)$):

$$T(x) = \underbrace{T(x=1)}_{\text{north boundary}} \cdot x + \underbrace{T(x=0)}_{\text{south boundary}} \cdot (1-x) \tag{4.5}$$

4.1.4. ANSYS Fluent

A reference was also provided by ANSYS Fluent for both cases under consideration. For validation the geometry (see Fig. 4.1) was modelled using a uniform mesh with 2025 cells and one with 9801 cells. A mesh independence study showed no significant deviations between the solutions of the two meshes. The energy equation that was solved is given by Eq. 4.6, where the first term on the left hand side describes the temporal change of energy and the second term on selfsame side describes the spatial change. *The first three terms on the right-hand side of equation 4.6 represent energy transfer due to conduction, species diffusion, and viscous dissipation, respectively. S_h includes the heat of chemical reaction, and any other volumetric heat sources [...]* . [9]

$$\frac{\partial}{\partial t}(\rho E) + \nabla \cdot (\vec{u}(\rho E + p)) = \nabla \cdot \left(k_{eff} \nabla T - \sum_j h_j \vec{J}_j + \left(\overline{\overline{\tau}}_{eff} \cdot \vec{v} \right) \right) + S_h \tag{4.6}$$

Simplification of the above equation for the problem present leads to the same formulation as described in the previous analytical reference section:

$$0 = \nabla^2 T. \tag{4.7}$$

4.1.5. Results - Case 1

The error between the LBE formulation and the analytical solution is primarily dependent on the relaxation time value τ. In comparison the influence of the overall convergence tolerance on the PDFs is rather negligible. The calculated error values were computed from the centreline temperature data in reference to their respective analytical reference solution. A separate illustration of the ANSYS Fluent temperature field plots was forgone due to the high similarity

to the energy transport lattice Boltzmann equation (ETLBE) results. The temperature boundary condition was implemented using an anti-bounce-back scheme. For the implementation of the zero flux condition a Neumann boundary condition was used as described in the previous chapter (Ch. 3.8).

4.1.5.1. Fictitious medium

The influence of five different time step parameters listed in table 4.2 and table 4.3 was analysed. The corresponding marching step was defined in all simulations as $\Delta x = \frac{1}{N_x - 1}$. Variant A represents a common approach [20], thus it is usually used in context with a marching step of the same size - the results showed to be poor as expected . Variant B was chosen according to [22], variants D and E present the doubled and halved value of selfsame in order to determine the overall influence. Variant C was found empirically to resolve the problem with good accuracy.

Table 4.2.: Time step variations for an adiabatic validation test case D2Q5 with the hot wall at 1300 K in exchange with the cold wall at 300 K

variant	time step	simulation time in s (mesh 100×100)	max. Error in %
A	1	1062	1.772
B	$1/(N_x - 1)$	28.0	0.0667
C	$1/(N_x)$	28.6	0.0682
D	$2/(N_x - 1)$	8.3	0.0103
E	$1/[2(N_x - 1)]$	187.4	0.6539

Table 4.3.: Time step variations for an adiabatic validation test case D2Q9 with the hot wall at 1300 K in exchange with the cold wall at 300 K

variant	time step	simulation time in s (mesh 100×100)	max. Error in %
A	1	1841	8.6733
B	$1/(N_x - 1)$	48.5	0.0667
C	$1/(N_x)$	49.7	0.0683
D	$2/(N_x - 1)$	14.8	0.1612
E	$1/[2(N_x - 1)]$	319.8	0.6524

The different variations of time steps had great impact on the overall simulation runtime and quality of the results. Analysis showed that by increasing the relaxation time the simulation runtime was drastically reduced. In addition

the error decreased slightly. Apart from the increased simulation runtime and number of iterations for the D2Q9, there was no noticeable difference between the two lattice arrangements under investigation. The impact of a higher mesh discretisation on the solution is illustrated in table 4.4 for the D2Q9 lattice arrangement.

Table 4.4.: Time step variations for an adiabatic validation test case D2Q9 with the hot wall at 1300 K in exchange with the cold wall at 300 K

variant	time step	simulation time in s (mesh 200×200)	max. Error in %
A	1	14800	9.0878
B	$1/(N_x - 1)$	340	0.2682
C	$1/(N_x)$	345	0.2714
D	$2/(N_x - 1)$	100	0.068
E	$1/[2(N_x - 1)]$	2014	2.562

All other simulation parameters, such as the physical properties of the medium, were fixed for the validation. The relaxation time term is grid dependent, thus, was the only parameter that was changed during the simulations. The grid-dependency of the relaxation time led to a grid dependent error of the solution, which increased exponentially with higher levels of discretisation. However it was found out, through analysis of different hot wall temperature boundaries up to a temperature of 2300 K, that with increasing temperature gradients the increase of the error is lower for the time step variants B - E. Table 4.5 shows the results of the different time steps for a mesh of the size 200×200, where the hot wall's boundary was set to a temperature of 2300 K and the cold wall's boundary was set to a temperature of 300 K.

Table 4.5.: Time step variations for an adiabatic validation test case D2Q9 with the hot wall at 2300 K in exchange with the cold wall at 300 K

variant	time step	simulation time in s (mesh 200×200)	max. Error in %
A	1	9163	10.0223
B	$1/(N_x - 1)$	247	0.2312
C	$1/(N_x)$	249	0.2339
D	$2/(N_x - 1)$	61	0.0552
E	$1/[2(N_x - 1)]$	1491	2.2083

Figure 4.2 (left) shows the temperature profile for the investigated case for given wall temperatures of 1300 K and 300 K calculated using the time step 'Variant B'. The corresponding errors calculated from the analytical reference solution for the time step variants B, C and D are displayed in Fig. 4.2 (right).

Due to the different magnitude of the error of variant A and E, the display of selfsame was forgone. The error of the variants B and C show, as expected, only small deviations among one another. For the time step variant D a significant lower error is visible, as well as a shift of the peak towards the cold temperature boundary.

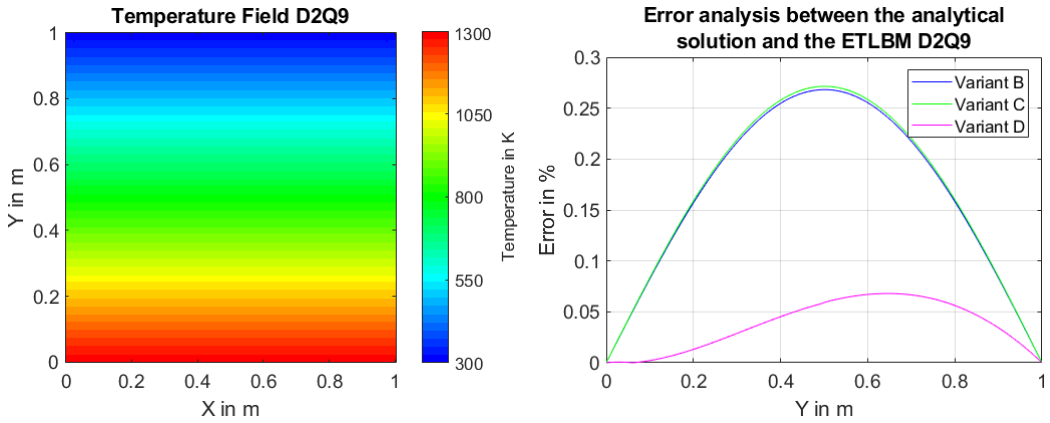

Figure 4.2.: Temperature field of the solved ETLBE (D2Q9 - time step variant B) for mesh size of 200 × 200 with a comparison of different time steps in analysis of the analytical error

4.1.5.2. Medium air

The change in media properties had great impact on the solution for the different time step variants under consideration. Due to the influence of the media's physical properties, which are represented in the relaxation term via the thermal diffusivity α, the formerly labelled as 'variant A' time step of $\Delta t = 1$ was the only variant, of those analysed, that led to results. Figure 4.3 shows the temperature field and the corresponding error calculated from the ANSYS Fluent reference solution, using the same mesh size and a D2Q9 lattice arrangement for the ETLBE solution.

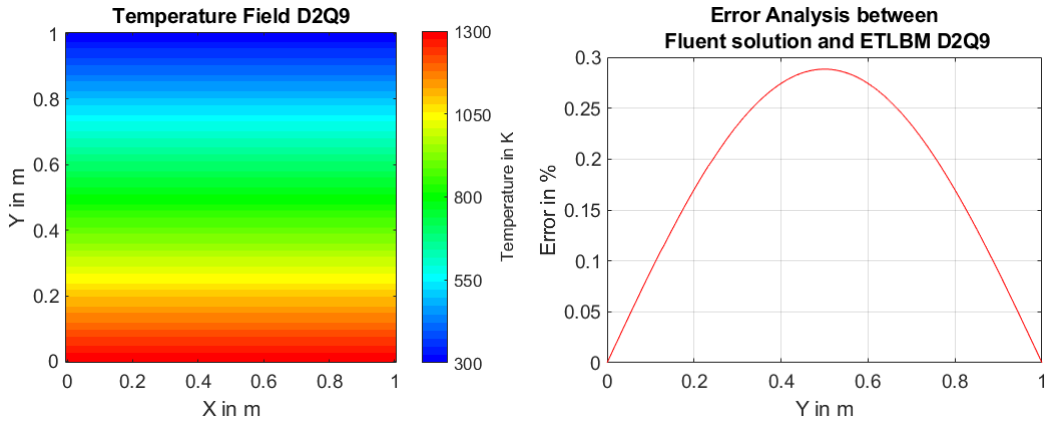

Figure 4.3.: Comparisons of the ETLBE (D2Q9) with ANSYS Fluent and error analysis using the same mesh size of 100×100 for a hot wall temperature of 1300 K (medium air)

There appears to be no grid dependency of results as further analysis using a 200×200 lattices has shown no significant change in error between the LBM and the solution computed with ANSYS Fluent.

4.1.6. Results - Case 2

The results showed in both media overall good comparison. A separate illustration of the ANSYS Fluent temperature field plots was forgone due to the high similarity to the ETLBE results. The second case was focused on

the D2Q9 lattice arrangement in view of the coupling of the ETLBE with the RTLBE. The temperature boundary condition was implemented using an anti-bounce-back scheme as described in the previous chapter (Ch. 3.8).

4.1.6.1. Fictitious medium

Figure 4.4 shows the comparison of the ETLBE solution and the ANSYS Fluent solution, in which the high temperature wall was set to 1300 K whilst the remaining walls were set to a temperature of 300 K. The time step was set to $\Delta t = 1/(N_x - 1)$ as previously introduced as 'Variant B'.

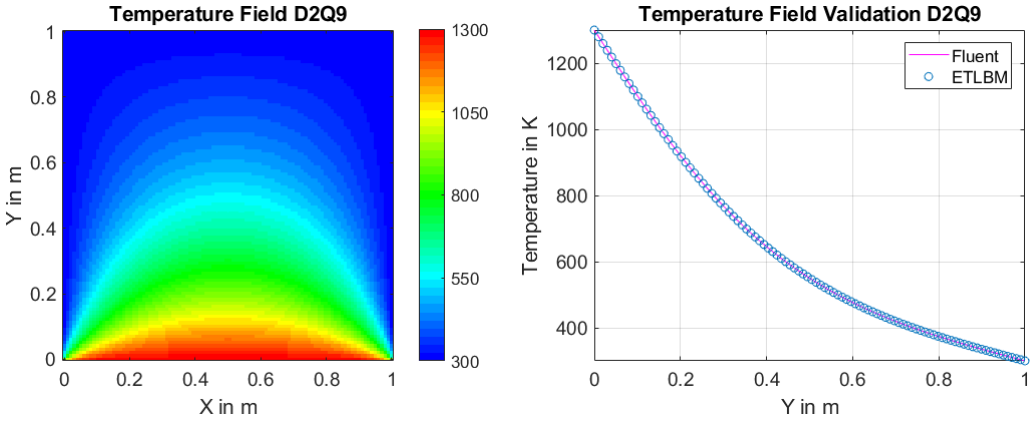

Figure 4.4.: Comparisons of the ETLBE (D2Q9) with ANSYS Fluent using a mesh size of 100×100; the hot wall temperature was set to 1300 K whilst the remaining walls were set to 300 K

The results for the different time steps, for the investigated case, are given in table 4.6. The results show strong deviations between the different time steps. A comparison with the results of the first case investigated (see Tab. 4.3) reveals a reduction of the simulation time. Furthermore the error of the time step variants B, C and E is reduced.

Table 4.6.: Time step variations for an adiabatic validation test case D2Q9 with the hot wall at 1300 K in exchange with the cold wall at 300 K

variant	time step	simulation time in s (mesh 100×100)	max. Error in %
A	1	681	30.7714
B	$1/(N_x - 1)$	8.4	0.0341
C	$1/(N_x)$	8.4	0.0341
D	$2/(N_x - 1)$	3.4	2.7286
E	$1/[2(N_x - 1)]$	48.3684	0.2236

The error for this specific case was calculated at the centre line from the north to the south wall from the ANSYS Fluent reference solution, and is given in Fig. 4.5. The ETLBE, with the time step referred to as 'variant B', shows good comparison over the whole range of temperatures under consideration with the ANSYS Fluent results and the analytical reference solution.

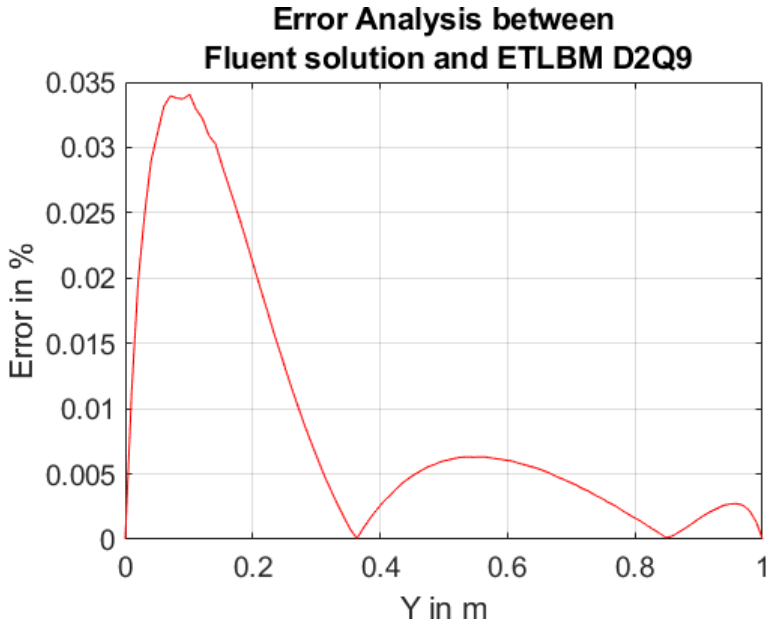

Figure 4.5.: Error analysis between the ANSYS Fluent solution and ETLBM (D2Q9) using a mesh size of 100×100; one wall temperature was set to 1300 K whilst the remaining walls were set to 300 K

4.1.6.2. Medium Air

Figure 4.6 shows the comparison of the ETLBE solution and the ANSYS Fluent solution, in which the high temperature wall was set to 1300 K whilst the remaining walls were set to a temperature of 300 K. The time step was set to $\Delta t = 1$ as previously introduced as 'Variant A'.

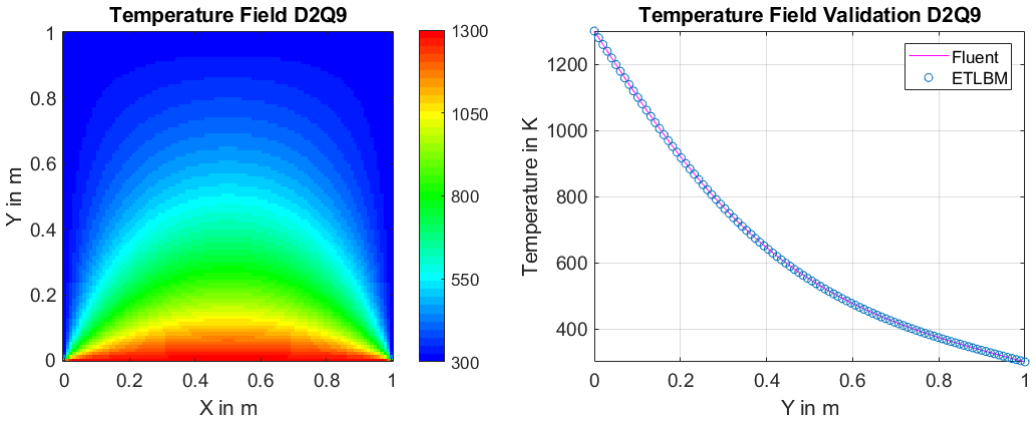

Figure 4.6.: Comparisons of the ETLBE (D2Q9) with ANSYS Fluent using a mesh size of 100×100; the hot wall temperature was set to 1300 K whilst the remaining walls were set to 300 K (medium air)

The error for this specific case was calculated at the centre line from the north to the south wall from the ANSYS Fluent reference solution, and is given in figure 4.7.

The ETLBE shows good comparison over the whole range of temperatures under consideration with the ANSYS Fluent results and the analytical reference solution. However, the detailed error analysis of the centreline data (see Fig. 4.7) reveals in comparison to the centreline error of the fictitious medium (see Fig. 4.5) a higher deviation. This is very likely caused by the different relaxation times τ, which are composed of the media's physical properties.

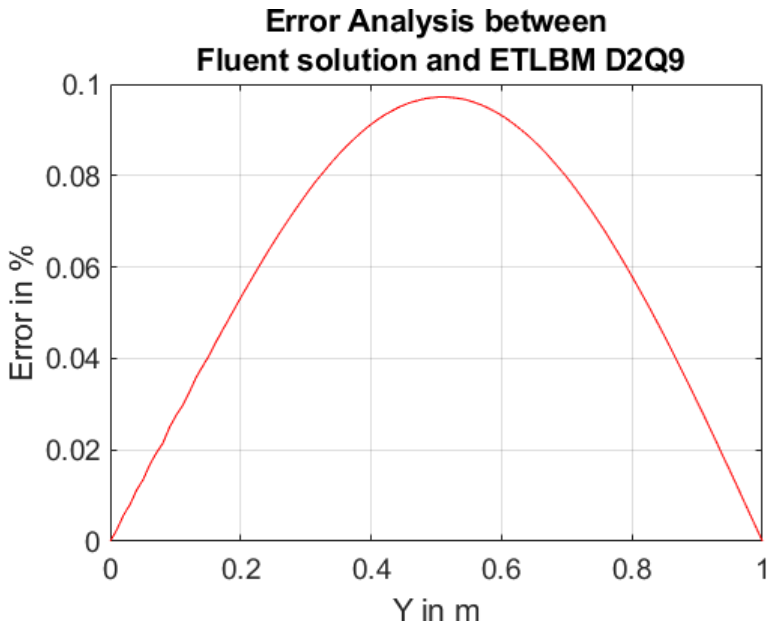

Figure 4.7.: Error analysis between the ANSYS Fluent solution and ETLBM (D2Q9) using a mesh size of 100×100; one wall temperature was set to 1300 K whilst the remaining walls were set to 300 K

4.2. Radiation

The two methods described in the previous chapter (Ch. 3) were investigated for the usage of the calculation of the RTE. Natural gas, which is commonly used as fuel in industrial high temperature applications, allowed for the scattering term to be neglected. This is reasoned by the low particle concentration in the flue gas, hence scattering effects have only a minor influence on the results [47]. Therefore, Eq. 1.5 can be written as:

$$\frac{dI}{ds} = \kappa I_b - \kappa I \tag{4.8}$$

According to [4] the source function equals the local blackbody intensity for radiative equilibrium with a nonzero absorption coefficient. Thus Eq. 4.8 is written as:

$$\frac{dI}{ds} = \kappa \frac{\sigma T^4}{\pi} - \kappa I \tag{4.9}$$

4.2.1. Participating medium without consideration of the temperature influence

The case used for the validation of the radiative heat exchange is illustrated in Fig. 4.8. At the source wall (west wall) a radiative flux was given, whilst at the recipient wall the incoming radiative flux was analysed. A rectangular geometry of the size 1×1 m (see Fig. 4.1) was used for this process, at which only the discretisation in the x-direction (primary direction of interest) was varied. The discretisation in the y-direction was set to a value of 2. The north, south and east walls were subjected to a Neumann boundary condition. A D2Q8 lattice arrangement, with the weighting factors introduced by McCulloch in [22], was used in order to calculate the radiative information.

4.2.1.1. Simplified radiative transfer lattice Boltzmann equation

Method 1 forms the basis for further calculations, as it is identical with Method 2 in this specific case, where the black body intensity is neglected. The one-dimensional approximation of the RTE (Eq. 4.9) is given below.

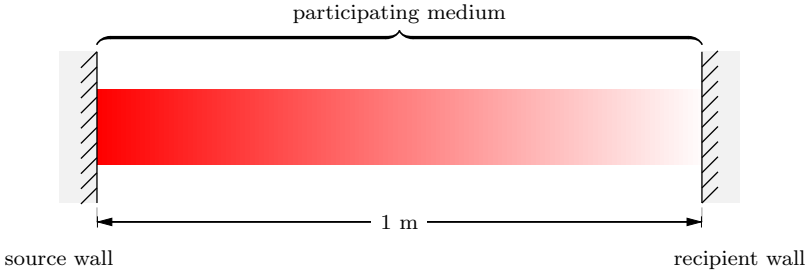

Figure 4.8.: Schematical setup for the analytical solution calculation

One-dimensional approximation
The left-hand-side represents the spatial change in radiative intensity caused by the absorption term on the right-hand-side.

$$\mu \frac{dI}{dx} = -\kappa_a I \tag{4.10}$$

The non-dimensional form is missing the absorptive information, as the scaling variable W described in the previous chapter (Ch. 3) eliminates the absorption coefficient. Thus a different set of non-dimensional variables was used to preserve the absorptive information in which the scaling factor W was set to a value of one.

$$\mu \frac{d\chi}{dr_x} = -\kappa_a \chi \tag{4.11}$$

The equivalent LBE is:

$$f_i\left(r_x + c_{i,r_x}\Delta t, t + \Delta t\right) = f_i\left(r_x, t\right) - \Delta t \kappa_a f_i \tag{4.12}$$

Two-dimensional approximation
The two-dimensional equation is given below,

$$f_i\left(\vec{r} + \vec{c}_i\Delta t, t + \Delta t\right) = f_i\left(\vec{r}, t\right) - \Delta t \kappa_a f_i\left(\vec{r}, t\right) \tag{4.13}$$

where the spatial directions are given by $\vec{r} = (r_x, r_y)$.

4.2.1.2. Analytical reference

In order to validate the calculated LBM solution a simplified RTE was solved analytically. For the previously presented LBM procedure scattering was neglected as well as the intensity augmented by local emission. This case is referred to in literature as 'absolute absorption' [3].

$$(dI)_{abs} = -\kappa_a I ds \tag{4.14}$$

$$I(s) = I(0) \exp\left(-\int_0^s \kappa_a ds\right) = I(0)\, e^{-\tau} \tag{4.15}$$

The optical thickness τ describes the transmissivity of a homogeneous isothermal gas layer. The analytical solution for the investigated case is given subsequently in Fig. 4.9 for an absorption coefficient of value 1 m^{-1} and a given radiative flux of 1 $W/(m^2 K)$.

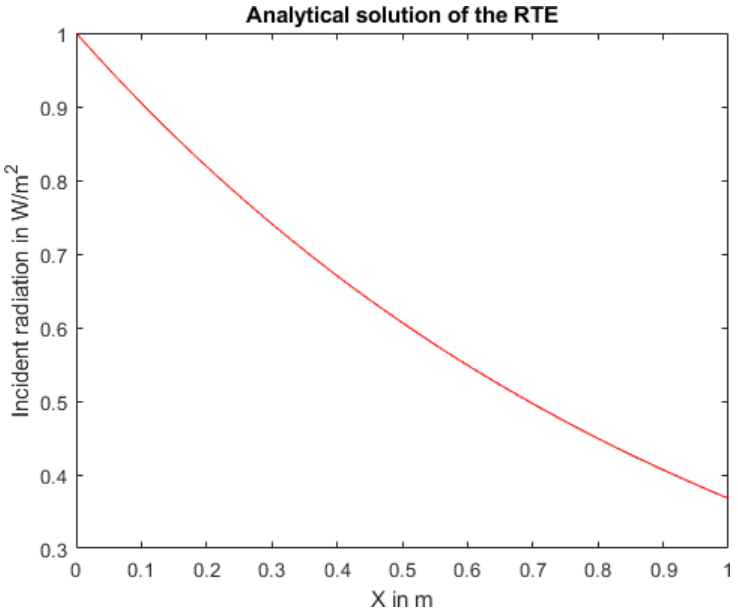

Figure 4.9.: Analytical solution of the simplified radiative transfer equation $\kappa_a = 1\ m^{-1}$

4.2.1.3. Error analysis and grid convergence study

The LBM solution was compared to the analytical solution, and the resulting error was calculated using Eq. 4.1. The absorption coefficient value was varied from 0.1 m^{-1} to 5.0 m^{-1}. The LBM solution proved to be very accurate for high levels of discretisation. However, with increasing absorption coefficients the error increased as well, as can be seen in Fig. 4.10 in which a constant discretisation of 15000 nodes was applied.

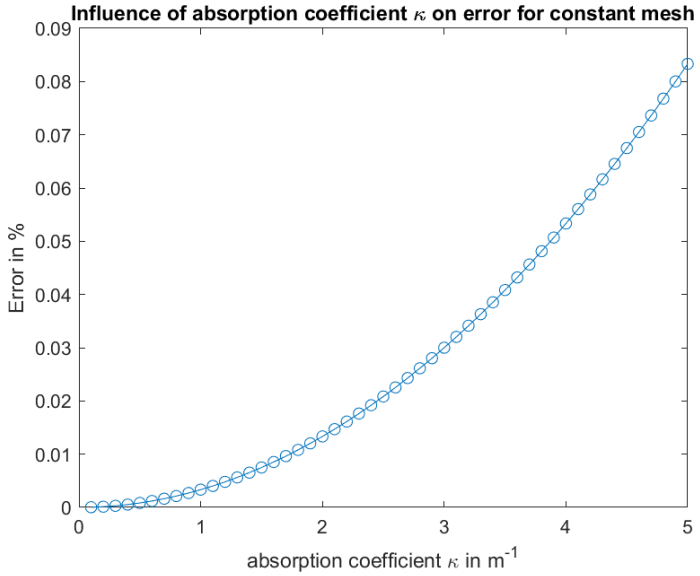

Figure 4.10.: Influence of absorption coefficient on error for constant number of nodes $N_x = 15000$

The subsequent figure (Fig. 4.11) shows the influence of different levels of discretisation on the calculated error for a constant absorption coefficient value of 1 m^{-1}. The curve characteristics of different absorption coefficients were shown to be similar. However, as previously shown in Fig. 4.10, higher levels of the absorption coefficient lead to an increase of the error especially for a low number of lattice nodes.

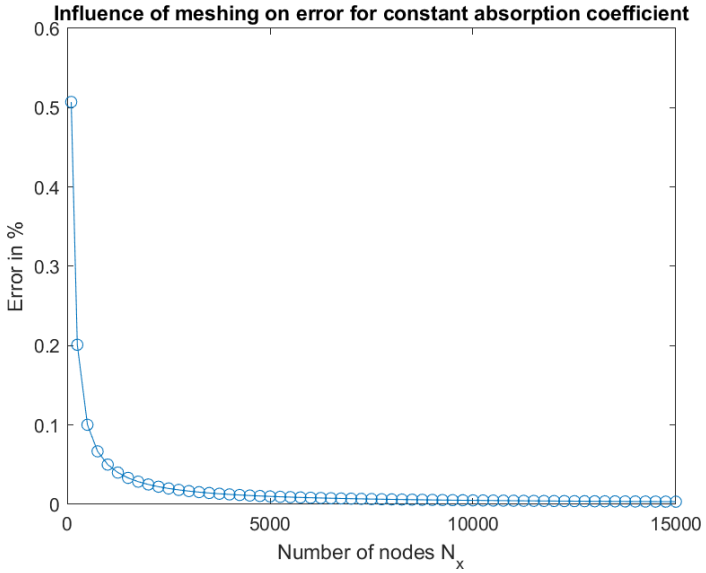

Figure 4.11.: Influence of mesh discretisation on error for constant absorption coefficient $\kappa = 1\ m^{-1}$

4.2.2. Participating medium with consideration of the temperature influence

The consideration of the black body intensity on radiative heat transfer requires the coupling of the RTLBE and the ETLBE. Due to the high adaptability of the first method described, only 'Method 1' was further analysed.
The sample problem consisted of the same rectangular slab geometry as illustrated in Fig. 4.1 in the previous section (Sec. 4.1). The temperature influence was investigated at five different levels, ranging from 400 K to 2300 K with a respective reference temperature set at 300 K. Three different values for the absorption coefficient κ_a (0.5 m^{-1}, 0.75 m^{-1}, 1 m^{-1}) were investigated for the two-way coupled model. In order to examine the influence of different physical properties two cases were investigated. The first using fictitious physical properties and the second by assuming constant physical properties of the medium air. The imposed values are listed in the table (Tab. 4.1) below.
In all of the subsequently investigated cases, the Stark number N did not exceed a value of 0.1, thus, proving that radiation was the dominating heat transfer mechanism.

4.2.2.1. Radiative transfer lattice Boltzmann equation - Method 1

In order to estimate the temperature influence, the RTE has to be coupled with the energy equation. The basis for the RTE form once again Eq. 3.15 and Eq. 3.41 for the energy equation. The problem was solved using a single speed lattice for both the RTLBE (D2Q8) and the ETLBE (D2Q9). Additionally a MS lattice arrangement (D2Q16) was investigated to predict the radiative information. In order to distinguish between the lattice weights of the different lattice arrangements used, the lattice weights of the ETLBE are hereinafter denoted as w_i^m.

RTLBE two-dimensional approximation

$$f_i\left(\vec{r}+\vec{c}_i\Delta t, t+\Delta t\right) = f_i\left(\vec{r},t\right) - \Delta t\left[w_i\widetilde{T}^4 + f_i\left(\vec{r},t\right)\right] \tag{4.16}$$

Energy Equation

$$g_i\left(\vec{r}+\vec{c}_i\Delta t, t+\Delta t\right) = g_i\left(\vec{r},t\right) - \frac{1}{\tau}\left(g_i - g_i^{eq}\right) + w_i^m\left(\frac{1}{4N}\left(\widetilde{T}^4 - \int_{\Omega=4\pi}\chi d\Omega\right)\right) \tag{4.17}$$

The radiation integral has been approximate by the local sum of all radiative PDFs.

$$g_i\left(\vec{r}+\vec{c}_i\Delta t, t+\Delta t\right) = g_i\left(\vec{r},t\right) - \frac{1}{\tau}\left(g_i - g_i^{eq}\right) + w_i^m\left(\frac{1}{4N}\left(\widetilde{T}^4 - \frac{1}{4}\sum_i f_i\right)\right) \tag{4.18}$$

4.2.2.2. Coupling Methods

The coupling of the radiative transfer LBE and the energy LBE leads to the solving procedure oriented on the coupling procedure of a hybrid model (see Sec. 3.6) developed by Mishra et al. [26] (see Fig. 4.12).

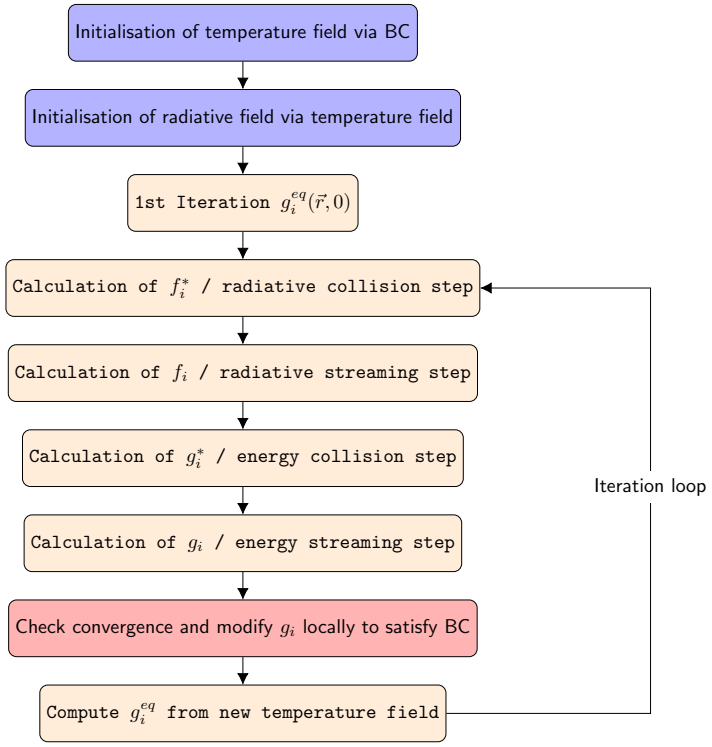

Figure 4.12.: Coupling procedure

The coupling procedure has been further adapted neglecting the influence of radiation on the energy equation respectively the temperature field, thus representing a one-way coupling model. In figure 4.13 the first loop was experimentally replaced by a given temperature field to examine the influence of selfsame on the radiative field calculated using the RTLBE.

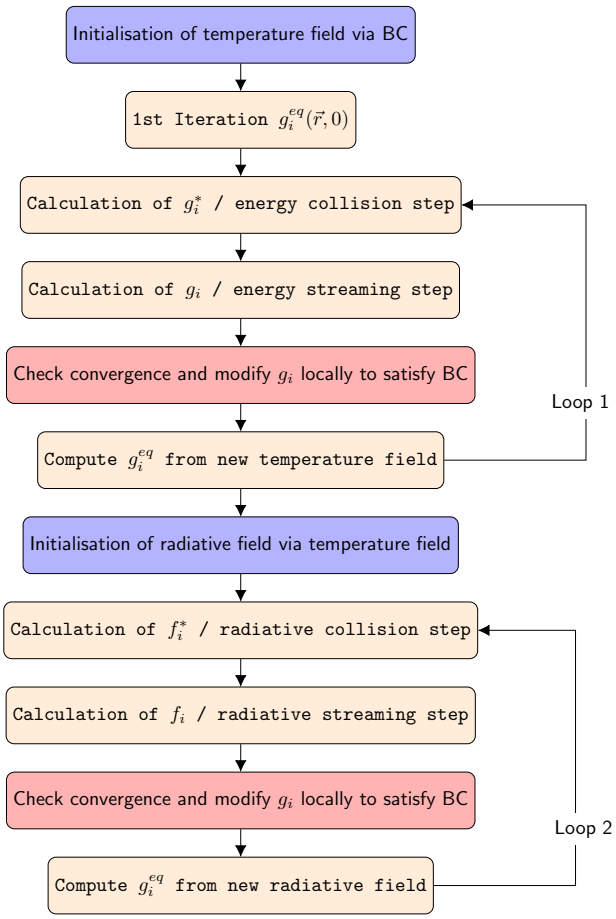

Figure 4.13.: Adapted one-way coupling procedure

The various coupling models investigated are listed below:

- two-way coupled model: RTLBE and ETLBE are solved simultaneously
- one-way coupled model:
  - Variant 1: RTLBE and ETLBE are solved simultaneously, but the radiative source term in the ETLBE is not solved
  - Variant 2: a temperature field is given a priori and the RTLBE is solved

4.2.2.3. Reference solution: P-1 Model - ANSYS Fluent [9]

The P1 model allows modelling of gray radiation and is the simplest case of the P_N model. The radiative flux q_r is calculated using Eq. 4.19, where κ_a is the absorption coefficient, σ_S the scattering coefficient, C the linear-anisotropic phase function coefficient and G the incident radiation.

$$q_r = -\frac{1}{3\left(\kappa_a + \sigma_S\right) - C\sigma_S}\nabla G \tag{4.19}$$

Assuming a non scattering medium Eq. 4.19 can be further simplified:

$$q_r = -\frac{1}{3\kappa_a}\nabla G \tag{4.20}$$

The transport equation for the incident radiation G without additional sources is given in Eq. 4.21 where σ represents the Boltzmann constant and n the refractive index of the medium.

$$-\nabla q_r - \kappa_a G + 4\kappa_a n^2 \sigma T^4 = 0 \tag{4.21}$$

The combination of Eq. 4.20 and Eq. 4.21 yields:

$$\frac{1}{3\kappa_a}\nabla^2 G - \kappa_a G + 4\kappa_a n^2 \sigma T^4 = 0 \tag{4.22}$$

As the analysed problem considered only a homogeneous phase, the refractive index n was set to a value of one.

$$\frac{1}{3\kappa_a}\nabla^2 G - \kappa_a G + 4\kappa_a \sigma T^4 = 0 \tag{4.23}$$

4.2.2.4. Reference solution: Discrete Ordinates (DO) Model - ANSYS Fluent [9]

The discrete ordinates (DO) radiation model solves the radiative transfer equation (RTE) for a finite number of discrete solid angles, each associated with a vector direction $\vec{s}$ fixed in the global Cartesian system (x, y, z).[9]. The RTE stated in Eq. 4.24 is considered as a field equation in the direction $\vec{s}$, where $I(\vec{r}, \vec{s})$ is the total intensity.

$$\nabla \cdot (I(\vec{r}, \vec{s})\,\vec{s}) + (\kappa_a + \sigma_S)\, I(\vec{r}, \vec{s}) = \kappa_a n^2 \frac{\sigma T^4}{\pi} + \frac{\sigma_S}{4\pi} \int_0^{4\pi} I(\vec{r}, \vec{s})\, \Phi(\vec{s} \cdot \vec{s}')\, d\Omega \quad (4.24)$$

Assuming a non scattering medium Eq. 4.24 can be further simplified:

$$\nabla \cdot (I(\vec{r}, \vec{s})\,\vec{s}) + \kappa_a I(\vec{r}, \vec{s}) = \kappa_a n^2 \frac{\sigma T^4}{\pi} \quad (4.25)$$

The DOM solution was calculated using an angular discretisation of five Θ and Φ divisions each.

4.2.2.5. One-way coupled model

In order to examine the effects of a given temperature field on the radiative field a 'one-way' coupled model was tested (see Fig. 4.13). As the physical properties of the medium are only present in the formulation of the ETLBE, a further sub-division into different media can be omitted. The one-way coupled model was investigated further given an equidistant temperature field. Furthermore, temperature solutions calculated using the DOM coupled with the energy equation in Fluent, were patched in the LBM code and the radiative information was calculated. The temperatures under consideration ranged from 300 K up to 2300 K. In order to avoid a change of the given temperature field in Fluent, through the coupling of RTE and heat equation, the thermal conductivity was set to an artificially high level.

The results of the model with given temperature values proved to be in coherence with those calculated using the DOM, due to the relatively small influence of the temperature related source term in the RTE. In this context the temperature influence in the RTE, given by the term $\widetilde{T}$, was set to a value of one, as proposed by [37], leading to similar results. As for the influence of the radiative field on the temperature a significant influence was recognisable, especially concerning the numerical stability of the model at hand. Subsequently, in Fig. 4.14 the results for the one-way coupled model are given. The radiative information was calculated using a D2Q4 lattice arrangement. The temperature was pre-set by a linear temperature gradient ranging from 800 K to 300 K.

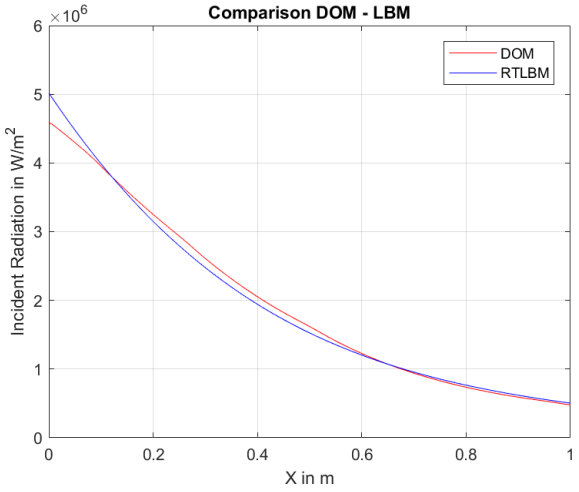

Figure 4.14.: Comparison of DOM and LBM (D2Q4) results for given linear temperature gradient from 800 K to 300 K and a mesh size of 200 × 200 in both solution methods

4.2.2.6. Two-way coupled model

The focus of the error analysis was set on the two-way coupled model, as it is of capital importance for the further intended applications. Subsequently the results of the analysis are given for a fictitious medium, followed by the results of the medium air.

4.2.2.6.1. Fictitious medium

The ETLBE was solved using a time step of $\Delta t = 1/(N_x - 1)$. The results showed overall good comparison for the D2Q8-D2Q9 model. The subsequent figures (Fig. 4.15, 4.16, 4.17) illustrate the influence of different absorption coefficient values for the same boundary temperature of 1800 K with a respective reference temperature on the opposite wall of 300 K. With increasing absorption coefficient values the similarity of the LBM solution to the P1 solution is visible. Furthermore a deviation is visible at the temperature boundary, as the prescribed temperature boundary value was not reached in any of the LBM simulations. However, with increasing absorption coefficient selfsame deviation was reduced. The Stark number, being dependent on the absorption coefficient κ_a, showed in all three cases that the heat transfer was dominated by radiation. The results for the same case, solved using the MS lattice arrangement D2Q16 for the RTLBE, are given in figures 4.18, 4.19 and 4.20. The higher angular resolution did not lead to any improvement of the results. However, as mentioned in the previous chapter (see Sec. 3.8.1.3), it is suspected that the implemented boundary condition is the source of the altered results. The results show, opposite as for the D2Q8 lattice arrangement, good comparison for decreasing values of the absorption coefficient κ_a.
The visible boundary error in the temperature solution was boosted by the low resolution mesh (100×100) used, higher discretisation led to a considerable improvement of the results, as previous findings have shown (see Fig. 4.11).

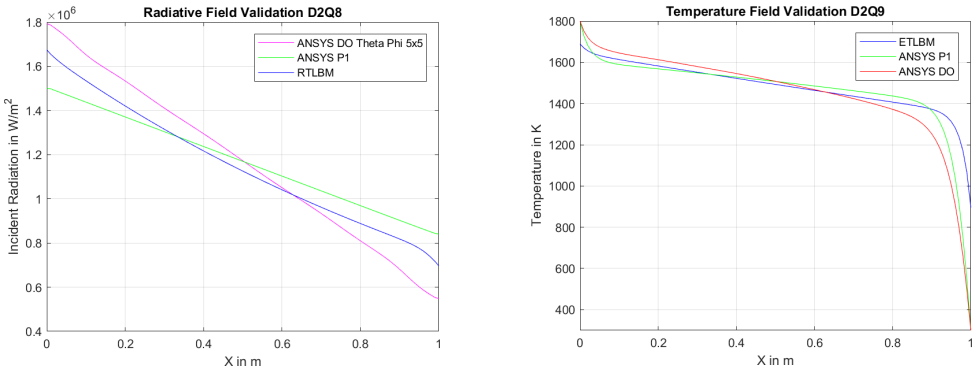

Figure 4.15.: Radiative (D2Q8) and temperature (D2Q9) field validation: $\kappa_a = 0.5\ m^{-1}$

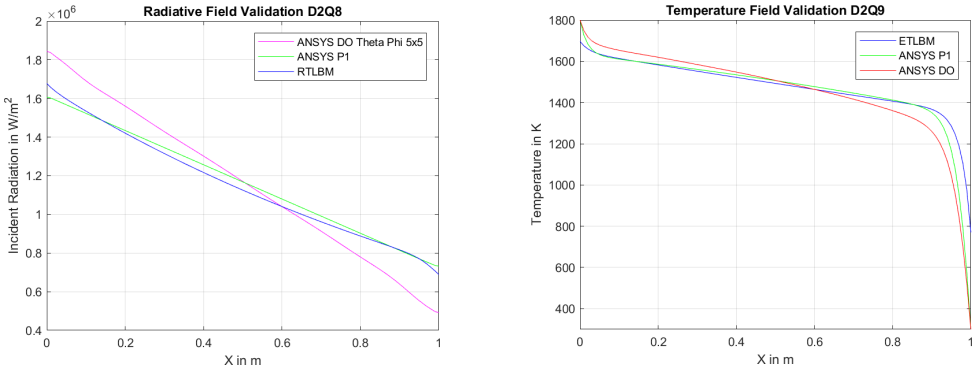

Figure 4.16.: Radiative (D2Q8) and temperature (D2Q9) field validation: $\kappa_a = 0.75\ m^{-1}$

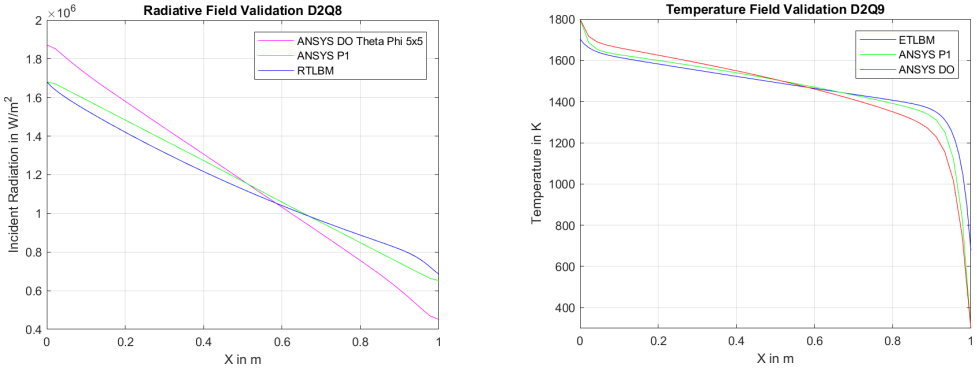

Figure 4.17.: Radiative (D2Q8) and temperature (D2Q9) field validation: $\kappa_a = 1\ m^{-1}$

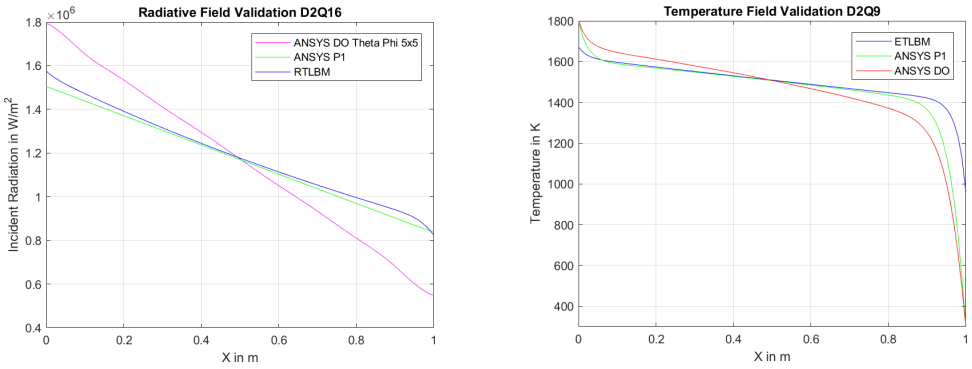

Figure 4.18.: Radiative (D2Q16) and temperature (D2Q9) field validation: $\kappa_a = 0.5\ m^{-1}$

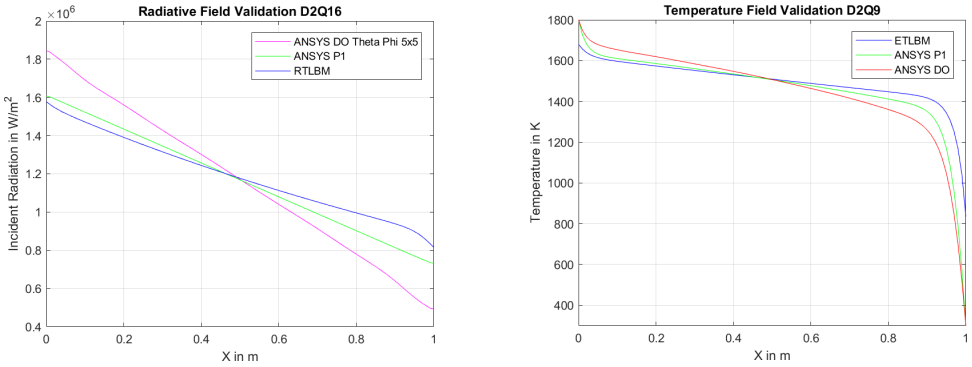

Figure 4.19.: Radiative (D2Q16) and temperature (D2Q9) field validation: $\kappa_a = 0.75\ m^{-1}$

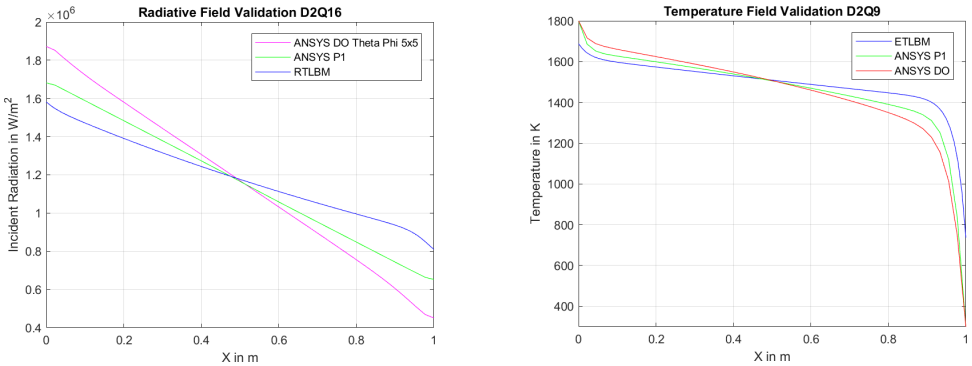

Figure 4.20.: Radiative (D2Q16) and temperature (D2Q9) field validation: $\kappa_a = 1\ m^{-1}$

4.2.2.6.2. Medium air

In order to explore the effects of physical properties on the model, the medium air was chosen as a start. The results of the RTLBE are in correspondence with those calculated using the DOM and P1 model. With an increasing number of lattice nodes the error on the boundaries of the ETLBE increases in dependence of the temperature gradient. Subsequently, a sample case for a wall temperature of 800 K, with a respective reference temperature of 300 K, is illustrated using different values of absorption coefficients and the D2Q8 lattice arrangement on a mesh consisting of 100×100 nodes (see Fig. 4.21, 4.22, 4.23). The results of the radiative field reveal a strong similarity to the P1 model with increasing levels of the absorption coefficient. However, the boundary condition of the temperature field does not match the given value. The same case was further investigated using a D2Q16 lattice arrangement, as illustrated in the figures 4.24, 4.25 and 4.26. The results of the radiative field show, in analogy to those calculated for the fictitious medium, good accordance with the P1 model for low values of the absorption coefficient κ_a. However, a strong deviation is visible in the temperature field results, especially in the vicinity of the lower temperature boundary.

The strong gradient in the temperature profile near the boundary is reflected in the solutions of the radiative field in form of a slight peak. The source of deviation in the temperature field remains uncertain, various approaches to adapt the algorithm have been unsuccessful. It is assumed that this decrease in numerical stability, caused by the decrease of the spatial grid step Δx, is related to the time step Δt which remains mesh independent for the energy equation. Thus, according to [26] should decrease like $\Delta t = O\left(\Delta x^2\right)$.

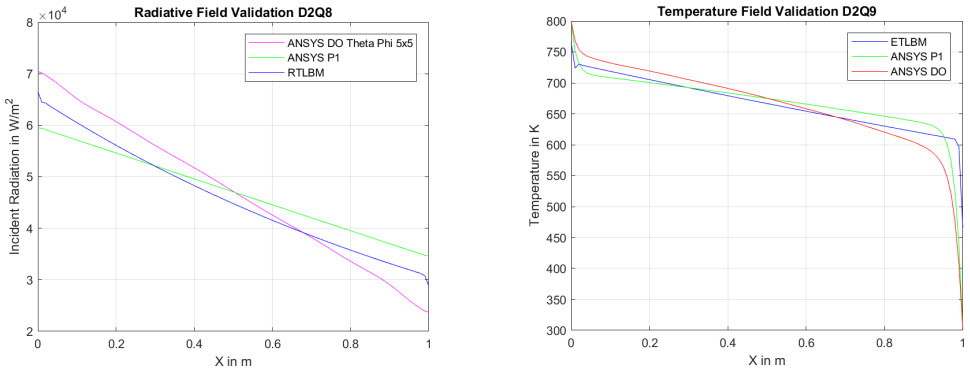

Figure 4.21.: Radiative (D2Q8) and temperature (D2Q9) field validation: $\kappa_a = 0.5\ m^{-1}$

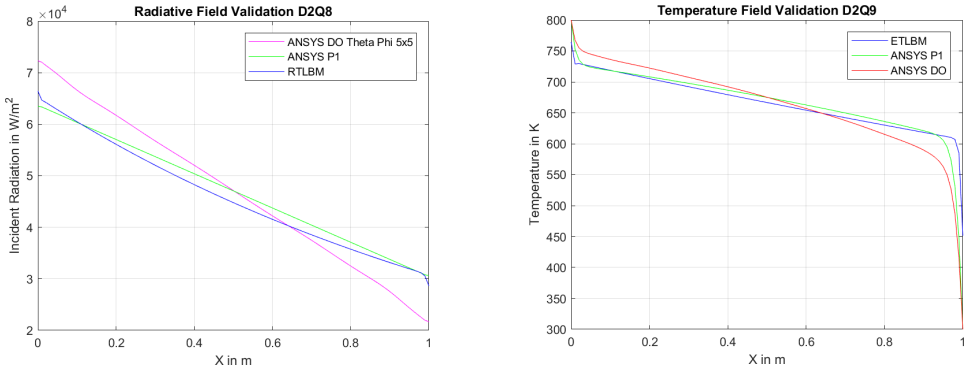

Figure 4.22.: Radiative (D2Q8) and temperature (D2Q9) field validation: $\kappa_a = 0.75\ m^{-1}$

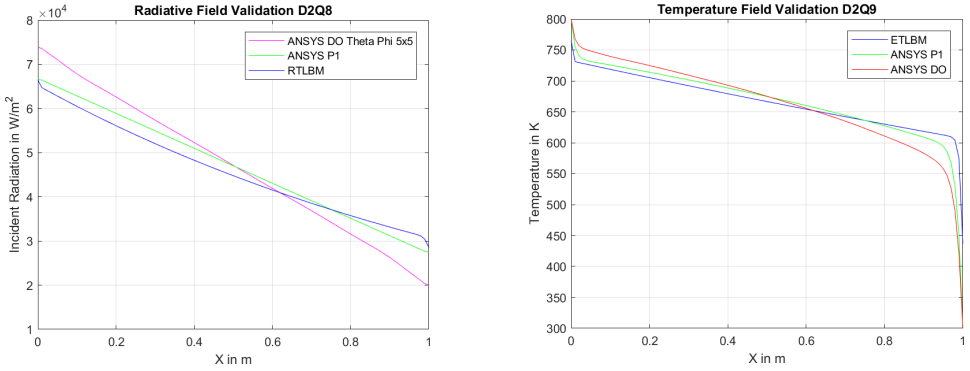

Figure 4.23.: Radiative (D2Q8) and temperature (D2Q9) field validation: $\kappa_a = 1\ m^{-1}$

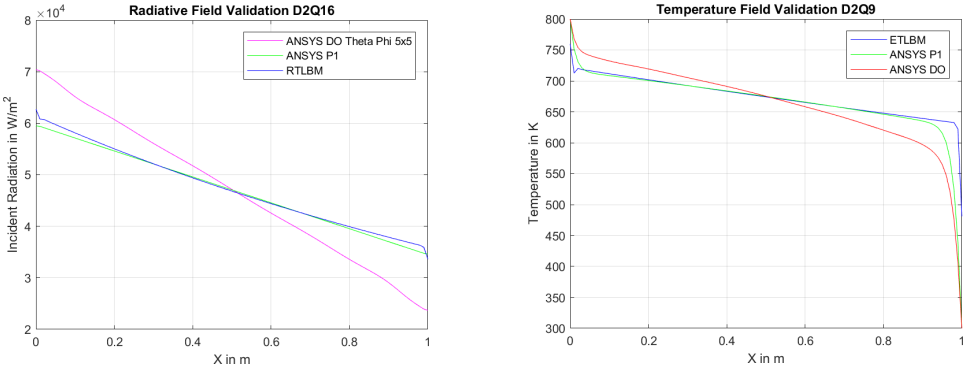

Figure 4.24.: Radiative (D2Q16) and temperature (D2Q9) field validation: $\kappa_a = 0.5\ m^{-1}$

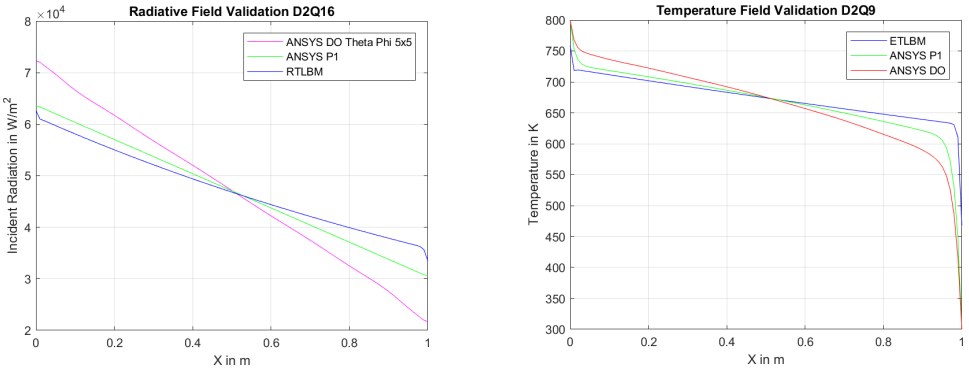

Figure 4.25.: Radiative (D2Q16) and temperature (D2Q9) field validation: $\kappa_a = 0.75\ m^{-1}$

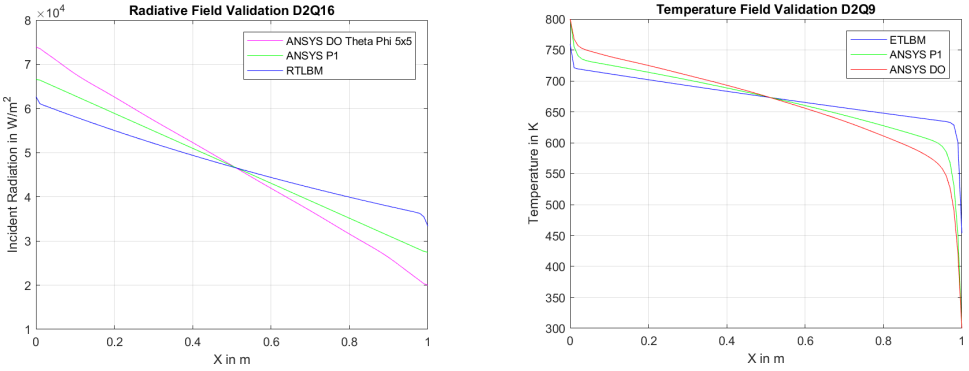

Figure 4.26.: Radiative (D2Q16) and temperature (D2Q9) field validation: $\kappa_a = 1\ m^{-1}$

4.2.2.7. Limitations

A major obstacle in coupling the RTLBE and the ETLBE turned out to be the different relaxation time parameters τ. As for the RTLBE any artificial relaxation parameter would be linked to the absorption coefficient. Thus, any variation has an immanent influence on the absorptive properties. On the other hand, lowering of the relaxation time parameter in the ETLBE may result in stability issues of the solution.

5. Application of the LBM for radiative simulation of industrial furnaces

The common purpose of industrial furnaces, ovens or kilns is to transfer a certain amount of heat Q to a load. The required amount of heat can be calculated from Eq. 5.1 from the loads weight, specific heat and temperature rise. [49]

$$Q = m \cdot c \cdot \Delta T \tag{5.1}$$

There is a large variety of different industrial furnaces available, however, this chapter will focus on the application of the LBM on a walking hearth furnace. *A walking hearth furnace is a heating chamber with loads placed on large refractory slabs for product advancement, with top firing only.* [49]
Furnaces of this kind are used in general as continuous furnaces for the purpose of billet reheating during the production of steel [14]. It is of immense importance to the quality of steel that the temperature distribution inside the slab is uniform when the steel is discharged from the furnace [50].

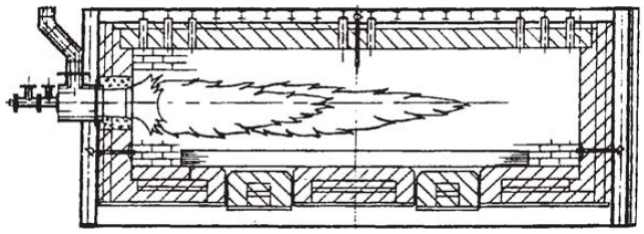

Figure 5.1.: *Walking hearth furnace, cross-section detail* [49]

One of the major disadvantages of walking hearth furnaces is that the load

is only heated from the top. Nevertheless, these types of furnaces have the advantage that apart from rectangular billets, also round billets can be pushed through the furnace. The load advancement is realized through a shift and lift mechanism by the refractory slabs. In figure 5.1 a cross-section through a walking hearth furnace is given, in which the load is heated from the top through a burner positioned on the side wall.

5.1. Furnace configuration

The walking hearth furnace under consideration was already investigated by Prieler et al. [2]. The furnace is natural gas fired and primarily used for the reheating of steel billets. Subsequently figure 5.2 gives a schematic overview of the furnace operation. The furnaces is subdivided in different heating zones, as illustrated. These zones imply different temperature marks and thus a different number as well as configuration of the flat flame burners in use. The billets entering the furnace are initially heated up by the exiting flue gas, before entering the actual pre-heating zone consisting of 8 burners. Subsequently, a cooling wall separates the pre-heating zone from the heating and soaking zone. The number of burners in the heating zone and in the soaking zone is 24 and 16 respectively. The purpose of the cooling wall is, on the one hand, to minimize the heat losses during the loading of the furnace, in order to maintain a constant zone of high temperatures in the heating and soaking zone. On the other hand, the cooling wall represents a reduction of the cross-section of the furnace, and thus, the velocity is locally increased, therefore the convective heat transport is increased as well. The division in separate zones is necessary to sustain a uniform temperature distribution.

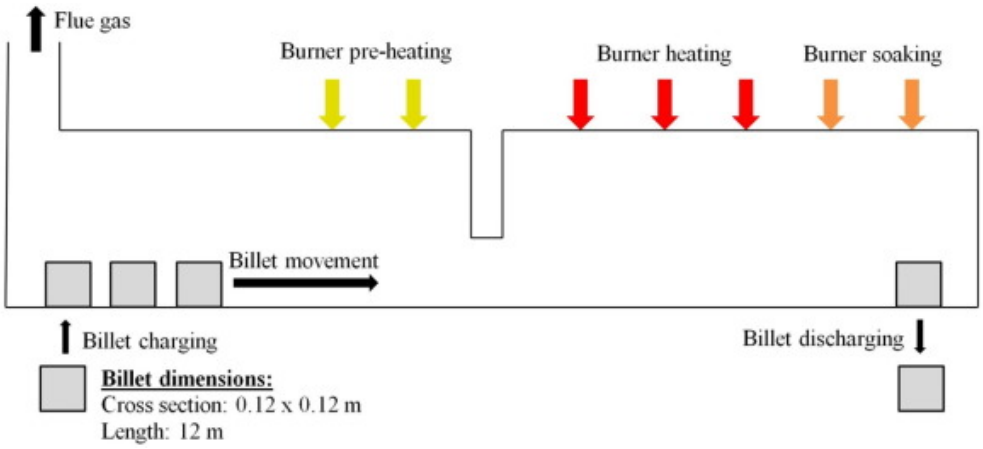

Figure 5.2.: *Schematic figure of the furnace operation* [2]

The physical properties of the furnace medium are given in table 5.1. They represents mass-weighted average values of the three-dimensional CFD simulations from [2].

Table 5.1.: Physical properties of the gas phase in the furnace

physical property	furnace medium
density ρ in (kg/m^3)	0.284
specific heat capacity Cp in $J/(kgK)$	1360.3
thermal conductivity k in $W/(mK)$	0.0454
absorption coefficient κ_a in $1/m$	0.266
molecular viscosity η in $kg/(ms)$	1.72e-05

A separate validation of the LBM model with the physical properties listed above was performed, which showed similar performance as the results using the medium air.

5.2. Applied lattice Boltzmann radiation modelling approach

The walking hearth furnace was modelled using the LBM in three consecutive steps illustrated in Fig. 5.4 - 5.6. A two-dimensional model of the furnace was built, using the longitudinal symmetry plane of the three-dimensional model as a reference (see Fig. 5.3). The flue gas outlet as well as the in- and outlet for the loading of the furnace was not considered. In the first step (Fig. 5.4) the outermost gas enclosure was modelled, which was extended in the second step by the cooling wall (Fig. 5.5). The final model (Fig. 5.6) included a furnace load of 64 billets. The Stark number has a value of $1.7244e-05$ in all of the above described simulation steps, thus, illustrating once again the dominating role of radiation in the heat transfer.

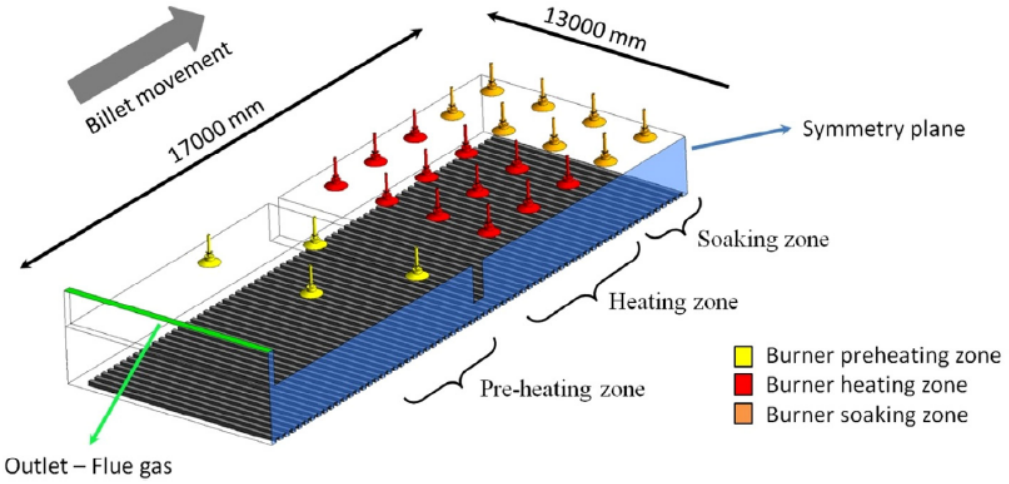

Figure 5.3.: *Configuration of the walking hearth furnace without walls* [2]

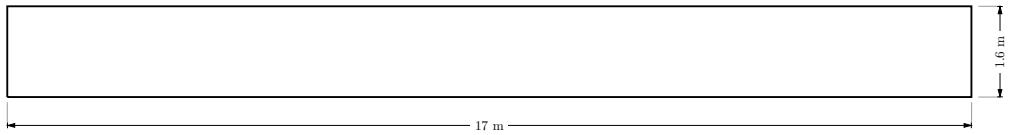

Figure 5.4.: Empty furnace geometry without cooling wall

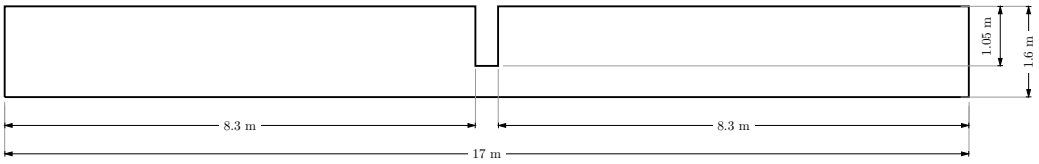

Figure 5.5.: Empty furnace geometry with cooling wall

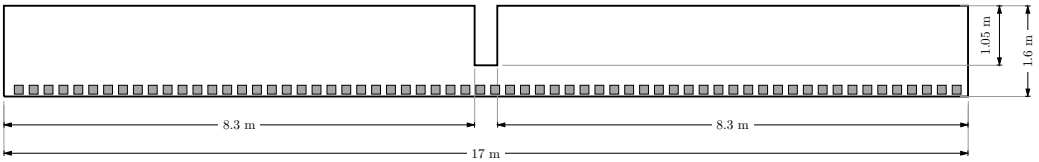

Figure 5.6.: Furnace geometry with cooling wall and 64 billets loaded

5.2.1. Furnace configuration 1: empty furnace geometry without cooling wall

The gas enclosure of the walking hearth furnace investigated was modelled in this first step as a rectangular geometry (see Fig. 5.4). The boundary temperature values were provided through the three-dimensional model by [2]. The temperature profile of the bottom wall was assumed to be linearly increasing from approximately 740 K to 1400 K. The reference solution was provided by a first-order DOM calculation. The validation was performed along the horizontal centre line of the furnace, as illustrated in figure 5.7. The furnace was discretised using a uniform mesh with 400 lattice nodes representing the furnace height, and 4250 lattice nodes representing the furnace length.

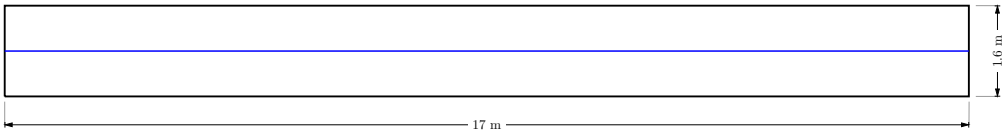

Figure 5.7.: Furnace validation reference lines

In order to demonstrate the effect of the boundary conditions on the LBM solution, figure 5.8 shows the radiative intensity and temperature of the horizontal centre line of the furnace. The temperature calculated using the LBM deviates from the reference solution in the vicinity of the high-temperature boundary, where the values are over-predicted. Consequently, this led to a deviation of the radiative intensity at the high-temperature boundary.
Subsequently, in figure 5.9 a comparison of results is given for a mesh of the size 400×4250, hence equalling an evenly distributed spatial resolution of a node every 40 mm. The results show in general good comparison, however, in the vicinity of the boundaries deviations are visible. The maximum temperature and radiative intensity values illustrated by the colour-bar are limited to a small region in the north-east corner of the furnace, and thus are not noticeable in the figure itself.

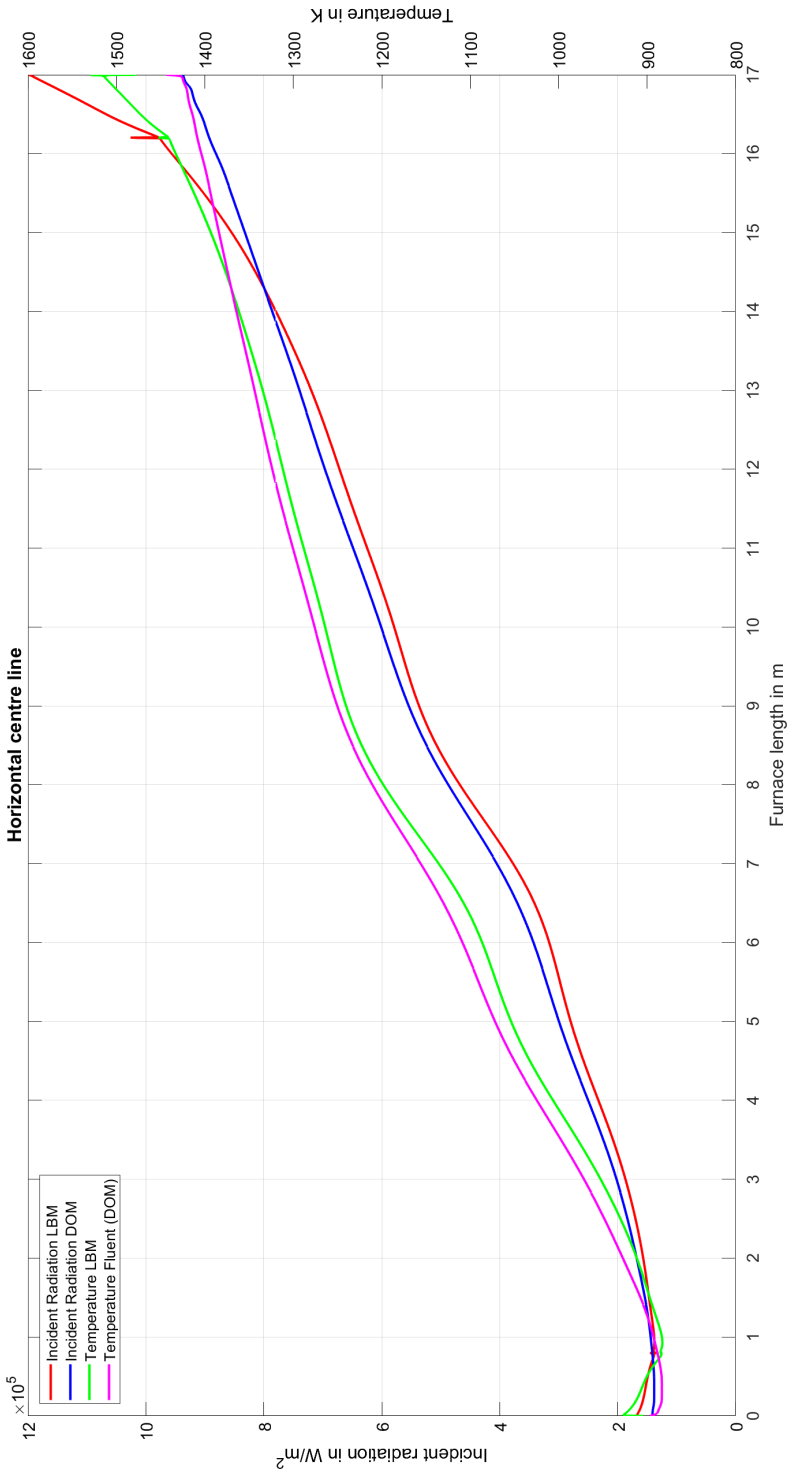

Figure 5.8.: Furnace configuration 1: comparison of the radiative intensity on the horizontal centre line of the furnace

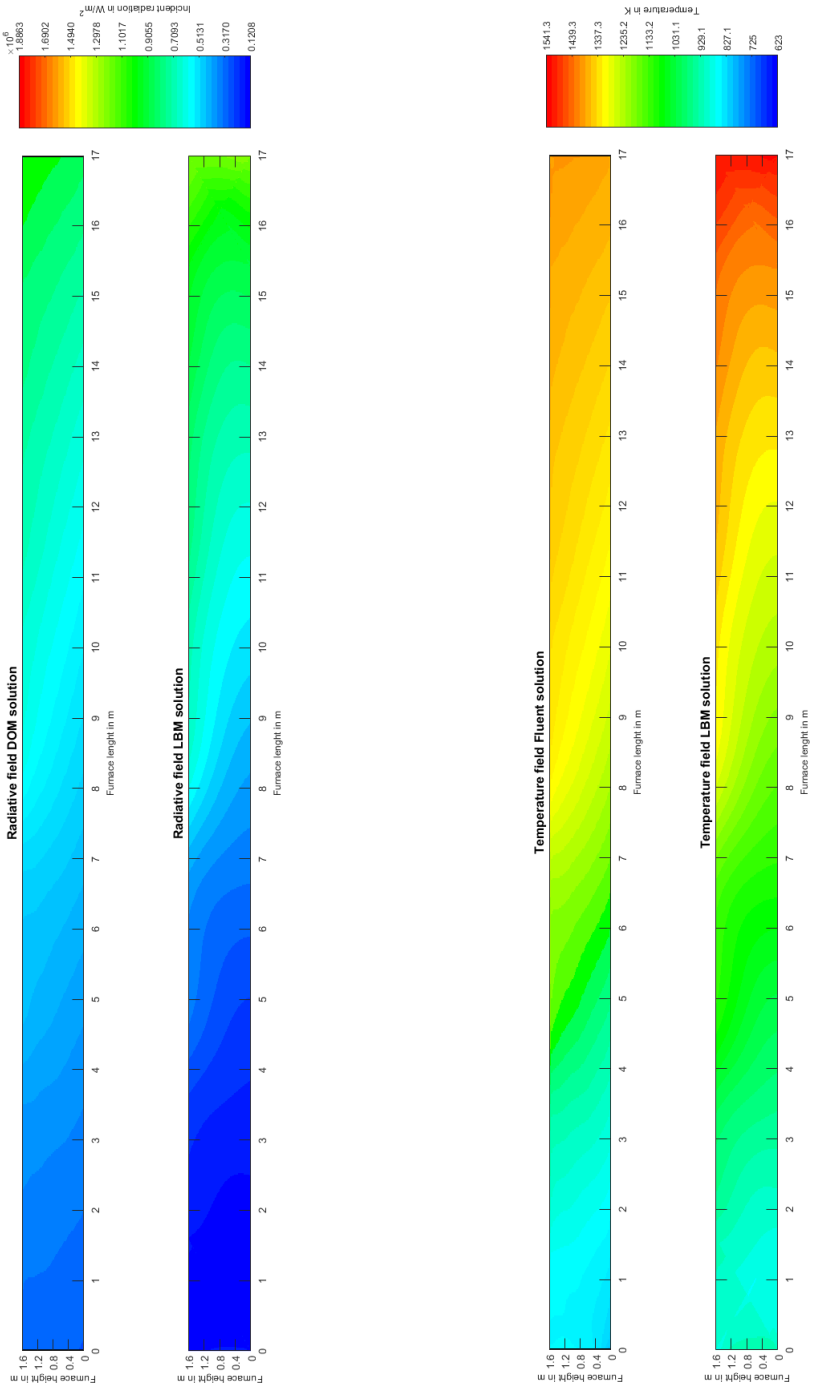

Figure 5.9.: Furnace configuration 1: comparison of the LBM and DOM results

5.2.2. Furnace configuration 2: empty furnace geometry with cooling wall

In the second step the cooling wall was added to the furnace geometry (see Fig. 5.5). The cooling wall itself was modelled by a temperature gradient given between the pre-heating zone and the heating zone. The temperature gradient caused by the cooling wall has been set for this case to approximately 109K and is assumed to be linear. The furnace was discretised using a uniform mesh with 400 lattice nodes representing the furnace height, and 4250 lattice nodes representing the furnace length.

Results (Fig. 5.10) show in general good comparison with the DOM solution, however, in the vicinity of the boundaries major deviations are detectable. This was presumably caused by the temperature boundary condition. Previous results of the empty furnace geometry (see Sec. 5.2.1) have shown that in the vicinity of high temperature gradients the developed LBM is prone to error. Furthermore, a slight over-prediction of quantities is visible in the soaking zone of the furnace, as compared to the reference solution.

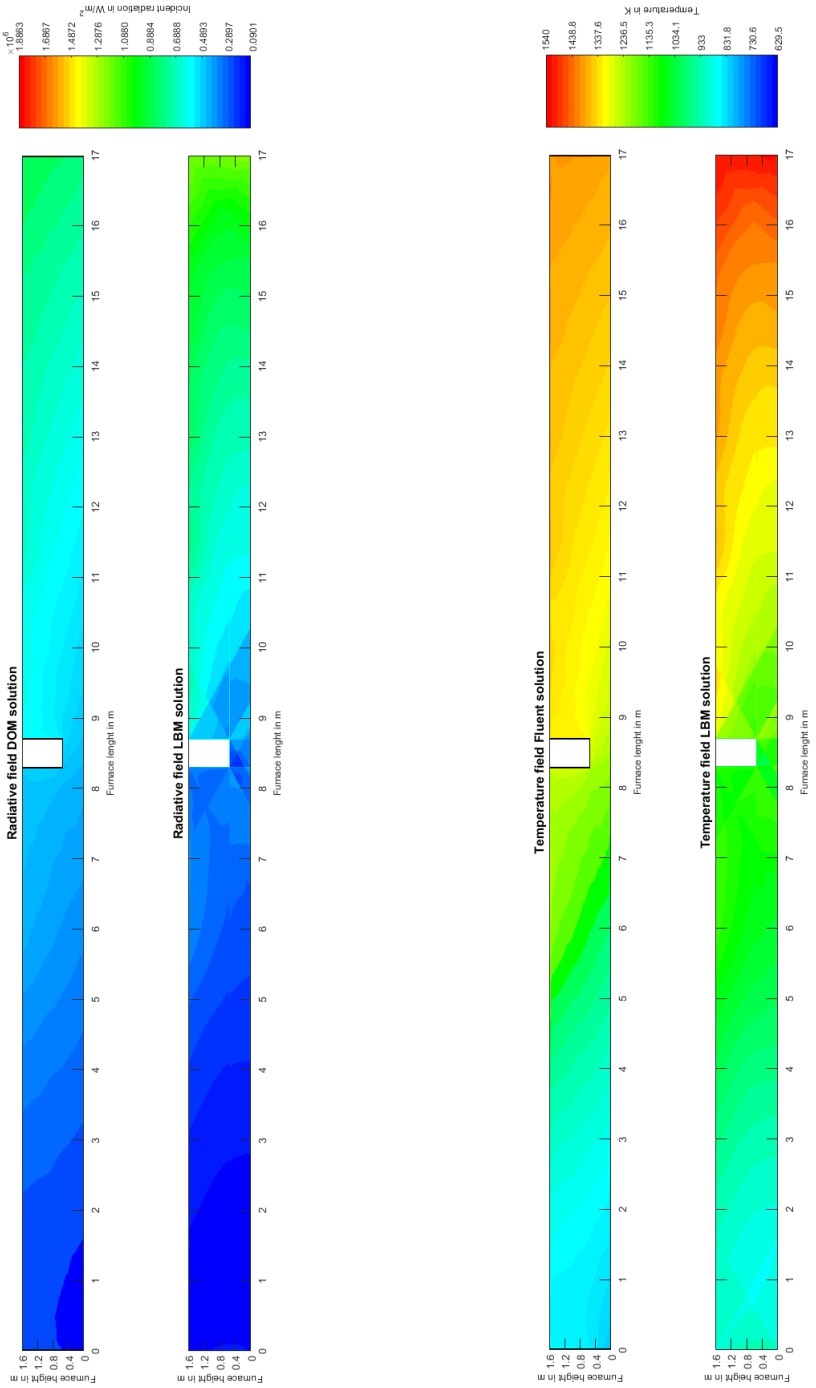

Figure 5.10.: Furnace configuration 2: comparison of the LBM and DOM results

5.2.3. Furnace configuration 3: furnace geometry with cooling wall and billets loaded

In the last step billets were added to the furnace geometry. The reference solution was calculated once again in Fluent using a first order DOM as well as the P1 model. Initially the same uniform mesh of the size 400×4250 was used for both the LBM and their respective reference solutions calculated in Fluent. Due to the high computational effort the mesh was only discretised further for the LBM model, as given by the table 5.2 below.

Table 5.2.: Mesh size for the modelling of the final furnace simulation using the LBM

	initial mesh	high resolution mesh
size	400×4250	800×8500

The results for the initial mesh of the size 400×4250 are given in figure 5.11, in which the good comparison between the LBM and DOM is evident for the main gas phase. The increased radiation and temperature levels in the soaking zone of the LBM solution were caused by the boundary conditions. The same behaviour of the developed LBM was encountered in the validation test case. The boundary conditions for the billets in the Fluent solution was implemented using an increasing linear temperature profile provided by a user-defined function (UDF). Subsequently, the results of the furnace simulation using the P1 model are illustrated (Fig. 5.12). The solution was calculated in Fluent using the same mesh as was previously used for the calculation with the DOM. The results are en bloc comparable to those calculated using the DOM.

Further discretisation of the mesh, to a size of 800×8500 nodes, for the LBM model led to a lower maximum temperature, presumably caused by the decrease of artefacts through better mesh resolution, as can be seen in figure 5.13. Evidently the mesh resolution seems to have only minor effects on the radiative field.

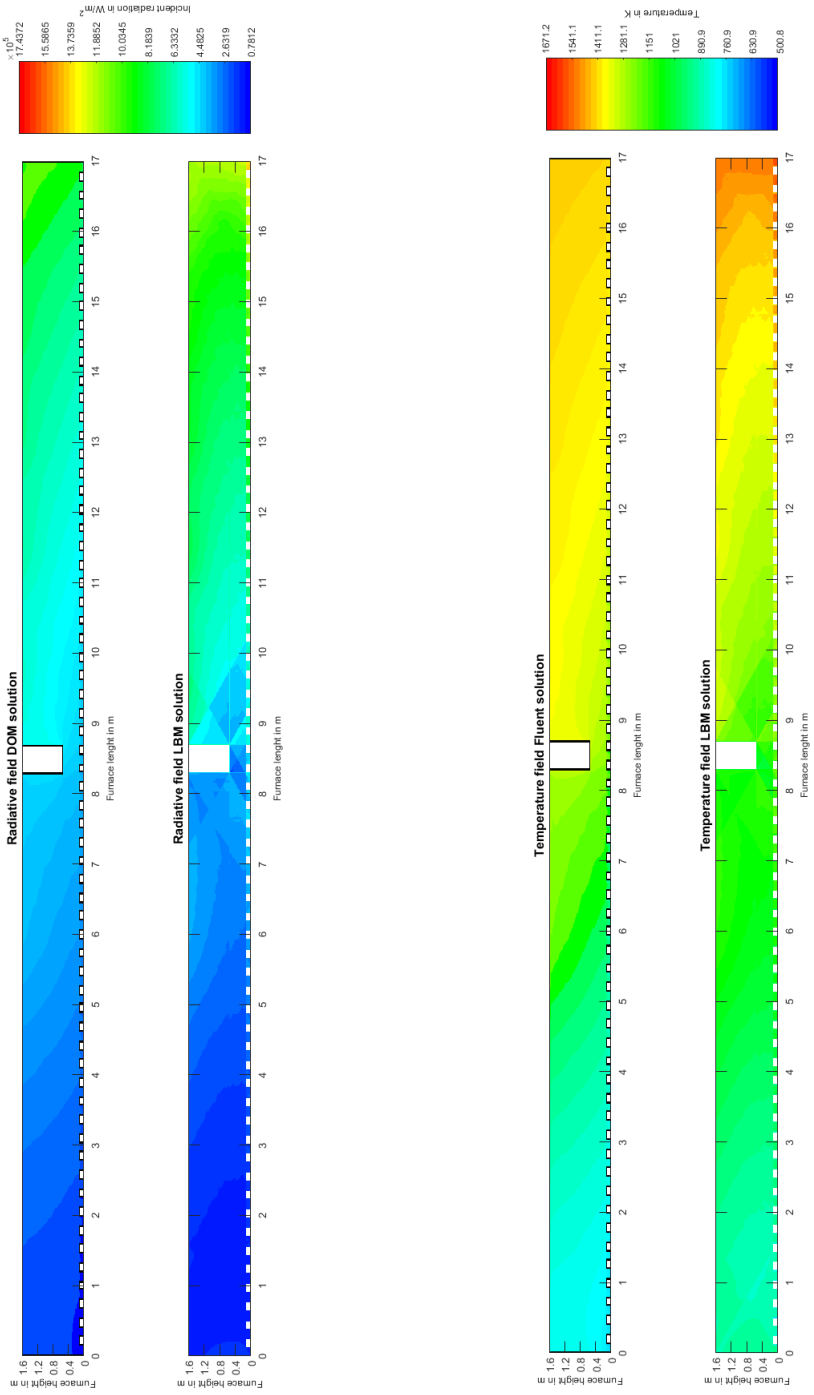

Figure 5.11.: Furnace configuration 3: comparison of the LBM and DOM results

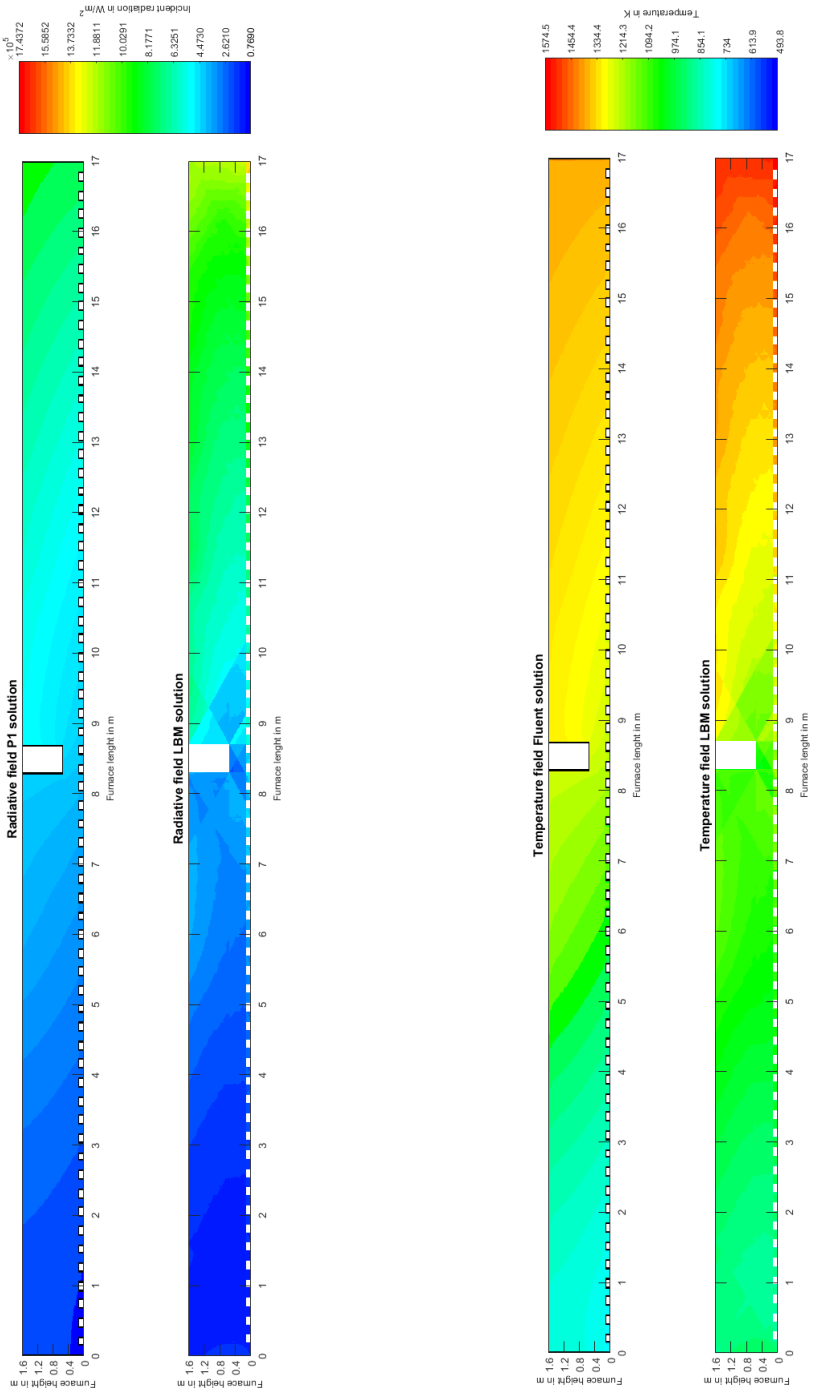

Figure 5.12.: Furnace configuration 3: comparison of the LBM and P1 results

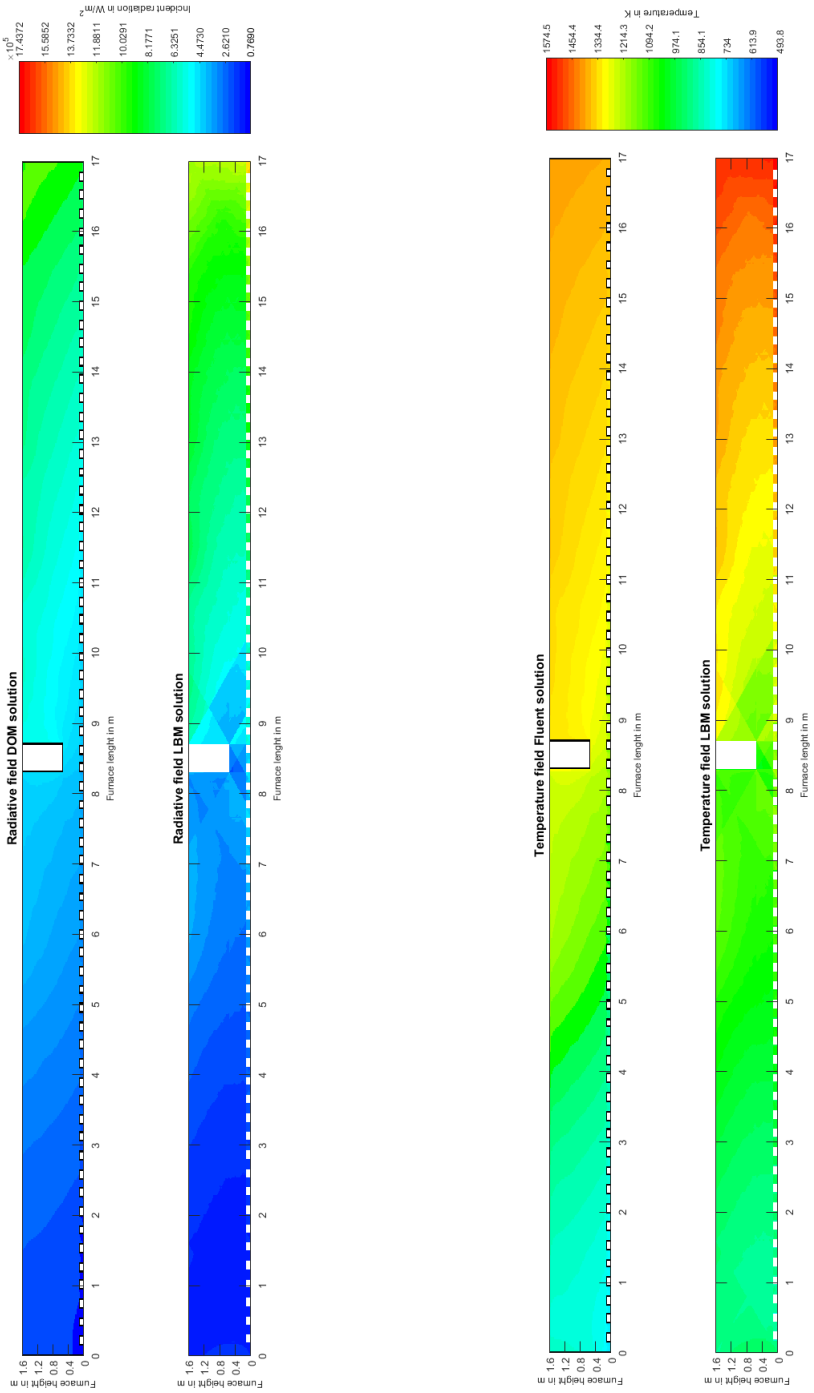

Figure 5.13.: Furnace configuration 3: comparison of the LBM and DOM results (high resolution mesh)

5.2.3.1. Truncation criterion

In all of the presented LBM calculations the solution was deemed to be stable if the maximum change of one cell node value prior to the last simulation was smaller than $1E-06$. Analysis of the error development showed a steady but slow decrease for the radiative solution, whilst the solution of the energy transport equation was achieved significantly faster. This led to a total simulation runtime of the final furnace model (see Fig. 5.6) of approximately 36 hours for the high resolution mesh, using a computer with an Intel i3 CPU with 3.4 GHz and 8 GB RAM.

5.3. Billet heating

The radiative intensity in the cells prior to the billets was compared amongst the three methods (LBM, DOM, P1). Figure 5.14 shows the mean average radiative intensity per billet, calculated from their respective adjacent cells.

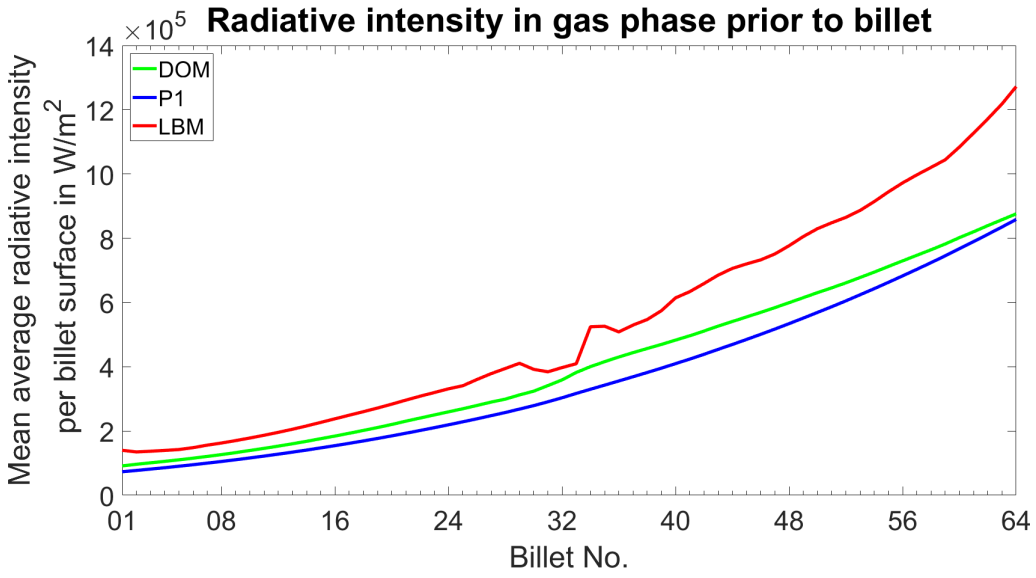

Figure 5.14.: Mean radiative intensity in gaseous phase prior to billets

In the first third of the furnace the results of the LBM are in good accordance with the reference solution. However, in the vicinity of the cooling wall the high temperature gradients cause deviations. With increasing temperature in the heating and soaking zone of the furnace the deviation between the LBM solution and the reference solutions increases.
The radiative heat flux transferred onto the billets was calculated from the difference of the incident radiation on the boundary and the nodes prior to selfsame (see Fig. 5.15).

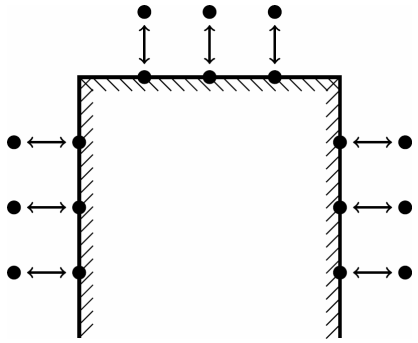

Figure 5.15.: Lattice nodes used for the calculation of the radiative heat flux on the billets

For better visualisation the mean value of the three resulting billet wall fluxes was calculated and compared to those computed in Fluent. It is clearly visible in Fig. 5.16, that with increasing proximity to the cooling wall the heat fluxes, which were calculated using the LBM, deviate strongly from the CFD solutions. The ongoing deviation in the heating and soaking zone of the furnace is linked to the increased incident radiation in these zones (see Fig. 5.14).

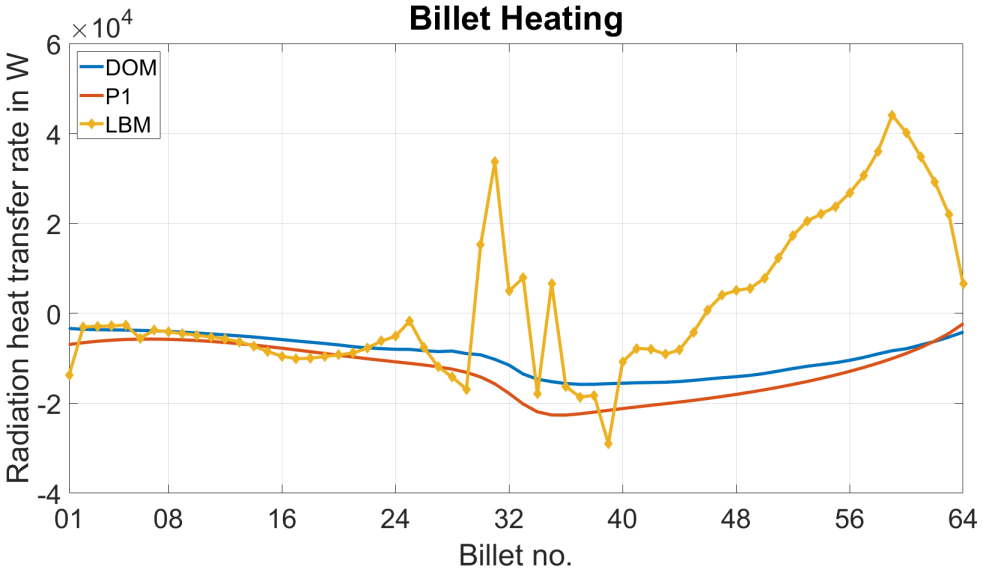

Figure 5.16.: Comparison of transferred heat onto billets between the LBM, DOM and P1 model

5.3.1. Temperature distribution inside the solid steel billet

The heat equation given below was used to calculate the billet heating, as heat inside the billets is only transferred through conduction. The holding time of each billet at its respective position was 100 s. Thus, the heat transfer could be calculated for each billet, starting from the known initial condition for the first billet, which was supplied to the furnace at an ambient temperature of 20° C. The density of the steel billets was assumed to be 7800 kg/m^3.

$$\frac{\partial \rho h}{\partial t} = \nabla \left(k \nabla T \right) \tag{5.2}$$

The left-hand-side of Eq. 5.2 denotes the temporal temperature change respectively the temporal change of enthalpy which relates to the temperature as following,

$$h = c \cdot T \tag{5.3}$$

in which c denotes the specific heat capacity of the steel and T denotes to the temperature of the billet whereat the reference temperature was set to zero. The right-hand-side of Eq. 5.2 denotes the spatial change in temperature due to

conduction, described by the thermal conductivity parameter k. The physical properties parameters of the steel were assumed to be constant.
The boundary temperature values were calculated from the radiative field reversing the previously described boundary condition.

$$T_{Wall} = \frac{11}{18} \cdot \sqrt[4]{\frac{I}{\sigma}} \tag{5.4}$$

The factor $\frac{11}{18}$ introduced in Eq. 5.4 represents the sum of node weighting values of the lattice used for solving the heat transfer equation in the furnace, as illustrated in figure 5.17 (centre node, one primary direction node an two diagonal nodes). The conversion factor is needed in order to gain the surface

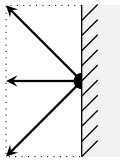

Figure 5.17.: Node weights used for the calculation of the conversion factor of boundary temperature values

temperature values of the gas enclosure from the incident radiation values. The heat transfer equation was solved using a LBE (cf. Sec. 3.4) with both a D2Q5 and D2Q9 lattice arrangement. The advantage of the D2Q5 lattice arrangement in this particular case is the significantly reduced calculation time, as well as the fact, that the initial boundary condition data from the furnace provided relatively low resolution for the billet surfaces.
In case of such low resolution source data a high resolution lattice arrangement such as the D2Q9 showed less advantageous, because of a higher affinity for artefacts in the solution caused by the diagonal streaming steps.
Exemplary the heat conduction for the eighth billet was calculated in a steady state simulation at the end of its holding time ($t_{Billet} = 100$ s). A comparison of results was provided by a Fluent solution. Both solutions were initialised with the same set of boundary conditions calculated from the LBM solution, in order to meaningfully compare results in regard to the heat conduction. The pseudo-time step for the ETLBE was set to $\Delta t = 0.5$ for this particular case. The results for the horizontal and vertical centre lines are given in Fig. 5.18. An exceedingly good comparison of the LBM results with those of the CFD

solution is visible. The increase of the temperature values towards the right side of the billet is caused by the incoming radiation from the ninth billet. As the distance between the neighbouring billets is closer than the top wall of the furnace, thus, meaning a shorter path of transport for the PDFs, the billets side walls have a higher temperature than the billets top wall.

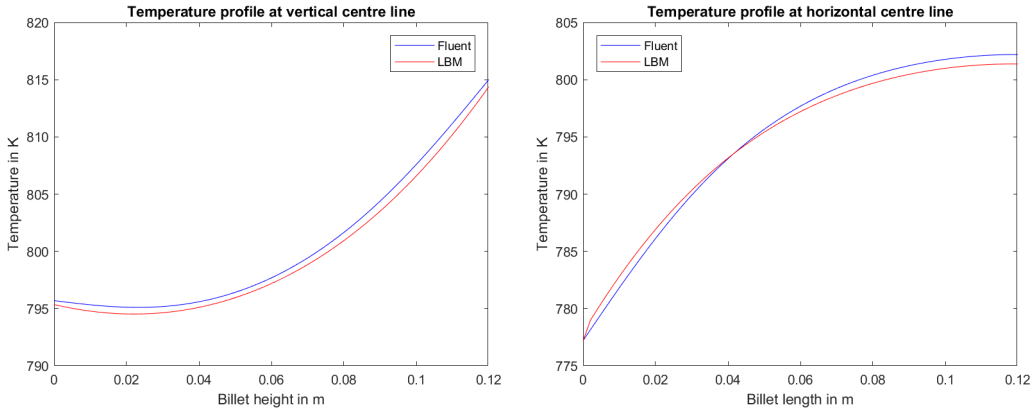

Figure 5.18.: Comparison of heat conduction between the Fluent and LBM solution for the heating of the eighth billet

The heat distribution for the eighth billet is given by Fig. 5.19. The overall good comparability between the solution methods for the same given set of boundary conditions is evident.

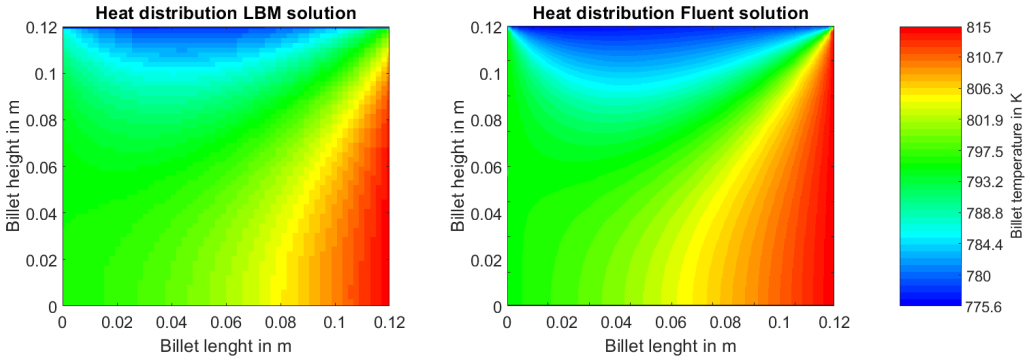

Figure 5.19.: Comparison of the heat distribution in the eighth billet; left LBM (D2Q5), right Fluent solution

5.4. Discussion of results

With increasing complexity of the furnace geometry deviations between the LBM and the CFD solutions are visible. The boundary conditions used, in particular the energy equations boundary condition, is prone to error as quasi fictitious values are imposed through the weighting of the given temperature value in different directions (cf. appendix C). The overestimation of the temperature values especially in the vicinity of the billet outlet at the end of the furnace, which is reflected in the incident radiation results, could be overcome through an adaptation of the pseudo-time step in the formulation of the ETLBE. However, caution is advised since any change of the pseudo-time step is linked to the relaxation time parameter, and thus the physical properties of the gas enclosure.

6. Conclusions

The LBM was successfully applied to predict the radiative heat transfer in a gas enclosure. The model was thoroughly validated, for both the calculation of the radiative transfer and the energy transfer, as well as the resulting two-way coupled model to simulate radiative heat transfer in participating media. The effect of different physical properties (e.g. κ_a) on the results were studied, as well as different geometrical solution approaches. The LBM furnace simulations were carried out using a customary budget computer with an Intel i3 CPU with 3.4 GHz and 8 GB RAM.
The code validation revealed that the implemented temperature boundary condition is prone to error, depending on the temperature gradients and the absorption coefficient chosen. Thus, these errors occur only in the close proximity of the boundary itself. Overall, a good comparison between the LBM and the CFD solutions, respectively the DOM and P1 method, could be achieved. The gas enclosure of the investigated walking hearth furnace was successfully modelled using the LBM. However, the same issues were encountered as in the validation test case. Especially in zones of high temperatures and temperature gradients an over-prediction of quantities was visible.
Major issue throughout the development process remained the numerical stability of the code, this was especially the case for the energy equation and its dependency of the relaxation-time parameter on the chosen grid. Apart from the numerical stability the implemented boundary condition of the energy equation proved to be prone for errors with increasing temperature gradients. Future development of the radiative LBM models should target three-dimensional calculation of the radiative heat transfer, as well as the option to include different wall emissivities and in general enhanced boundary conditions. Due to the increasing computational effort it is highly recommended to focus further code design on `C` or `C++` type programming languages to enable an optimized workflow. The extension to a transient model might prove useful, especially under consideration of future coupling of the LBEs in multi-physics problems.

An accurate knowledge of the numerical accuracy of the method and in particular the boundary conditions, which have substantial influence on selfsame, will decide the future of the LBM in the prediction of radiative heat transfer in industrial furnaces.

Appendix

Appendix A.

Macroscopic conservation equations of radiation

The foundation amongst many publications concerning the modelling of radiative transfer using the LBM is an article written by Ma et al. [32], whereupon this section is primarily based.

The starting point is the Boltzmann equation of photon transfer in phase space derived from the equations of radiation hydrodynamics by [33]. *The discipline of radiation hydrodynamics is the branch of hydrodynamics in which the moving fluid absorbs and emits electromagnetic radiation, and in so doing modifies its dynamical behavior.* [51]
In phase space, the Boltzmann equation of photon transfer can be written as

$$\frac{\partial f_\nu(\mathbf{r},\Omega,t)}{\partial t} + \nabla\cdot[\mathbf{v} f_\nu(\mathbf{r},\Omega,t)] + \nabla_\nu\cdot[\mathbf{a}\ f_\nu(\mathbf{r},\Omega,t)] = Q_\nu(\mathbf{r},\Omega,t) \qquad \text{(A.1)}$$

where ν is the frequency associated with each photon; r is the vector of spatial position; Ω is the direction of travel of the photon; t is time; $\mathbf{v}$ and $\mathbf{a}$ are microscopic velocity and acceleration, respectively; ∇ and ∇_ν are the divergence operators in geometric space and velocity space, respectively; $f_\nu(\mathbf{r},\Omega,t)$ is the distribution function of the photon; and $Q_\nu(\mathbf{r},\Omega,t)$ is the source of photons, including the contributions of absorption, emission, and scattering in the radiation field. For a medium with a uniform refractive index, ignoring the relativistic effect, $\mathbf{a}=0$ and $\mathbf{v}=c\Omega$, Eq. A.1 can be simplified and written as:

$$\frac{\partial f_\nu(\mathbf{r},\Omega,t)}{\partial t} + c\nabla\cdot[\mathbf{\Omega} f_\nu(\mathbf{r},\Omega,t)] = Q_\nu(\mathbf{r},\Omega,t) \qquad \text{(A.2)}$$

where c is the velocity of light in space. [32]
Regarding only absorption and thus neglecting scattering the source term in Eq. A.2 is supplemented with an emission source function of photons $q_\nu(\mathbf{r}, \mathbf{\Omega}, t)$.

$$\frac{\partial f_\nu(\mathbf{r}, \mathbf{\Omega}, t)}{\partial t} + c\mathbf{\Omega} \cdot \nabla f_\nu(\mathbf{r}, \mathbf{\Omega}, t) = q_\nu(\mathbf{r}, \mathbf{\Omega}, t) - c\kappa_{a,\nu}(\mathbf{r}, t) f_\nu(\mathbf{r}, \mathbf{\Omega}, t) \quad \text{(A.3)}$$

The number of absorbed photons is described by the term $f_\nu(\mathbf{r}, \mathbf{\Omega}, t)$. Next the radiative intensity $I_\nu(\mathbf{r}, \mathbf{\Omega}, t)$ is introduced. Selfsame is a function of the speed of light, the Planck's constant, the frequency and the number of absorbed photons; $I_\nu(\mathbf{r}, \mathbf{\Omega}, t) = ch\nu f_\nu(\mathbf{r}, \mathbf{\Omega}, t)$.

$$\frac{\partial I_\nu(\mathbf{r}, \mathbf{\Omega}, t)}{\partial t} + \mathbf{\Omega} \cdot \nabla I_\nu(\mathbf{r}, \mathbf{\Omega}, t) = S_\nu(\mathbf{r}, \mathbf{\Omega}, t) - \kappa_{a,\nu} I_\nu(\mathbf{r}, \mathbf{\Omega}, t) \quad \text{(A.4)}$$

The term S_ν represents a source term which denotes the rate of energy emission caused by spontaneous processes. Selfsame is defined as

$$S_\nu(\mathbf{r}, \mathbf{\Omega}, t) = h\nu q_\nu(\mathbf{r}, \mathbf{\Omega}, t) = n^2 \kappa_{a,\nu} I_{b\nu} \quad \text{(A.5)}$$

in which the refractive index n and the specific black body emission intensity $I_{b\nu}$ is introduced. Rewriting the second term on the left-hand-side of Eq. A.4 in which s represents the length along $\mathbf{\Omega}$,

$$\mathbf{\Omega} \cdot \nabla I_\nu(\mathbf{r}, \mathbf{\Omega}, t) = \frac{\partial I_\nu(\mathbf{r}, \mathbf{\Omega}, t)}{\partial s} \quad \text{(A.6)}$$

the RTE, without scattering for a medium with a uniform refractive index, can be written as following:

$$\frac{\partial I_\nu(\mathbf{r}, \mathbf{\Omega}, t)}{c\partial t} + \frac{\partial I_\nu(\mathbf{r}, \mathbf{\Omega}, t)}{\partial s} = n^2 \kappa_{a,\nu} I_{b,\nu} - \kappa_{a,\nu} I_\nu(\mathbf{r}, \mathbf{\Omega}, t) \quad \text{(A.7)}$$

Integration of the initial RTE given by Eq. A.4 over all directions in space holds,

$$\begin{aligned} \int_{4\pi} \frac{\partial I_\nu(\mathbf{r}, \mathbf{\Omega}, t)}{c\partial t} d\mathbf{\Omega} + \int_{4\pi} \mathbf{\Omega} \cdot \nabla I_\nu(\mathbf{r}, \mathbf{\Omega}, t)\, d\mathbf{\Omega} = \\ \int_{4\pi} S_\nu(\mathbf{r}, \mathbf{\Omega}, t)\, d\mathbf{\Omega} - \int_{4\pi} \kappa_{a,\nu} I_\nu(\mathbf{r}, \mathbf{\Omega}, t)\, d\mathbf{\Omega} \end{aligned} \quad \text{(A.8)}$$

which can be rewritten by factoring out the constants

$$\frac{\partial}{c\partial t}\left(\int_{4\pi} I_\nu\left(\mathbf{r},\mathbf{\Omega},t\right)d\mathbf{\Omega}\right)+\nabla\cdot\left(\int_{4\pi}\mathbf{\Omega}I_\nu\left(\mathbf{r},\mathbf{\Omega},t\right)d\mathbf{\Omega}\right)= \int_{4\pi} S_\nu\left(\mathbf{r},\mathbf{\Omega},t\right)d\mathbf{\Omega}-\kappa_{a,\nu}\int_{4\pi} I_\nu\left(\mathbf{r},\mathbf{\Omega},t\right)d\mathbf{\Omega} \tag{A.9}$$

Next the radiative energy density (Eq. A.10), the radiative heat flux (Eq. A.11) and the radiative momentum (Eq. A.12) are in introduced.

$$E_\nu=\int_{4\pi} h\nu f_\nu\left(\mathbf{r},\mathbf{\Omega},t\right)d\mathbf{\Omega}=\frac{1}{c}\int_{4\pi} I_\nu\left(\mathbf{r},\mathbf{\Omega},t\right)d\mathbf{\Omega} \tag{A.10}$$

$$\mathbf{F}_\nu=\int_{4\pi}\mathbf{\Omega}h\nu c f_\nu\left(\mathbf{r},\mathbf{\Omega},t\right)d\mathbf{\Omega}=\int_{4\pi}\mathbf{\Omega}I_\nu\left(\mathbf{r},\mathbf{\Omega},t\right)d\mathbf{\Omega} \tag{A.11}$$

$$\mathbf{P}_\nu=\frac{1}{c}\int_{4\pi}\mathbf{\Omega}\Omega h\nu c f_\nu\left(\mathbf{r},\mathbf{\Omega},t\right)d\mathbf{\Omega}=\frac{1}{c}\int_{4\pi}\mathbf{\Omega}\Omega I_\nu\left(\mathbf{r},\mathbf{\Omega},t\right)d\mathbf{\Omega} \tag{A.12}$$

The radiative energy conservation equation is given from the above as following, where Q_ν represents the source of radiative energy:

$$\frac{\partial E_\nu}{\partial t}+\nabla\cdot\mathbf{F}_\nu=Q_\nu-c\kappa_{a,\nu}E_\nu \tag{A.13}$$

Equation A.13 can alternatively be gained from Eulerian hydrodynamics. As opposed to the Lagrangian equations which move with the fluid at fluid velocity the Eulerian description is streamed through by the fluid and thus describes parameters at each point in time and space. The radiation energy density (Eq. A.14), radiation momentum (Eq. A.15), radiation energy flux (Eq. A.16) as well as the radiation momentum flux (Eq. A.17) are given below.

$$E_{r,\nu}=\int_{4\pi} h\nu f_\nu\left(\mathbf{r},\mathbf{\Omega},t\right)d\mathbf{\Omega}=E_\nu \tag{A.14}$$

$$\mathbf{M}_{R,\nu}=\int_{4\pi}\left(\frac{h\nu\mathbf{\Omega}}{c}\right)f_\nu\left(\mathbf{r},\mathbf{\Omega},t\right)d\mathbf{\Omega}=\frac{\mathbf{F}_\nu}{c^2} \tag{A.15}$$

$$\mathbf{E}_{RF,\nu}=\int_{4\pi} h\nu c\mathbf{\Omega}f_\nu\left(\mathbf{r},\mathbf{\Omega},t\right)d\mathbf{\Omega}=\mathbf{F}_\nu \tag{A.16}$$

$$\mathbf{M}_{RF,\nu}=\int_{4\pi} c\mathbf{\Omega}\left(\frac{h\nu\mathbf{\Omega}}{c}\right)f_\nu\left(\mathbf{r},\mathbf{\Omega},t\right)d\mathbf{\Omega}=P_\nu \tag{A.17}$$

The Eulerian conservation equation in vector notation can be written as

$$\frac{\partial D}{\partial t} + \nabla \mathbf{F} = W \tag{A.18}$$

where $\mathbf{D}$, $\mathbf{F}$, *and* $\mathbf{W}$ *express density, flux, and source for any quantity, respectively* [32]. Substitution of the radiation momentum (Eq. A.15), radiation energy flux (Eq. A.16) and the radiation momentum flux (Eq. A.17) in the Eulerian conservation equation (Eq. A.18) renders,

$$\frac{\partial E_\nu}{\partial t} + \nabla \mathbf{F}_\nu = W_\nu \tag{A.19}$$

$$\frac{\partial \mathbf{F}_\nu}{c^2 \partial t} + + \nabla \mathbf{P}_\nu = 0 \tag{A.20}$$

in which external radiative energy sources, including emission and absorption of energy, are denoted by the term W_ν. The above derived macroscopic radiative conservation equations form the basis of connection to be considered with the LBM.
The LBM for this specific case has been constructed using a SRT approach as following:

$$I_{\nu,\mathbf{\Omega}}\left(\mathbf{r} + c\mathbf{\Omega}\Delta t, t + \Delta t\right) - I_{\nu,\mathbf{\Omega}}\left(\mathbf{r}, t\right) = -\frac{1}{\tau}\left[I_{\nu,\mathbf{\Omega}}\left(\mathbf{r}, t\right) - I^{eq}_{\nu,\mathbf{\Omega}}\left(\mathbf{r}, t\right)\right] + S_{\nu,\mathbf{\Omega}}\left(\mathbf{r}, t\right)\Delta t + w_{\mathbf{\Omega}} I_{\nu,\mathbf{\Omega}}\left(\mathbf{r}, t\right)\Delta t \tag{A.21}$$

The equilibrium PDF should obey the conservation conditions stated by Eqs. A.10 - A.12.

$$E_\nu = \frac{1}{c}\int_{4\pi} I_{\nu,\mathbf{\Omega}}\left(\mathbf{r}, t\right) = \frac{1}{c}\sum_{\mathbf{\Omega}} I^{eq}_{\nu,\mathbf{\Omega}}\left(\mathbf{r}, t\right) \tag{A.22}$$

$$\mathbf{F}_\nu = \sum_{\mathbf{\Omega}} \mathbf{\Omega} I_{\nu,\mathbf{\Omega}}\left(\mathbf{r}, t\right) = \sum_{\mathbf{\Omega}} \mathbf{\Omega} I^{eq}_{\nu,\mathbf{\Omega}}\left(\mathbf{r}, t\right) \tag{A.23}$$

$$\mathbf{P}_\nu = \frac{1}{c}\sum_{\mathbf{\Omega}} \mathbf{\Omega}\mathbf{\Omega} I_{\nu,\mathbf{\Omega}}\left(\mathbf{r}, t\right) = \frac{1}{c}\sum_{\mathbf{\Omega}} \mathbf{\Omega}\mathbf{\Omega} I^{eq}_{\nu,\mathbf{\Omega}}\left(\mathbf{r}, t\right) \tag{A.24}$$

The one-dimensional form of Eq. A.21 is written as following:

$$I_{\nu,\Omega}\left(x + c\Omega\Delta t, t + \Delta t\right) - I_{\nu,\Omega}\left(x, t\right) = -\frac{1}{\tau}\left[I_{\nu,\Omega}\left(x, t\right) - I^{eq}_{\nu,\Omega}\left(x, t\right)\right] + S_{\nu,\Omega}\left(x, t\right)\Delta t + w_{\Omega} I_{\nu,\Omega}\left(x, t\right)\Delta t \tag{A.25}$$

where Ω denotes the direction of radiative transfer. The PDF of the radiative intensity has been formally written as f_i as introduced in Ch. 3. A Taylor series expansion of the left-hand-side yields:

$$f_i\left(x + c\Omega\Delta t, t + \Delta t\right) = \sum_{n=0}^{\infty} \frac{\Delta t^n}{n!} \left(\partial_t + c\Omega\nabla\right)^n f_i\left(x,t\right) \tag{A.26}$$

Next the Taylor series expansion up to the second order is introduced in Eq A.25,

$$\begin{aligned}\Delta t \left(\partial_t + c\Omega\nabla\right) f_i\left(x,t\right) + \frac{\Delta t^2}{2}\left(\partial_t + c\Omega\nabla\right)^2 f_i\left(x,t\right) = \\ -\frac{1}{\tau}\left[I_{\nu,\Omega}\left(x,t\right) - f_i^{eq}\left(x,t\right)\right] + S\left(x,t\right)\Delta t + w_\Omega f_i\left(x,t\right)\Delta t\end{aligned} \tag{A.27}$$

Introducing perturbation series of the PDF the time and spatial scale as well as the source term lead to Eqs. A.28 - A.31. Note that the one-dimensional form of the spatial derivation is now written instead of ∇ as $\frac{\partial}{\partial x} = \partial_x$.

$$f_i = \sum_{n=0}^{\infty} \varepsilon^n f_i^{(n)} = f_i^{(0)} + \varepsilon f_i^{(1)} + \varepsilon^2 f_i^{(2)} + ... \tag{A.28}$$

$$\partial_t = \sum_{n=0}^{\infty} \varepsilon^n \partial_{t_n} = \partial_{t_0} + \varepsilon\partial_{t_1} + \varepsilon^2\partial_{t_2} + ... \tag{A.29}$$

$$\partial_x = \sum_{n=0}^{\infty} \varepsilon^n \partial_{x_n} = \partial_{x_0} + \varepsilon\partial_{x_1} + \varepsilon^2\partial_{x_2} + ... \tag{A.30}$$

$$S = \sum_{n=0}^{\infty} \varepsilon^n S^{(n)} = S^{(0)} + \varepsilon S^{(1)} + \varepsilon^2 S^{(2)} + ... \tag{A.31}$$

Thus inserting the above perturbations up to the second order in A.27 yields:

$$\begin{aligned}\varepsilon\left(\sum_{n=0}^{2}\varepsilon^n\partial_{t_n} + c\Omega\sum_{n=0}^{2}\varepsilon^n\partial_{x_n}\right)\sum_{n=0}^{2}\varepsilon^n f_i^{(n)} \\ + \frac{\varepsilon^2}{2}\left(\sum_{n=0}^{2}\varepsilon^n\partial_{t_n} + c\Omega\sum_{n=0}^{2}\varepsilon^n\partial_{x_n}\right)\sum_{n=0}^{2}\varepsilon^n f_i^{(n)} = \\ \frac{1}{\tau}\left(\sum_{n=0}^{2}\varepsilon^n f_i^{(n)} - f_i^{eq}\right) + \varepsilon\left(\sum_{n=0}^{2}\varepsilon^n S^{(n)}\right) + \varepsilon w_i\left(\sum_{n=0}^{2}\varepsilon^n f_i^{(n)}\right)\end{aligned} \tag{A.32}$$

The reformulated equation can be written in the consecutive order of the parameter ε.

$$\varepsilon^0 : f_i^{(0)} = f_i^{eq} \tag{A.33}$$

$$\varepsilon^1 : \partial_t f_i^{(0)} + c\Omega\partial_{x_0} f_i^{(0)} = -\frac{1}{\tau} f_i^{(1)} + S^{(0)} + w_i f_i^{(0)} \tag{A.34}$$

Substituting Eq. A.33 into Eq. A.34 yields:

$$\frac{\partial f_i^{eq}}{\partial t} + c\Omega\partial_{x_0} f_i^{eq} + \frac{1}{\tau} f_i^{(1)} = S^{(0)} + f_i^{eq} \tag{A.35}$$

Spatial summation of the above equation leads to:

$$\sum_{\Omega} \frac{\partial f_i^{eq}}{\partial t} + \sum_{\Omega} c\Omega\partial_x f_i^{eq} = \sum_{\Omega} S + \sum_{\Omega} w_i f_i^{eq} \tag{A.36}$$

Which can be presented for the one-dimensional case as given by [32], thus formally neglecting the frequency associated influence:

$$\sum_{\Omega} \frac{\partial f_i^{eq}}{\partial t} + \sum_{\Omega} c\Omega \frac{f_i^{eq}}{\partial x} = \sum_{\Omega} S + \sum_{\Omega} w_i f_i^{eq} \tag{A.37}$$

Thus for weights w given as a function of the absorption coefficient κ_a and the speed of light c, the recovered macroscopic equation is given as

$$\frac{\partial I}{c\partial t} + \nabla I = S - \kappa_a I \tag{A.38}$$

Appendix B.

Macroscopic conservation equations of the energy equation

Mishra et al. showed in [26], whereupon this chapter is primarily based, a numerical analysis of a transient conduction-radiation problem whereat a LBM for the energy equation was derived. The general form of the LBM equations without external sources or fluxes is written as following:

$$\left(\frac{\partial}{\partial t} + \xi^{(i)} \cdot \nabla\right) g_{(i)}\left(\mathbf{r}, t\right) = \Omega_i \tag{B.1}$$

in which i denotes the directions of the PDFs given by $g_{(i)}\left(\mathbf{r}, t\right)$. The collision term is approximated using the BGK operator. *The main difficulty in handling the full Boltzmann equation arises from the complicated nature of the collision terms.* [23] Each collision term handles two parts, the first representing the removed and absorbed particle, the second representing collision caused emission of particles. The emission term is replaced in the BGK model *by a term representing a Maxwellian distribution of the emitted particles* [23], thus allowing conservation of the required quantities.

$$\Omega_i = \frac{\left(g_i^{eq} - g_i\right)}{\tau} \tag{B.2}$$

As evident in Eq. B.2 the model is a SRT model and thus according to [26] the relaxation constant τ can be related to the diffusivity of the medium, using the C-E analysis. The C-E analysis is in general terms used to determine a connection between the LBE and the macroscopic equation, in this case

the energy equation. *The Chapman–Enskog expansion is a vehicle to derive macroscopic equations from stream and collide equations. This is a crucial step of the LBM development, since it is not guarantied or even clear whether the computations in mesoscale generate suitable solutions of macroscopic target equations or not [sic!].* [24]
Rewriting Eq. B.1 with the BGK collision operator given in Eq. B.2 yields,

$$\left(\frac{\partial}{\partial t} + \xi^{(i)} \cdot \nabla\right) g_{(i)}\left(\mathbf{r}, t\right) = \frac{\left(g_i^{eq} - g_i\right)}{\tau} \tag{B.3}$$

which when applied a zero-order moment *gives a diffusion equation for the evolution of the scalar, with a diffusivity proportional to* τ [26]. If the zeroth, first and second order moments of both PDFs coincide, mass, momentum and energy are conserved through the BGK operator [24].
Recalling the corresponding LBE given below, renders the basis for further derivation of the macroscopic energy equation.

$$g_i\left(\tau_x + \vec{e}_i\Delta t, \tau_y + \vec{e}_i\Delta t, t + \Delta t\right) = g_i\left(\tau_x, \tau_y, t\right) - \frac{\Delta t}{\tau}\left[g_i - g_i^{eq}\right] \tag{B.4}$$

A Taylor series expansion of the left-hand-side up to the second order following [24] was performed.

$$g_i\left(\vec{x} + \vec{e}_i\Delta t, t + \Delta t\right) = g_i\left(\vec{x}, t\right) + \Delta t\left(\partial_t + \vec{e}_i\nabla\right) g_i\left(\vec{x}, t\right) + \frac{\Delta t^2}{2}\left(\partial_t + \vec{e}_i\nabla\right)^2 g_i\left(\vec{x}, t\right) \tag{B.5}$$

Substitution of Eq. B.5 in Eq. 4.2 gives the following equation:

$$\Delta t\left(\partial_t + \vec{e}_i\nabla\right) g_i\left(\vec{x}, t\right) + \frac{\Delta t^2}{2}\left(\partial_t + \vec{e}_i\nabla\right)^2 g_i\left(\vec{x}, t\right) = -\frac{\Delta t}{\tau}\left[g_i\left(\vec{x}, t\right) - g_i^{eq}\left(\vec{x}, t\right)\right] \tag{B.6}$$

Division by Δt renders:

$$\left(\partial_t + \vec{e}_i\nabla\right) g_i\left(\vec{x}, t\right) + \frac{\Delta t}{2}\left(\partial_t + \vec{e}_i\nabla\right)^2 g_i\left(\vec{x}, t\right) = -\frac{1}{\tau}\left[g_i\left(\vec{x}, t\right) - g_i^{eq}\left(\vec{x}, t\right)\right] \tag{B.7}$$

Next the scaling parameter ε (Note: in no connection to the radiative emissivity) is introduced which relates to the time step Δt as following:

$$\varepsilon = \Delta t^2 \tag{B.8}$$

Furthermore the time and space derivation are written according to the diffusive limit, [21], [24],

$$\partial_t \sim \varepsilon \partial_t \quad \nabla \sim \varepsilon \nabla \tag{B.9}$$

and the PDF g_i is expanded up to the second order by ε, as terms of higher order tend to be rather small and can be neglected according to [20].

$$g_i = g_i^{(0)} + \varepsilon g_i^{(1)} + \varepsilon^2 g_i^{(2)} (+...) \tag{B.10}$$

Deploying the scaling (B.8) and the expansion (B.10), the reformulated Eq. (B.7) can be rewritten in the consecutive orders of parameter ε as [24]

$$\left(\varepsilon^2 \partial_t + \vec{e}_i \varepsilon \nabla\right) g_i(\vec{x}, t) + \frac{\varepsilon^2}{2} \left(\varepsilon^2 \partial_t + \vec{e}_i \varepsilon \nabla\right)^2 g_i(\vec{x}, t) = - \frac{1}{\tau} \left[g_i(\vec{x}, t) - g_i^{eq}(\vec{x}, t)\right] \tag{B.11}$$

$$\varepsilon^0 : \qquad g_i^{(0)} = g_i^{eq} \tag{B.12}$$

$$\varepsilon^1 : \qquad \vec{e}_i \nabla g_i^{(0)} = -\frac{1}{\tau} g_i^{(1)} \tag{B.13}$$

$$\varepsilon^2 : \qquad \partial_t g_i^{(0)} + \vec{e}_i \nabla g_i^{(1)} = -\frac{1}{\tau} g_i^{(2)} \tag{B.14}$$

Inserting the zeroth and first orders of ε in the second order equation gives:

$$\partial_t g_i^{eq} - \tau |\vec{e}_i|^2 |\nabla|^2 g_i^{eq} = -\frac{1}{\tau} g_i^{(2)} \tag{B.15}$$

For the D2Q5 lattice $|\vec{e}_i|^2$ equals one. Recalling that all PDFs are close to their equilibrium, and the sum of all discrete equilibria represents the temperature, the recovered heat equation can be written as following:

$$\frac{\partial T}{\partial t} - \alpha \nabla^2 T = 0 \tag{B.16}$$

The relation between the thermal diffusivity and the relaxation time was found by Mishra et al. in [27] as following:

$$\tau = \frac{3\alpha}{|e_i|^2} + \frac{\Delta t}{2} \tag{B.17}$$

Appendix C.

Boundary conditions for the energy lattice Boltzmann equation

The Dirichlet boundary conditions are dependent on the lattice arrangement used, as they incorporate the lattice directions at the boundary. The implementation for the D2Q9 lattice arrangements was done by Mishra et al. [26]. Selfsame implementation has been adapted for usage of a D2Q5 lattice as described by [20]. Capital letters describe the respective directional maximum value, lower case letters the iterating directional variable.

C.1. D2Q9

This section is based on the findings of Mishra et al. [26].

- north boundary

$$g_4(x, Y, t) = (2/9) \cdot T_{\text{north boundary}} - g_2(x, Y, t)$$
$$g_7(x, Y, t) = (1/18) \cdot T_{\text{north boundary}} - g_5(x, Y, t)$$
$$g_8(x, Y, t) = (1/18) \cdot T_{\text{north boundary}} - g_6(x, Y, t)$$

- east boundary

$$g_3(X, y, t) = (2/9) \cdot T_{\text{east boundary}} - g_1(X, y, t)$$
$$g_6(X, y, t) = (1/18) \cdot T_{\text{east boundary}} - g_8(X, y, t)$$
$$g_7(X, y, t) = (1/18) \cdot T_{\text{east boundary}} - g_5(X, y, t)$$

- south boundary

$$g_2(x,0,t) = (2/9) \cdot T_{\text{south boundary}} - g_4(x,0,t)$$

$$g_5(x,0,t) = (1/18) \cdot T_{\text{south boundary}} - g_7(x,0,t)$$

$$g_6(x,0,t) = (1/18) \cdot T_{\text{south boundary}} - g_8(x,0,t)$$

- west boundary

$$g_1(0,y,t) = (2/9) \cdot T_{\text{west boundary}} - g_3(0,y,t)$$

$$g_5(0,y,t) = (1/18) \cdot T_{\text{west boundary}} - g_7(0,y,t)$$

$$g_8(0,y,t) = (1/18) \cdot T_{\text{west boundary}} - g_6(0,y,t)$$

C.2. D2Q5

- north boundary

$$g_4(x,Y,t) = (1/3) \cdot T_{\text{north boundary}} - g_2(x,Y,t)$$

- east boundary

$$g_3(X,y,t) = (1/3) \cdot T_{\text{east boundary}} - g_1(X,y,t)$$

- south boundary

$$g_2(x,0,t) = (1/3) \cdot T_{\text{south boundary}} - g_4(x,0,t)$$

- west boundary

$$g_1(0,y,t) = (1/3) \cdot T_{\text{west boundary}} - g_3(0,y,t)$$

Appendix D.

From the Boltzmann equation to the lattice Boltzmann equation

This section is based on [42] and shows the basic modus operandi behind the derivation of the LBE.

Boltzmann equation:

$$\frac{\partial f}{\partial t} + \mathbf{v}\nabla f = Q$$

Boltzmann equation (BGK approximation):

$$\frac{\partial f}{\partial t} + \mathbf{v}\nabla f = -\frac{1}{\tau}\left(f - f^{eq}\right)$$

discrete Boltzmann equation:

$$\frac{\partial f_i}{\partial t} + \mathbf{v_i}\nabla f_i = -\frac{1}{\tau}\left(f_i - f_i^{eq}\right)$$

non-dimensional discrete Boltzmann equation:

$$\frac{\partial F_i}{\partial \hat{t}} + c_i\hat{\nabla}F_i = -\frac{1}{\hat{\tau}\epsilon}\left(F_i - F_i^{eq}\right)$$

discretized Boltzmann equation:

$$\frac{F_i\left(\hat{x},\hat{t}+\Delta\hat{t}\right) - F_i\left(\hat{x},\hat{t}\right)}{\Delta\hat{t}} + c_{ix}\frac{F_i\left(\hat{x}+\Delta\hat{x},\hat{t}+\Delta\hat{t}\right) - F_i\left(\hat{x},\hat{t}+\Delta\hat{t}\right)}{\Delta\hat{t}}... = -\frac{1}{\hat{\tau}\epsilon}\left(F_i - F_i^{eq}\right)$$

lattice Boltzmann equation:

$$F_i\left(x + c_i\Delta t, t + \Delta t\right) - F_i\left(x,t\right) = -\frac{1}{\tau}\left(F_i - F_i^{eq}\right)$$

Bibliography

[1] B. Mayr, R. Prieler, M. Demuth, M. Potesser, and C. Hochenauer, 'CFD and experimental analysis of a 115 kW natural gas fired lab-scale furnace under oxy-fuel and air–fuel conditions', *Fuel*, vol. 159, pp. 864–875, 2015, ISSN: 0016-2361. DOI: https://doi.org/10.1016/j.fuel.2015.07.051. [Online]. Available: http://www.sciencedirect.com/science/article/pii/S0016236115007425 (cit. on p. 1).

[2] R. Prieler, B. Mayr, M. Demuth, B. Holleis, and C. Hochenauer, 'Prediction of the heating characteristic of billets in a walking hearth type reheating furnace using CFD', *International Journal of Heat and Mass Transfer*, vol. 92, pp. 675–688, 2016, ISSN: 0017-9310. DOI: https://doi.org/10.1016/j.ijheatmasstransfer.2015.08.056. [Online]. Available: http://www.sciencedirect.com/science/article/pii/S0017931015302295 (cit. on pp. 1, 11, 72–74, 76).

[3] M. F. Modest, *Radiative Heat Transfer*, Third Edition. Academic Press, 2013, 904 pp., ISBN: 978-0-12-386944-9 (cit. on pp. 2–6, 10–12, 20–22, 55).

[4] J. R. Howell, M. P. Menguc, and R. Siegel, *Thermal Radiation Heat Transfer*, Fifth edition. Boca Raton: CRC Press, 2010, 987 pp., ISBN: 978-1-4398-0533-6 (cit. on pp. 2, 4, 6, 8, 12, 17, 22, 26, 28, 53).

[5] M. Kuang, Q. Zhu, Z. Ling, S. Ti, and Z. Li, 'Improving gas/particle flow deflection and asymmetric combustion of a 600 MWe supercritical down-fired boiler by increasing its upper furnace height', *Energy*, vol. 127, pp. 581–593, 2017, ISSN: 0360-5442. DOI: https://doi.org/10.1016/j.energy.2017.04.002. [Online]. Available: http://www.sciencedirect.com/science/article/pii/S0360544217305649 (cit. on p. 10).

[6] C. Zhang, T. Ishii, and S. Sugiyama, 'Numerical modeling of the thermal performance of regenerative slab reheat furnaces', *Numerical Heat Transfer, Part A: Applications*, vol. 32, no. 6, pp. 613–631, 1997. DOI: 10.1080/10407789708913909 (cit. on p. 10).

[7] C. Caliot, 'Numerical methods in radiative transfer - introduction to DOM, FVM and MCM', PROMES-CNRS Lab., Jun. 11, 2010, [Online]. Available: http://sfera.sollab.eu/downloads/Schools/Caliot_DOM_FVM_MCM.pdf (cit. on p. 11).

[8] M. Sankar, 'A hybrid discrete ordinates - spherical harmonics method for solution of the radiative transfer equation in multi-dimensional participating media', Masterthesis, Ohio State University, 2011. [Online]. Available: https://etd.ohiolink.edu/rws_etd/document/get/osu1308244319/inline (cit. on p. 11).

[9] ANSYS Inc., *ANSYS Fluent 14.0 Theory Guide*. 2011 (cit. on pp. 11, 44, 61, 62).

[10] T. Morgado, P. J. Coelho, and P. Talukdar, 'Assessment of uniform temperature assumption in zoning on the numerical simulation of a walking beam reheating furnace', *Applied Thermal Engineering*, vol. 76, pp. 496–508, 2015, ISSN: 1359-4311. DOI: https://doi.org/10.1016/j.applthermaleng.2014.11.054. [Online]. Available: http://www.sciencedirect.com/science/article/pii/S1359431114010886 (cit. on p. 11).

[11] M. Landfahrer, R. Prieler, B. Mayr, H. Gerhardter, R. Schöngrundner, J. Klarner, and C. Hochenauer, 'Development of a numerically efficient CFD model to predict transient temperature distribution of mother tubes moving translative and rotative through a gas fired furnace', *Applied Thermal Engineering*, vol. 123, pp. 290–300, 2017, ISSN: 1359-4311. DOI: https://doi.org/10.1016/j.applthermaleng.2017.05.093. [Online]. Available: http://www.sciencedirect.com/science/article/pii/S1359431117306567 (cit. on p. 11).

[12] M. Landfahrer, R. Prieler, B. Mayr, H. Gerhardter, T. Zmek, J. Klarner, and C. Hochenauer, 'Characterization of the temperature distribution on steel tubes for different operating conditions in a reheating furnace using CFD and three different measuring methods', *Applied Thermal Engineering*, vol. 133, pp. 39–48, 2018, ISSN: 1359-4311. DOI: https:

//doi.org/10.1016/j.applthermaleng.2017.12.098. [Online]. Available: http://www.sciencedirect.com/science/article/pii/S135943111735439X (cit. on p. 11).

[13] S. H. Han, D. Chang, and C. Y. Kim, 'A numerical analysis of slab heating characteristics in a walking beam type reheating furnace', *International Journal of Heat and Mass Transfer*, vol. 53, no. 19, pp. 3855–3861, 2010, ISSN: 0017-9310. DOI: https://doi.org/10.1016/j.ijheatmasstransfer.2010.05.002. [Online]. Available: http://www.sciencedirect.com/science/article/pii/S001793101000236X (cit. on p. 11).

[14] G. Tang, B. Wu, D. Bai, Y. Wang, R. Bodnar, and C. Zhou, 'CFD modeling and validation of a dynamic slab heating process in an industrial walking beam reheating furnace', *Applied Thermal Engineering*, vol. 132, pp. 779–789, 2018, ISSN: 1359-4311. DOI: https://doi.org/10.1016/j.applthermaleng.2018.01.017. [Online]. Available: http://www.sciencedirect.com/science/article/pii/S1359431117325954 (cit. on pp. 11, 71).

[15] W. Yuen and E. Takara, 'The zonal method: A practical solution method for radiative transfer in non-isothermal inhomogeneous media', vol. 8, pp. 153–215, Jan. 1995 (cit. on p. 12).

[16] Z. Li, P. Barr, and J. Brimacombe, 'Computer simulation of the slab reheating furnace', *Canadian Metallurgical Quarterly*, vol. 27, no. 3, pp. 187–196, 1988 (cit. on p. 12).

[17] W. Wu, Y. Feng, and X. Zhang, 'Zonal method solution of radiative heat transfer in a one-dimensional long roller-hearth furnace in CSP', *Journal of University of Science and Technology Beijing, Mineral, Metallurgy, Material*, vol. 14, no. 4, pp. 307–311, 2007, ISSN: 1005-8850. DOI: https://doi.org/10.1016/S1005-8850(07)60060-7. [Online]. Available: http://www.sciencedirect.com/science/article/pii/S1005885007600607 (cit. on p. 12).

[18] H. Ebrahimi, A. Zamaniyan, J. S. S. Mohammadzadeh, and A. A. Khalili, 'Zonal modeling of radiative heat transfer in industrial furnaces using simplified model for exchange area calculation', *Applied Mathematical Modelling*, vol. 37, no. 16, pp. 8004–8015, 2013, ISSN: 0307-904X. DOI: https://doi.org/10.1016/j.apm.2013.02.053. [Online]. Available: http://

www.sciencedirect.com/science/article/pii/S0307904X13001923 (cit. on p. 12).

[19] P. Asinari, R. Borchiellini, and S. C. Mishra, 'A lattice Boltzmann formulation for the analysis of radiative heat transfer problems in a participating medium', *NUMERICAL HEAT TRANSFER PART B-FUNDAMENTALS*, vol. 57, pp. 1–21, Mar. 10, 2010. DOI: 10.1080/10407791003613769 (cit. on pp. 13, 18, 21–23, 32, 35, 36).

[20] T. Krüger, H. Kusumaatmaja, A. Kuzmin, O. Shardt, G. Silva, and E. M. Viggen, *The Lattice Boltzmann Method - Principles and Practice*. Springer, 2017, ISBN: 978-3-319-44649-3. [Online]. Available: //www.springer.com/de/book/9783319446479 (cit. on pp. 14, 24, 25, 33, 37–39, 43, 45, 103, 105).

[21] A. A. Mohamad, *Lattice Boltzmann Method - Fundamentals and Engineering*. 2011. [Online]. Available: http://www.springer.com/de/book/9780857294548 (cit. on pp. 15, 30, 37, 103).

[22] R. McCulloch, 'Advances in radiation transport modeling using lattice Boltzmann methods', Masterthesis, Kansas State University, 2015. [Online]. Available: https://krex.k-state.edu/dspace/bitstream/handle/2097/20516/RichardMcCulloch2015.pdf?sequence=3 (cit. on pp. 16, 18, 19, 27, 31, 33, 45, 53).

[23] P. L. Bhatnagar, E. P. Gross, and M. Krook, 'A model for collision processes in gases. i. small amplitude processes in charged and neutral one-component systems', *Physical Review*, vol. 94, pp. 511–525, May 1954. DOI: 10.1103/PhysRev.94.511 (cit. on pp. 16, 17, 101).

[24] A. Mink, G. Thäter, H. Nirschl, and M. J. Krause, 'A 3D lattice Boltzmann method for light simulation in participating media', *Journal of Computational Science*, Discrete Simulation of Fluid Dynamics 2015, vol. 17, pp. 431–437, Part 2 Nov. 1, 2016, ISSN: 1877-7503. DOI: 10.1016/j.jocs.2016.03.014. [Online]. Available: http://www.sciencedirect.com/science/article/pii/S1877750316300357 (cit. on pp. 17, 18, 102, 103).

[25] R. Geist, K. Rasche, J. Westall, and R. Schalkoff, *Lattice-Boltzmann Lighting*. The Eurographics Association, 2004, ISBN: 978-3-905673-12-8. [Online]. Available: https://diglib.eg.org:443/handle/10.2312/EGWR.EGSR04.355-362 (cit. on p. 17).

[26] S. C. Mishra, A. Lankadasu, and K. N. Beronov, 'Application of the lattice Boltzmann method for solving the energy equation of a 2-D transient conduction–radiation problem', *International Journal of Heat and Mass Transfer*, vol. 48, no. 17, pp. 3648–3659, 2005, ISSN: 0017-9310. DOI: https://doi.org/10.1016/j.ijheatmasstransfer.2004.10.041. [Online]. Available: http://www.sciencedirect.com/science/article/pii/S0017931005000864 (cit. on pp. 17, 39, 40, 59, 67, 101, 102, 105).

[27] S. C. Mishra and A. Lankadasu, 'Transient conduction-radiation heat transfer in participating media using the lattice Boltzmann method and the discrete transfer method', *Numerical Heat Transfer, Part A: Applications*, vol. 47, no. 9, pp. 935–954, 2005. DOI: 10.1080/10407780590921935. eprint: https://doi.org/10.1080/10407780590921935. [Online]. Available: https://doi.org/10.1080/10407780590921935 (cit. on pp. 17, 25, 29, 43, 103).

[28] S. C. Mishra, B. Mondal, T. Kush, and B. S. R. Krishna, 'Solving transient heat conduction problems on uniform and non-uniform lattices using the lattice Boltzmann method', *International Communications in Heat and Mass Transfer*, vol. 36, no. 4, pp. 322–328, Apr. 1, 2009, ISSN: 0735-1933. DOI: 10.1016/j.icheatmasstransfer.2009.01.001. [Online]. Available: http://www.sciencedirect.com/science/article/pii/S0735193309000128 (cit. on p. 17).

[29] S. C. Mishra, M. Y. Kim, and S. Maruyama, 'Performance evaluation of four radiative transfer methods in solving multi-dimensional radiation and/or conduction heat transfer problems', *International Journal of Heat and Mass Transfer*, vol. 55, no. 21, pp. 5819–5835, Oct. 1, 2012, ISSN: 0017-9310. DOI: 10.1016/j.ijheatmasstransfer.2012.05.078. [Online]. Available: http://www.sciencedirect.com/science/article/pii/S0017931012004073 (cit. on pp. 17, 18, 29).

[30] S. C. Mishra, H. Poonia, R. R. Vernekar, and A. K. Das, 'Lattice Boltzmann method applied to radiative transport analysis in a planar participating medium', *Heat Transfer Engineering*, vol. 35, no. 14-15, pp. 1267–1278, 2014. DOI: 10.1080/01457632.2013.876806. eprint: https://doi.org/10.1080/01457632.2013.876806. [Online]. Available: https://doi.org/10.1080/01457632.2013.876806 (cit. on pp. 17, 37).

[31] S. C. Mishra, H. Poonia, A. K. Das, P. Asinari, and R. Borchiellini, 'Analysis of conduction-radiation heat transfer in a 2D enclosure using the lattice Boltzmann method', *Numerical Heat Transfer, Part A: Applications*, vol. 66, no. 6, pp. 669–688, 2014. DOI: 10.1080/10407782.2014.894376. eprint: https://doi.org/10.1080/10407782.2014.894376. [Online]. Available: https://doi.org/10.1080/10407782.2014.894376 (cit. on pp. 17, 21, 27, 28).

[32] Y. Ma, S. Dong, and H. Tan, 'Lattice Boltzmann method for one-dimensional radiation transfer', *Physical review. E, Statistical, nonlinear, and soft matter physics*, vol. 84, p. 016 704, Jul. 1, 2011. DOI: 10.1103/PhysRevE.84.016704 (cit. on pp. 17–19, 95, 96, 98, 100).

[33] G. C. Pomraning, *The Equations of Radiation Hydrodynamics*. Courier Corporation, 1973, 306 pp., ISBN: 978-0-486-44599-1 (cit. on pp. 18, 95).

[34] A. F. D. Rienzo, P. Asinari, R. Borchiellini, and S. C. Mishra, 'Improved angular discretization and error analysis of the lattice Boltzmann method for solving radiative heat transfer in a participating medium', *International Journal of Numerical Methods for Heat & Fluid Flow*, vol. 21, no. 5, pp. 640–662, Jun. 14, 2011, ISSN: 0961-5539. DOI: 10.1108/09615531111135873. [Online]. Available: http://www.emeraldinsight.com/doi/full/10.1108/09615531111135873 (cit. on pp. 18, 22).

[35] H. Bindra and D. V. Patil, 'Radiative or neutron transport modeling using a lattice Boltzmann equation framework', *Physical Review E*, vol. 86, no. 1, p. 016 706, Jul. 18, 2012. DOI: 10.1103/PhysRevE.86.016706. [Online]. Available: https://link.aps.org/doi/10.1103/PhysRevE.86.016706 (cit. on p. 18).

[36] Y. Zhang, H. Yi, and H. Tan, 'One-dimensional transient radiative transfer by lattice Boltzmann method', *Optics Express*, vol. 21, no. 21, p. 24 532, Oct. 21, 2013, ISSN: 1094-4087. DOI: 10.1364/OE.21.024532. [Online]. Available: https://www.osapublishing.org/oe/abstract.cfm?uri=oe-21-21-24532 (cit. on p. 18).

[37] R. McCulloch and H. Bindra, 'Coupled radiative and conjugate heat transfer in participating media using lattice Boltzmann methods', *Computers & Fluids*, vol. 124, pp. 261–269, 2016, Special Issue for ICMMES-2014, ISSN: 0045-7930. DOI: https://doi.org/10.1016/j.compfluid.2015.05.

024. [Online]. Available: http://www.sciencedirect.com/science/article/pii/S0045793015001796 (cit. on pp. 18, 19, 27, 33, 37, 63).

[38] T. Bralower and D. Bice. (). Radiative equilibrium — EARTH 103: Earth in the future. College of Earth and Mineral Science, The Pennsylvania State University, [Online]. Available: https://www.e-education.psu.edu/earth103/node/1003 (visited on 10/18/2017) (cit. on p. 22).

[39] S. P. C. Marques, E. J. Barbero, and J. S. R. Murillo, 'Analysis of conduction-radiation problem in absorbing and emitting nongray materials', *International Journal of Numerical Methods for Heat & Fluid Flow*, vol. 19, no. 2, pp. 165–181, Mar. 27, 2009, ISSN: 0961-5539. DOI: 10.1108/09615530910930955. [Online]. Available: http://www.emeraldinsight.com/doi/full/10.1108/09615530910930955 (cit. on p. 26).

[40] H.-L. Yi, F.-J. Yao, and H.-P. Tan, 'Lattice Boltzmann model for a steady radiative transfer equation', *Physical Review E*, vol. 94, no. 2, p. 023 312, Aug. 18, 2016. DOI: 10.1103/PhysRevE.94.023312. [Online]. Available: https://link.aps.org/doi/10.1103/PhysRevE.94.023312 (cit. on pp. 28, 36).

[41] Z. Jian Guo, *Lattice Boltzmann Methods for Shallow Water Flows*, First Edition. Springer, Berlin, Heidelberg, 2004, ISBN: 978-3-642-07393-9. DOI: https://doi.org/10.1007/978-3-662-08276-8 (cit. on pp. 29, 30).

[42] D. A. Wolf-Gladrow, *Lattice-Gas Cellular Automata and Lattice Boltzmann*. Springer, 2000, ISBN: 978-3-540-46586-7. [Online]. Available: //www.springer.com/de/book/9783540669739 (cit. on pp. 30, 31, 33, 107).

[43] Z. Guo and C. Shu, *Lattice Boltzmann Method and Its Applications in Engineering*. Hackensack, New Jersey: World Scientific Publishing Company, 2013, 420 pp., ISBN: 978-981-4508-29-2 (cit. on pp. 32, 33).

[44] Y. Shi, Y. W. Yap, and J. E. Sader, 'Lattice Boltzmann method for linear oscillatory noncontinuum flows', *Phys. Rev. E*, vol. 89, p. 033 305, 3 2014 (cit. on p. 32).

[45] H.-J. Bartsch and M. Sachs, *Taschenbuch mathematischer Formeln für Ingenieure und Naturwissenschaftler*. Hanser Fachbuch, 2014, ISBN: 978-3-446-43800-2 (cit. on p. 34).

[46] H. Lee, S. Bawazeer, and A. Mohamad, 'Boundary conditions for lattice Boltzmann method with multispeed lattices', *Computers & Fluids*, vol. 162, pp. 152–159, 2018, ISSN: 0045-7930. DOI: https://doi.org/10.1016/j.compfluid.2017.12.011. [Online]. Available: http://www.sciencedirect.com/science/article/pii/S0045793017304498 (cit. on p. 38).

[47] B. Mayr, R. Prieler, M. Demuth, and C. Hochenauer, 'Comparison between solid body and gas radiation in high temperature furnaces under different oxygen enrichments', *Applied Thermal Engineering*, vol. 127, pp. 679–688, Supplement C Dec. 25, 2017, ISSN: 1359-4311. DOI: 10.1016/j.applthermaleng.2017.08.054. [Online]. Available: http://www.sciencedirect.com/science/article/pii/S1359431117310979 (cit. on p. 53).

[48] ANSYS Inc., *Module 09: Best practice guidelines - introduction to ansys fluent*, Knowledge Resources: Tutorials & Training Materials - Introduction to ANSYS Fluent 17.0, 2016 (cit. on p. 42).

[49] W. Trinks, M. H. Mawhinney, R. A. Shannon, R. J. Reed, and J. R. Garvey, *Industrial Furnaces*, Sixth edition. New Jersey: Jon Wiley & Sons, Inc., 2004, 496 pp., ISBN: 978-0-471-38706-0 (cit. on p. 71).

[50] V. K. Singh and P. Talukdar, 'Comparisons of different heat transfer models of a walking beam type reheat furnace', *International Communications in Heat and Mass Transfer*, vol. 47, pp. 20–26, 2013, ISSN: 0735-1933. DOI: https://doi.org/10.1016/j.icheatmasstransfer.2013.06.004. [Online]. Available: http://www.sciencedirect.com/science/article/pii/S0735193313001292 (cit. on p. 71).

[51] J. I. Castor, *Radiation Hydrodynamics*. Lawrence Livermore National Laboratory, 2003. [Online]. Available: https://e-reports-ext.llnl.gov/pdf/301321.pdf (cit. on p. 95).